UCGE Reports

Number 20312

Department of Geomatics Engineering

High Latitude Ionospheric Scintillation: Detection and Isolation from Oscillator Phase Noise as Applied to GNSS

(URL: http://www.geomatics.ucalgary.ca/graduatetheses)

by

Aiden J. Morrison

August 2010

UNIVERSITY OF CALGARY

HIGH LATITUDE IONOSPHERIC SCINTILLATION: DETECTION AND ISOLATION FROM OSCILLATOR PHASE NOISE AS APPLIED TO GNSS

by

Aiden J. Morrison

A THESIS

SUBMITTED TO THE FACULTY OF GRADUATE STUDIES

IN PARTIAL FULFILMENT OF THE REQUIREMENTS FOR THE

DEGREE OF DOCTOR OF PHILOSOPHY

DEPARTMENT OF GEOMATICS ENGINEERING

CALGARY, ALBERTA

AUGUST, 2010

Abstract

This thesis investigates the detection of high latitude ionospheric scintillation effects using data collected by the author during two field exercises into the Canadian low arctic and high arctic regions during March and October-November 2008 respectively. The effect of ionospheric phase scintillation in these regions is studied through the observation of the influence it has on both the L1CA and L2C modernized GPS signals simultaneously. A pulsation detection method is proposed and investigated which identifies, and in turn exploits an apparent high level of correlation between the phase effects present on the L1 and L2 GPS carriers during low arctic pulsation events. Using this data, the level of correlated activity between the civil GPS signals during both polar and auroral scintillation events is related to the physical scale sizes of detectable ionospheric features. As a further novel contribution the presentation of a method for estimating the epoch to epoch phase change in the local oscillator over millisecond time scales is presented. This method is potentially capable of providing apparent phase stability commensurate with the use of an ovenized quartz oscillator within equipment actually utilizing an inexpensive (e.g. TCXO) oscillator, thereby allowing phase scintillation detection while using very low cost user equipment. An appendix detailing the design and development of a multi channel multi GNSS wide bandwidth research front-end for use in future investigations is included.

Acknowledgements

I would like to thank my family, my friends, my colleagues in the PLAN group, and my supervisors, Professors Gérard Lachapelle and M. Elizabeth Cannon, for the time and support they have given to me during my studies. The ionospheric expertise, time and advice provided by Professor Susan Skone is also highly appreciated. I would also like to thank the organizations that have helped fund and facilitate my research including The University of Calgary, the Natural Sciences and Engineering Research Council (NSERC), the informatics Circle of Research Excellence (iCORE), the Association of Canadian Universities for Northern Studies (ACUNS), the Canadian Northern Studies Trust (CNST), Environment Canada including the staff of the Eureka High Arctic Weather Station, the Canadian Network for the Detection of Atmospheric Change (CANDAC), and the Churchill Northern Studies Centre.

Dedication

This thesis is dedicated to Dr. Reza Sedaghat, the person I consider directly responsible for my arrival at this time and place. Thank you once more for giving me the chance to excel.

Table of Contents

List of Tables

List of Figures and Illustrations

List of Symbols, Abbreviations and Nomenclature

Symbol	Definition
ACE	Advanced Composition Experiment (satellite)
ADR	Accumulated Delta Range
ASIC	Application Specific Integrated Circuit
BOC	Binary Offset Carrier
Bn	Noise Bandwidth
CME	Coronal Mass Ejection
CPLD	Complex Programmable Logic Device
CS	Central Synchronizer
DVB-S	Direct Video Broadcast Satellite
DVB-S2	Second generation DVB-S
EMI	Electromagnetic Interference
FPGA	Field Programmable Gate Array
GLONASS	GLObal NAvigation Satellite System
GNSS	Global Navigation Satellite System
GPS	Global Positioning System
HDF	Multi-Object File Format
IC	Integrated Circuit
IF	Intermediate Frequency
IPP	Ionospheric Pierce Point
I/Q	In-Phase and Quadrature
L1	Microwave signal band
L1CA	Civilian GPS signal in the L1 Band
L2	Microwave signal band
L2C	Civilian GPS signal in the L2 Band
L2CA	Civilian GLONASS signal in the L2 Band
L2P(Y)	Encrypted Military signal in the L2 Band
MB	Mega Byte
MCXO	Microcontroller compensated XO
NBP	Narrowband Power
OCXO	Ovenized OCXO (single or double oven)
P-Code	Precise GPS or GLONASS signal code
PCB	Printed Circuit Board
PDF	Probability Distribution Function
PLL	Phase Locked Loop
PNT	Positioning Navigation and Timing
PPS	Pulse Per Second
PSD	Power Spectral Density
RAM	Random Access Memory
RF	Radio Frequency
RWFM	Random Walk Frequency Modulation
S4	Amplitude Fading Scintillation Index
SA	Selective Availability

SED	Storm Enhanced Density
TEC	Total Electron Content
TECU	Units of TEC
TID	Travelling Ionospheric Disturbances
TCXO	Temperature Compensated XO
TKS	Time Keeping System
USB	Universal Serial Bus
USNO	United States Naval Observatory
WBP	Wideband Power
XO	Crystal Oscillator

Chapter One: Introduction and Overview

Global Navigation Satellite Systems (GNSS's) including the currently operational GPS and GLONASS constellations were originally designed in the 1970's and 1980's by military organizations to provide Positioning Navigation and Timing (PNT) services to the armed forces of the United States and Soviet Union, respectively. While both of these systems included a capacity to service civilian needs, this functionality remained secondary during the first decades of each system as the cost of the hardware required to use the systems remained high, and the number of non-military users remained relatively small. This pattern of use did not shift until at least the 1990's when it was announced by then U.S. President Bill Clinton that the intentional degradation of the civilian portion of GPS signals known as Selective Availability (SA) would be deactivated. This deactivation of SA, when combined with European plans to launch a civilian controlled GNSS, Galileo, as well as the miniaturization and cost reduction of receiver electronics began a long and sustained drive to ever higher levels of use of satellite navigation technology among the general public. Simultaneous with the advances in user equipment, the advanced nature of the proposed Galileo system, along with modernization efforts in the GPS and GLONASS systems promised vastly increased levels of civilian service, including two and eventually three civilian signals to be broadcast from each GPS and GLONASS satellite. Additionally, consideration of safety of life integrity requirements including the use of protected radio-navigation bands of spectrum for at least one of these signals (GPS World 2008), and inclusion of more reliable indications of satellite health in broadcast data have been discussed. However, despite the increased reliance upon, modernization of, and interest in GNSS in general,

relatively little is known about how these improved systems will fare during the coming peak of the 11 year solar activity cycle, and the associated increase in ionospheric scintillation occurrence due in May 2013 (NOAA 2009).

1.1 Background

While the uses of, and the dependence upon, GNSS systems has continued to rise, consequently so too has the risk posed by disruption to these systems from numerous naturally occurring and man-made sources. One naturally occurring source of this interference worth considering is that of ionospheric scintillation, characterized by its 11-year cyclical intensity as discussed in NOAA (2009), and its ability to cause disruption over vast geographic regions simultaneously. The study of this phenomenon via GNSS has been limited in past cycles due to several former restrictions on researchers, including the lack of availability of strong multiple frequency carriers, the lack of easily reconfigurable software receivers for conducting analysis, and the lack of raw IF sample data for post processing and investigation within these receivers. In fact the first broadcast of a civilian accessible second signal did not occur until the first GLONASS-M launch in 2003 (Victorkosenko & Chebotarev 2006), while the first broadcast of the L2C signal from GPS did not occur until late 2005 (Boeing 2005), both well after the preceding peak in the solar cycle but fortuitously well in advance of the next maxima.

Since the last solar maxima the desire to better understand the ionosphere, and develop tracking methods which can operate robustly during high latitude scintillation events has

increased dramatically. One example of the drivers behind this increased desire is the recent political posturing between Canada, the United States, Russia and Denmark regarding the control and ownership of the potential resources under the Arctic Ocean. These efforts to establish arctic sovereignty will bring a higher concentration to users to the polar regions of Canada, at a time coinciding with the next solar maxima.

1.2 Literature Review

Past and current works within the GNSS field involving ionospheric scintillation often cover multiple sub-categories of interest simultaneously. A functional distinction adopted by the author is to categorize publications as occupying one or more of the three sub-categories of ionospheric scintillation event modelling and detection, quantitative effects of ionospheric scintillation on GNSS, and the design or optimization of GNSS receiver technologies or parameters to mitigate scintillation. The reference literature when divided into these categories is represented in Figure 1-1.

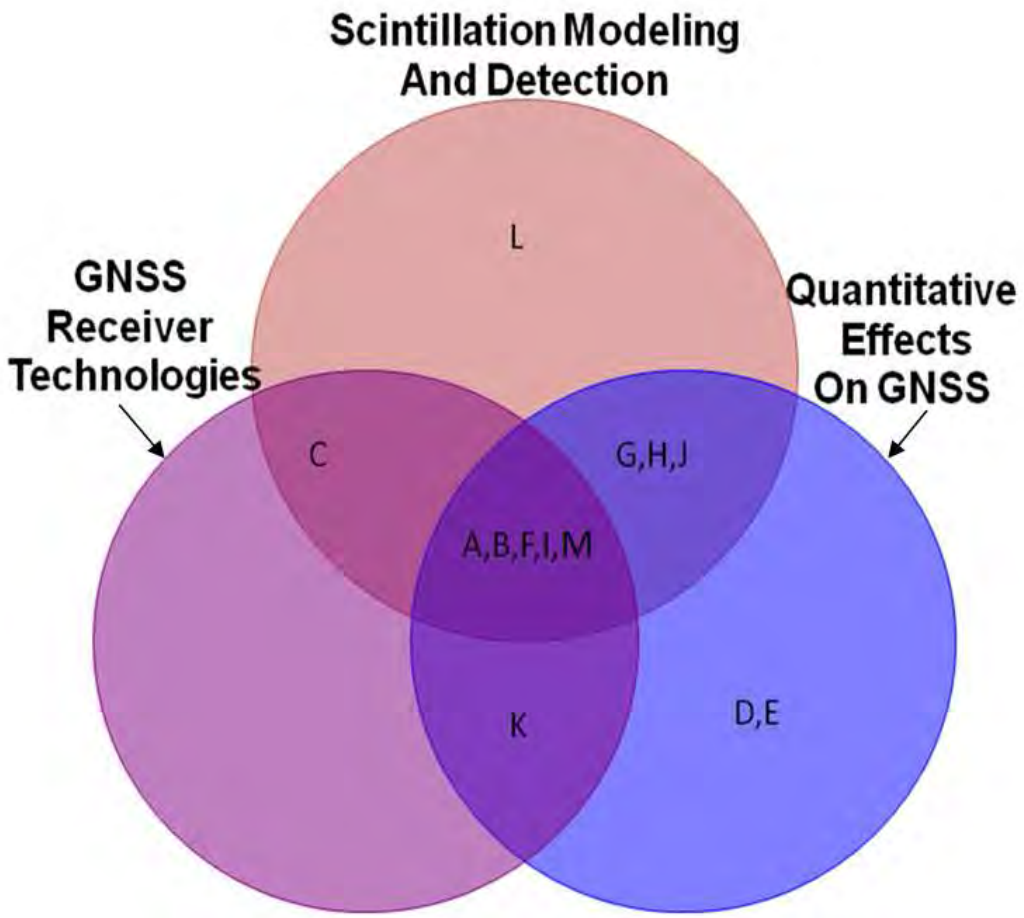

Figure 1-1: Venn diagram representation of overlapping sub categories of interest within the existing body of literature.

The publications in Figure 1-1 are summarized for convenience and discussed below:

A) Skone et al (2005)

B) Conker et al (2000)

C) Béniguel et al (2004)

D) Datta-Barua et al (2003)

E) Skone and knudsen (2000)

F) Hinks et al (2008)

G) Rodrigues et al (2004)

H) Moaraes et al (2009)

I) Yu et al (2006)

J) Pullen et al (1998)

K) Humphreys et al (2004)

L) Van Dierendonck (1999)

M) Psiaki et al (2007)

Certain common elements can be identified within this cross section of literature which shows patterns of both excellence and deficiency within the existing body of work. Publications F - Hinks et al (2008), H - Moaraes et al (2009) and J – Pullen et al (1998), each provide an extensive review of equatorial scintillation, but only through the lense of simulated data. While publication F does introduce a potentially very useful 'hardware in the loop' fast simulation model for equatorial scintillation simulation based on real world data, the work itself contains no new primary source information. Additionally Pullen et al (1998) relied on sources of primary data more than two decades old at the time of publication. Publication C - Béniguel et al (2004) does distinguish itself through validation of its findings with real world data collected in a high latitude auroral region, but is also based mainly on theoretical findings from modeled sources of data.

Among the papers that concern themselves in part with receiver design considerations, including Publication B – Conker et al (2000), Publication I - Yu et al (2006) and Publication A - Skone et al (2005), each provides excellent insight into receiver design choices for scintillation resistance, but once again rely to a large degree on simulated scintillation. Conker et al (2000) provides the best statistical impact summaries of

scintillation parameters on the ability of a given GNSS receiver to track both the GPS L1, L2 and WAAS L1 signals, while Yu et al (2006) and Skone et al (2005) both provide excellent overviews of the best practices of design for a receiver that must operate under scintillation conditions.

In terms of primary data sourcing, only Publication G - Rodrigues et al (2004) appears to consider a large data set of environment sourced scintillation observations, and utilizes this for the determination of its findings. Additionally Rodrigues et al (2004) is the only publication in the body cited which discusses data sourced from the environment above 70 degrees north latitude. This supports the assertion that the polar effects of scintillation observed via L1 plus L2 civil GPS signals are minimal in the current literature. In light of this it can be stated that there has been relatively little recent publication regarding the observation of polar scintillation activity via GNSS utilizing strong dual frequency signals. This work will attempt to overcome this as well as other limitations in the context of GNSS receiver operation.

1.3 Improvements over Previous Contributions

When compared to other pre-existing works concerning the interaction of ionospheric scintillation and received GNNS signals, the investigations carried out herein present a number of important improvements. These improvements are stated, and expanded upon below.

1) Multi-Carrier Scintillation Analysis – The vast majority of literature to date regarding ionospheric scintillation and GNSS has been produced via observation of only the L1 GPS carrier. Some researchers have in the past used codeless or semi-codeless observations from GPS L2, but only M- Psiaki et al (2007) is known to have contributed analyses based on multiple strong civilian accessible signals. Even then however, the observations used were collected in an equatorial region in Brazil, with the focus of the analysis devoted to the fading rather than the phase effects of scintillation. In this work the development of civilian multi-carrier based analysis methods are developed in order to better determine the characteristics of real-world auroral and polar scintillation events.

2) Frequency Reference Considerations – Previously, when quantifying the parameters of ionospheric phase scintillation, it was necessary to have a local timing standard with extremely low phase noise (Van Dierendonck & Hua 2001). This added additional expense and in many cases power requirements to not only the equipment that must be used to measure and observe scintillation effects, but also to any future user equipment that must detect scintillation as part of an overall scintillation resistance strategy. In this thesis, methods for removing the majority of phase noise contributions from the local oscillator with delays in the tens of milliseconds range are presented. These methods will allow the use of equipment with modest oscillator requirements in scintillation detection, analysis, or scintillation resistant tracking roles.

3) Sources of Data – The data used in all evaluations of scintillation behaviour are the product of real world data collection campaigns, where Intermediate Frequency (IF) samples of the GPS L1 and L2 navigation bands were collected during an active ionospheric scintillation event. In short, all GNSS data considered in this report is sourced directly from the environment, in theory allowing representative models to be created from the results. Past investigations using GNSS have by contrast consisted largely of modeled effects based on the interactions of other satellite communication systems with the ionosphere, or of interpretation of observation domain data at the output of a commercial receiver.

4) Frequency Diversity of Data – While some previous contributions included considerations of the advantages and weaknesses of using multiple carriers within the same constellation including reference 'D' - Datta-Barua et al (2003), these investigations were often conducted at the observation level utilizing equipment which employed codeless or semi-codeless tracking techniques to track the L2 GPS carrier via the L2P(Y) signal. Unfortunately, the consequences of this approach include the amplification of the apparent fragility of the L2 carrier during ionospheric events due to the large power losses associated with this method of tracking, as well as the loss of independence of the L2 measurement due to the use of L1 dynamics to aid in the tracking of the other signal. This limitation of previous work is not due to a shortcoming of the Authors of the studies, but rather due to the simple unavailability of multiple civilian accessible signals on existing navigation satellites at the time of these studies. As of the

writing of this thesis, while 21 GLONASS satellites carry an L2CA payload, only 7 GPS satellites carry an L2C signal payload. Through fieldwork during 2008, dozens of scintillation events have been captured simultaneously from L1/L2C capable GPS satellites, eliminating the former losses and correlations through independent tracking of each carrier. While equipment was not available during the execution of data collection for this effort to collect the GLONASS L1/L2 IF samples in addition to GPS L1/L2 IF samples, a front-end for this purpose was subsequently designed, as described in Appendix A.

5) Geographic Diversity of Data – The data collected during the scintillation events discussed was collected at latitudes of 60 degrees and 80 degrees north, respectively, providing for observations of both mid/high latitude and very high northern latitudes. The advantage gained through this diversity is in the potential identification of differences in scintillation characteristics between these regions, in light of the previously existing work which has been effective to observe the characteristics of the deep fades typical of equatorial scintillation phenomena (e.g. reference K - Humphreys et al 2004). While mid/high latitude studies have been conducted in the past such as in reference E - Skone and Knudsen (2000) the high latitude data considered herein is expected to be the highest latitude observation of scintillation via GNSS IF sample collection conducted to date, and therefore of potential interest to polar users as well as transpolar navigation operators of GNSS equipment.

1.4 Contributions and Objectives

i) Statement of Contributions

All activities undertaken in support and preparation of this thesis were conducted exclusively by the author. These activities include but are not limited to design or selection of field data collection equipment, logistical planning for expeditions, conduct of actual field data collection, subsequent data analysis and novel theory development, as well as front-end hardware design and embedded software development.

ii) Contributions

One of the key contributions of this thesis is derived from the development of processes to allow the rapid estimation of the phase noise introduced by the local oscillator of a GNSS system or IF data logging front-end. In the context of scintillation detection and resistance, this allows the use of very low cost oscillators in equipment that may then still be used to study ionospheric phase scintillation.

An additional primary contribution of this work includes the development of multi-carrier based, high bandwidth characterization of phase scintillation events. These methods determine the maximum carrier correlation frequency during auroral and polar phase scintillation, and by extension allow the calculation of the scale sizes of ionospheric features most readily visible to the GPS L1 and L2 carriers.

An additional important contribution of this thesis derives from the fact that all scintillation data drawn upon is the result of observing real world scintillation events. As such this is the first known analysis of dual frequency civilian GNSS IF sample data collected during periods of high ionospheric activity in the auroral and polar regions, including the strongest and second strongest geomagnetic events of 2008.

Consequently, significant new data has been gained containing the real world behaviour of both auroral and polar scintillation effects, which can be contrasted and compared with not only each other, but also pre-existing studies which involved single frequency digital samples collected during equatorial scintillation events. These include insights into the structure of the ionosphere, and by way of the correlation between the L1 and L2 phase, the differential effects typical in the ionosphere relative to anomaly size during polar and auroral scintillation events.

A further supporting contribution comes in the form of a design of an adjustable frequency, wide bandwidth, dual channel front-end for use in GNSS applications. During the course of the studies leading to this thesis, it became apparent that commercially available front-ends suffered from high weight, high power consumption, and extremely high cost. As a consequence, work on a lightweight, low power relatively low cost front-end was commenced by the author. When completed this front-end will be capable of providing dual simultaneous 40 MHz bands of spectrum, tuneable to anywhere between 925 MHz and 2.175 GHz,

covering all known L-band GNSS signals. Additionally, due to the very wide 40 MHz bandwidth in each channel, the simultaneous observation of GPS and GLONASS signals will be possible in both the L1 and L2 bands, while also covering the BOC (1,1) open service signal of Galileo and portions of the civilian COMPASS/BEIDOU signal bands.

iii) Objectives

Utilizing the data referred to previously a range of specific objectives is expected, including but not limited to definitive analysis of the characteristics of the observed scintillation in terms of

1) The magnitude range and correlation between the observed phase effects of scintillation between the L1 and L2 GPS carriers, from real world data.

2) Determination of optimally detectable ionospheric feature sizes via calculated L1 and L2C phase correlation combined with ray path sweep rate.

3) Design and implementation of pulsation detection methods based on the created behavioural models.

4) Development of oscillator phase noise detection methods to allow scintillation detection methods to be useable by a much broader user base.

1.5 Chapter Outline

This chapter focuses on the analysis of real world scintillation effects on legacy, and modernized GPS signals, in addition to the development of scintillation detection, and oscillator noise estimation, and mitigation strategies for use by GNSS receivers during ionospheric scintillation events.

Chapter two contains an introduction to the sources of ionospheric scintillation behaviour, the geographic dependence of these effects, and their relation to the solar cycle.

Chapter three details the criteria used to select locations for observation efforts, as well as the type and characteristics of desired GNSS data for use in subsequent analysis. Additionally, the equipment used to achieve these goals, the procedures followed in their operation, and the types and significance of data collected are also documented.

Chapter four discusses the observed effects of ionospheric scintillation captured in the collected GNSS IF data and introduces a method for using the dual frequency civilian GPS signals to determine the optimally detectable scale size of ionospheric irregularity for each phase scintillation event. An ionospheric pulsation detection method is also developed, while anomalies identified on the broadcast L1 signal of SVN48 are discussed in terms of their impact on scintillation monitoring equipment and software.

The fifth Chapter develops and discusses the methods for the use of multi-constellation multi-frequency GNSS data for the purpose of estimating, on the fly, the contributions of the phase noise in the local oscillator to the phase errors of the individually measured GNSS carriers. This novel phase noise estimation method promises to allow the use of inexpensive oscillators in future user equipment while at the same time maintaining the ability to detect, quantify, and resist the phase effects of ionospheric scintillation.

Chapter six contains the summarized conclusions and suggestions for the evolution and future work on the novel methods developed within the thesis.

Appendix A documents the design methodology behind and development of a multi-frequency, multi-constellation front-end. The development of this front-end is intended to provide to the researcher a source of multi-constellation dual frequency data, which will allow the leveraging of the (as of the time of writing) 3:1 ratio of GLONASS modernized vehicles to GPS modernized vehicles.

Chapter Two: Scintillation Effects

2.1 Definition of Scintillation

Under normal conditions the ionosphere poses little threat to the integrity or availability of navigation signals, instead appearing as only a slowly varying nuisance parameter to the vast majority of single frequency users. This nuisance parameter appears in two parts, with the first being an apparent positive user to satellite range bias, due to the propagation speed of RF signals through the ionosphere being slightly lower than the speed of propagation in free space. The second component of the nuisance parameter is the apparent advance of the carrier phase of the RF signal by an amount equal in magnitude, but opposite in sign to the effect observed on the ranging code. These effects are summarized by equations (2.1) and (2.2) respectively, with total electron content (TEC) defined in equation (2.3). Note that one unit of TEC, or TECU is defined as 10^{16} electrons/m^2 in a 1 m^2 corridor around the ray path between the satellite and user (Conley et al 2006).

$$\Delta S_{iono,g} = \frac{40.3TEC}{f^2} \tag{2.1}$$

$$\Delta S_{iono,p} = \frac{-40.3TEC}{f^2} \tag{2.2}$$

$$TEC = \int_{SV}^{User} n_e dl \tag{2.3}$$

In equations (2.1) and (2.2) ΔS_{iono} is the apparent range change in metres affecting the group or phase of the signal denoted by a subscripted g or p respectively, while *TEC* is the total number of electrons encountered by the ray path, and *f* is the carrier frequency of the signal passing through the ionosphere.

Since the ionosphere is a dispersive medium, the magnitude of the effect experienced by different carrier frequencies broadcast from the same satellite will differ, allowing properly equipped dual or multi-frequency users to directly observe and remove the typical nuisance parameters of the ionosphere from locally generated observables. While this is not necessarily possible under all conditions and causes an increase in observable noise, it is known to be a reliable method of ionospheric mitigation under normal (non-scintillating) conditions. The analysis performed in Chapter 4 will determine the extent to which this approach remains applicable under auroral and polar scintillation conditions. This derivation of ionospheric influence from dual frequency measurements was originally intended only for military users of GPS and GLONASS, as evidenced by the absence of a civilian signal on the L2 carriers of either satellite system until the most recent Block of satellites in each constellation.

Since the modernization of satellites to transmit multiple civilian accessible carriers at full strength is a recent development, the vast majority of GNSS users possess only single frequency equipment, and require other methods to mitigate normal ionospheric effects. Under typical conditions the ionosphere may be assumed to have a low spatial concentration gradient of TEC, and may be modeled well by interpolating between

widely dispersed measurement points, such as is the case for the broadcast ionospheric correction terms received from WAAS satellites (Cosentino et al 2006).

When the ionosphere is disturbed however, as depicted in Figure 2-1 the normally smooth spatial gradient assumption no longer holds. In this state the ionospheric medium gains pockets of enhanced TEC as well as relatively depleted regions. Under these conditions, two problematic consequences affect the performance of GNSS. Firstly, since the ionosphere is no longer well modeled by a single uniform infinitesimally thin shell of electron content at 350 km altitude, broadcast correction models using a two dimensional grid and the assumed wide area spatial correlation begin to break down, as do the effective ranges for differential GNSS user corrections. The second and more interesting consequence is the manifestation of effects referred to collectively as ionospheric scintillation. Ionospheric scintillation arises from the interactions of the GNSS carrier waves and the spatially varying ionosphere, as the ray path between the user and satellite changes, and the ionospheric medium moves relative to the satellite and/or user. At the edges of well defined pockets of relative TEC enhancement/depletion the magnitude of the ionospheric effects on traversing signals rapidly change. The effective addition of an instability term to the received signal phase due to rapid interaction with these pockets is referred to as ‘phase scintillation’.

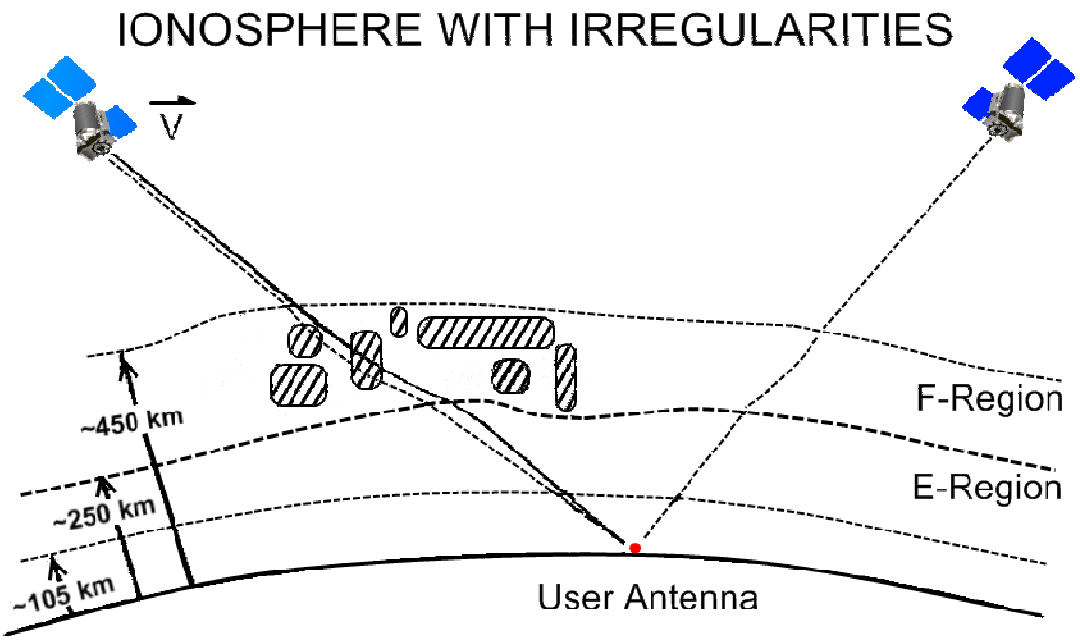

Figure 2-1: Disturbed Ionosphere with Vertical and Horizontal TEC concentrations of varying scale sizes, showing disturbances concentrated in the F-Layer of the Ionosphere (Skone 2010).

Additionally, since the propagation along different portions of the wave front between the user and satellite will encounter different levels of ionospheric group delay / phase advance along their direction of travel, the wave below the disturbed ionosphere can no longer be viewed as a single ray between the transmitting satellite and the user. Because of the differential delay/advance between the regions of differential TEC encountered, along with the slight path bending of the wave front within each region relative to free space and regions of differential concentration due to Snell's Law, different approaches may be needed to model the ionosphere in this state. Depending on the density of the enhanced/depleted TEC regions, the disturbed ionosphere may be better thought of as a series of point sources or a 'phase screen' (Béniguel et al 2004) rather than the previously considered thin shell. While traditionally applied to specular reflectors or obstructions

between a transmitter and receiver as discussed by Forssell (2003), the concept of the Fresnel zone may be applicable due to the capacity of ionospheric enhancements or depletions adjacent to but not directly in the ray path to alter the path of signal propagation. The recombination of the differentially delayed and redirected portions of the wave front at the user antenna below the disturbed ionosphere may recombine constructively or destructively, not only adding further phase instability, but potentially leading to near total destructive interference. The tendency of the signal to vary in received power level due to alternating constructive and destructive self interference following from ionospheric interaction is quantified in the amplitude scintillation index.

The quantification of the severity of scintillation effects within the GNSS field is typically encompassed by two parameters, described in depth by Van Dierendonck & Hua (2001). These Authors were involved in a company that produced commercial scintillation monitor receivers specifically to provide these parameters to interested users. The phase scintillation index quantifies the standard deviation in the change of the de-trended signal phase due to ionospheric changes, per

$$\sigma_{\Delta\phi}{}^{N} = \frac{1}{m}\sum_{1}^{m}\left[std(\phi_m^{HPF}) \right]. \tag{2.4}$$

The calculation of phase scintillation indices in equation (2.4) involves the subdivision of carrier phase in radians into *m* equal subintervals totalling *N* seconds. Since the carrier phase observable within a receiver is modified by several error sources in addition to the contribution of interest from the ionosphere, it is necessary to pre-filter the phase measurement to remove unwanted system noise contributors. The recommended filtering

approach is to filter each of the *m* sub intervals with a 6^{th} order Butterworth high-pass filter (HPF) having a 3 dB corner frequency of 0.1 Hz, per Van Dierendonck & Hua (2001). The standard deviations of the de-trended phase (denoted ϕ^{HPF}) are then averaged over the *N* second de-trending interval. In the degenerate case there may be only one sub-interval *m* of *N* seconds length. Utilizing a 60 second de-trending interval, Yu (2007) defines very weak, weak, moderate and strong phase scintillation in units of radians as being above 0.05, 0.2, 0.3, and 0.6 radians respectively.

Other researchers including Olynik et al (2002) have subsequently published confirmation that the 0.1 Hz threshold is well selected to remove the contributions of most other system noise sources, including un-modeled dynamics arising from ephemeris errors, undisturbed or 'background' ionospheric changes, and satellite clock errors. In the case of the Block IIR satellites it is noted that while the clock error values have improved, the spectra of noise from the IIR clocks has been shifted higher relative to that of the IIA vehicles. This is likely due to the addition of the time keeping system (TKS) introduced in Block IIR satellites (Garvey 2004). The notable exception to the error sources successfully removed by the simple high pass filtering is the contribution from the local oscillator, as the phase noise component of the local oscillator noise will not be mitigated by 0.1 Hz high pass filtering. As a practical constraint of this fact, hardware scintillation monitors must be equipped with a very stable external reference, preferably a double oven OCXO per Van Dierendonck & Hua (2001). For this reason, the data collected in support of this thesis was gathered using a front-end and scintillation monitor driven by a Vectron double oven OCXO.

The determination of the S4 fading index, alternatively called the amplitude fading index is calculated from GNSS in-phase and quadrature 1 ms correlator outputs, per equations (2.5) through (2.10) as described by Van Dierendonck & Hua (2001). The narrowband and wideband power, or *NBP* and *WBP* respectively, are used to determine the expected value of the signal intensity (*SI*) measure. This measure will change with time to a value over unity during constructive interference, and to a value lower than unity during destructive interference. The S4 index is then calculated using the signal intensity root variance, and an estimate of the noise density N_0 developed by the receiver to remove the contribution due to instability of the apparent received power envelope at low carrier to noise density ratios.

The Wide Band Power (*WBP*) is calculated over each bit period using the prompt in phase (*I*) and quadrature (*Q*) correlator outputs. Since the GPS signals considered herein use 50 symbols per second data rates, each bit period possesses 20 one-millisecond intervals denoted *i* such that

$$WBP = \sum_{i=1}^{20} I_i^2 + Q_i^2 \,. \tag{2.5}$$

Similarly the Narrow Band Power (*NBP*) is calculated over a one bit period interval using the in phase and quadrature prompt correlator outputs via

$$NBP = \left(\sum_{i=1}^{20} I_i \right)^2 + \left(\sum_{i=1}^{20} Q_i \right)^2 . \tag{2.6}$$

For the *k*th bit interval, the Signal Intensity (*SI*) is calculated by dividing the difference between the narrow and wide band power by the low pass filtered version of the same per

$$SI_k = \frac{(NBP - WBP)_k}{(NBP - WBP)_{lpf,k}}. \tag{2.7}$$

The total fading index, which is not compensated for carrier strength $S4_T$ is calculated over a given averaging interval, which is typically one minute, from the *SI* measurements

$$S4_T = \sqrt{\frac{\langle SI^2 \rangle - \langle SI \rangle^2}{\langle SI^2 \rangle}}. \tag{2.8}$$

In order to compensate for the expected effect of the received signal to noise level, the noise compensation factor $S4_{N0}$ is formed from the received Signal to Noise density level (S/N_0) via

$$S4_{N_0} = \sqrt{\frac{100}{S/N_0}\left[1 + \frac{500}{19 S/N_0}\right]}. \tag{2.9}$$

Combining the total fading index with the noise compensation factor to produce the *S4* amplitude fading index gives

$$S4 = \sqrt{\frac{\langle SI^2 \rangle - \langle SI \rangle^2}{\langle SI^2 \rangle} - \frac{100}{\overline{S/N_0}}\left[1 + \frac{500}{19\overline{S/N_0}}\right]}. \tag{2.10}$$

According to Yu (2007) an amplitude fading index of 0.1 is considered very weak, one above 0.4 described as weak, those above 0.6 termed moderate, and an index of 0.9 considered strong.

2.2 Latitude Dependence of Scintillation Effects

The relative quantities of amplitude fading versus phase scintillation experienced by a user are dependent on the phenomena causing the scintillation to occur, and by extension

the geographic location of the user. Scintillation effects at low geomagnetic latitudes are dominated by intense fading events with only secondary phase activity, and are discussed in Pullen et al (1998), as well as Humphreys et al (2004). The chief cause of equatorial scintillation events are the formation of ionospheric features, which become unstable following local sunset, and begin to decay as in a Rayleigh-Taylor instability problem (Moraes and Parrella 2009).

In the case of auroral scintillation effects occurring beneath the auroral oval, users will experience vigorous phase activity, but relatively limited fading compared to the amount experienced by equatorial users. High latitude polar scintillation events in general as discussed in Béniguel et al (2004) may experience both fading as well as phase scintillation activity.

In general, nearly all scintillation effects are directly influenced by the current, or former interaction between the earth and the sun, in terms of either magnetic field coupling, solar wind including charged particle flow and coronal mass ejections (CMEs), or some combination of these events as indicated in Skone (2010b).

In the case of polar scintillation, charged particles emitted from the Sun may enter along open field lines near the poles of the earth, depicted in Figure 2-2 as the vertical interplanetary magnetic field lines. Auroral scintillation may occur due to accumulated plasma in the magnetotail entering the neutral Earth atmosphere, producing the auroral oval, also depicted in Figure 2-2, and Figure 3-1. A specific example of the dependence

of polar scintillation on the state and activity of the Sun is the Coronal Mass Ejection (CME) on 10 October 2008 noted by SpaceWeather.com (2008) which was predicted to reach Earth by October 11. The CME was subsequently attributed as the cause of the October 11 geomagnetic storm by SpaceWeather.com (2008a). During this geomagnetic storm polar scintillation data was collected on multiple GPS IIR-M satellites over several hours.

For additional information the reader is directed to the previously referenced works within this chapter. It is however important to note in summary that in all cases of ionospheric scintillation, the Sun – Earth magnetic field and solar wind interactions are either the cause of, or in the case of equatorial scintillation an addition or catalyst to the causes of disruptive ionospheric scintillation. For this reasons, these interactions must be considered in any discussion of scintillation activity.

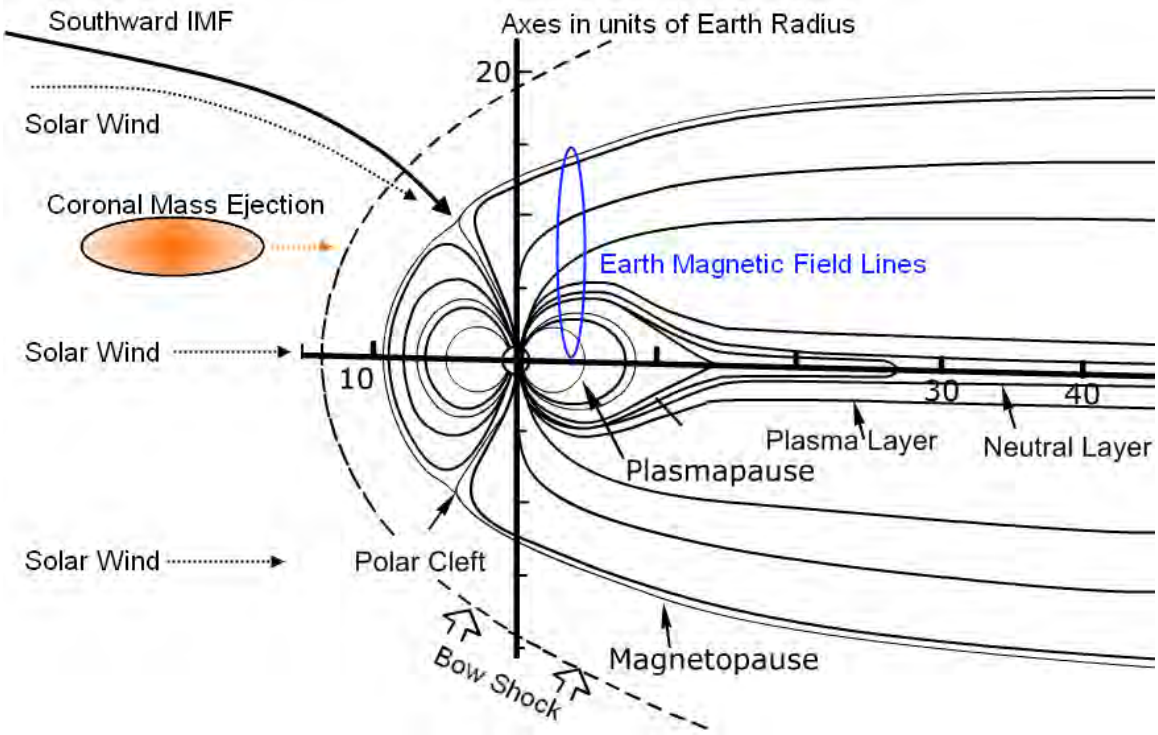

Figure 2-2: Causes of ionospheric scintillation are often directly attributable to the Sun-Earth interaction. After NAROM (2010), and Skone (2010b).

2.3 Frequency of Scintillation Occurrence

While the frequency and strength of equatorial scintillation is heavily dependent on the time of year, and time of day, the frequency of ionospheric scintillation activity at all latitudes is closely tied to the frequency of sunspot occurrence. This is due to the emissions that may occur from sunspots, both in terms of coronal mass ejections and normal plasma, as well as strong and unstable magnetic flux.

As shown in Figure 2-3 the occurrence of sunspots tends to follow an 11-year cycle of intensity, with notable but infrequent exceptions in recorded solar history including an approximately 60 year period with virtually no solar activity, referred to as the Maunder Minimum. Due to the importance of sunspots and solar activity to industrial society

because of the associated interference with satellite communications, terrestrial communication, power distribution grids, gas distribution pipelines, and even radiation exposure during high altitude travel, the sunspot cycle is closely monitored and predicted.

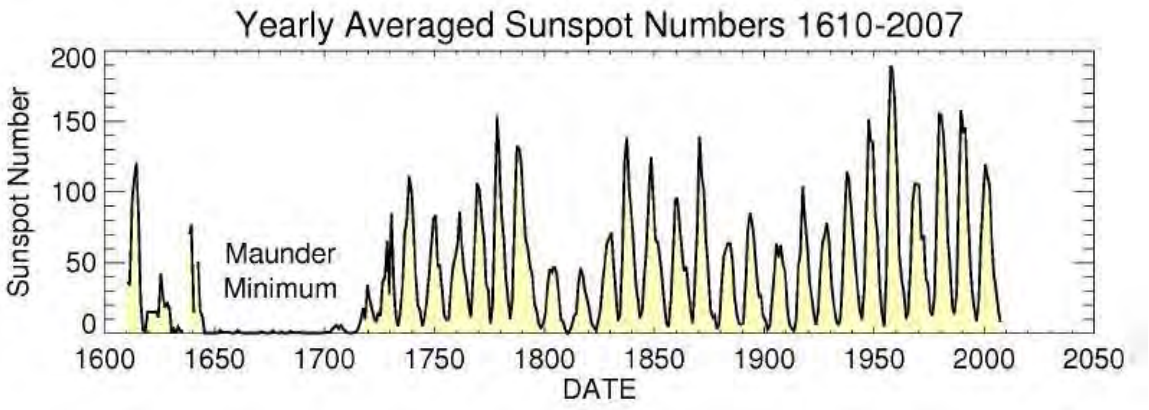

Figure 2-3: Long term behaviour of the '11 year' solar "cycle" (Nasa 2008)

During 2007 it was predicted by the NOAA that the solar activity minima had arrived, and the ascending activity portion of solar cycle 24 would commence some time during late 2007 through mid 2008, depending on the projections used. The range of predictions is shown in Figure 2-4, including 1-sigma confidence levels around both a high and low activity prediction for solar cycle 24.

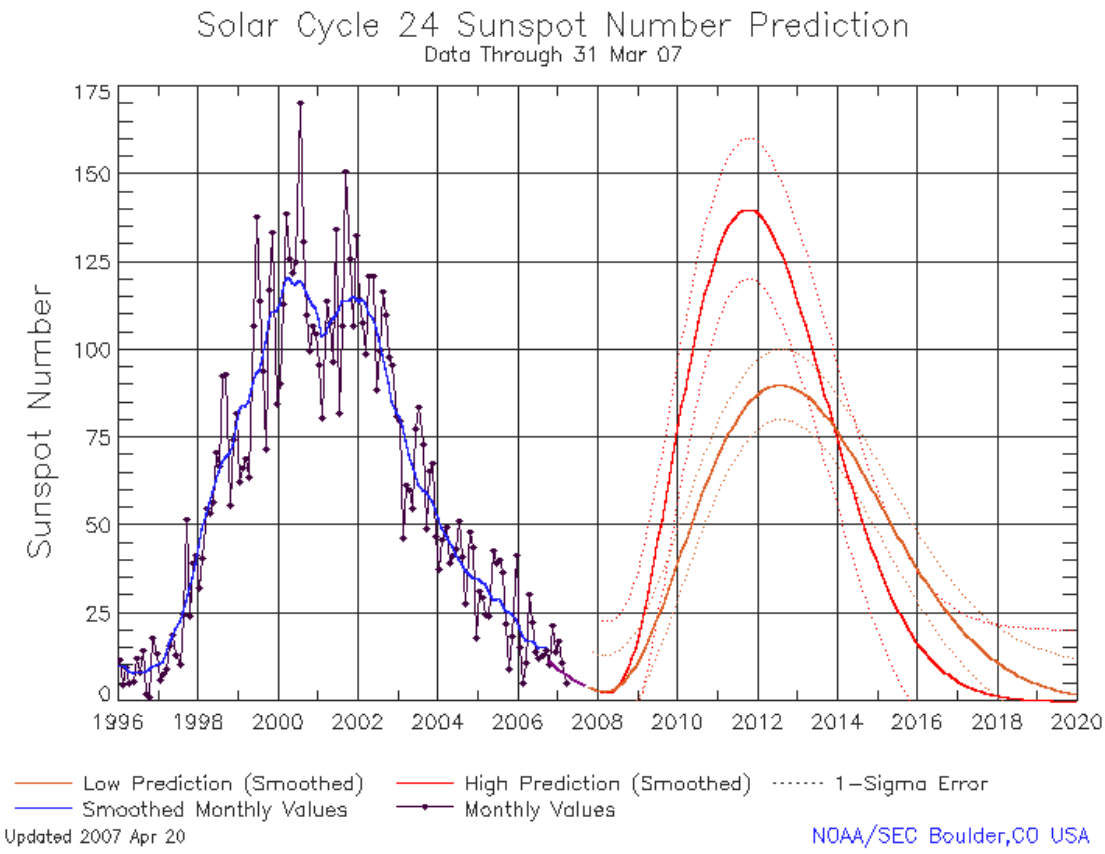

Figure 2-4: April 2007 Predictions of solar cycle 24 (NOAA 2009)

These predictions by the NOAA have since proved to be too aggressive as of the last months of 2009, whereby the solar minima had not yet been conclusively exited. Referring to the updated historical data in Figure 2-5, it can be concluded that the collection campaigns conducted during the course of field work supporting this thesis fortuitously covered the strongest events of 2008. The first of these events is the March peak in Figure 2-5 indicated by the green arrow, during which data was collected at the Churchill Northern Studies Centre in Churchill Manitoba, Canada. The second and smaller of these local maxima indicated by the orange arrow occurred during October and

November of 2008, during which data was collected at the Eureka weather station in Eureka NU, Canada.

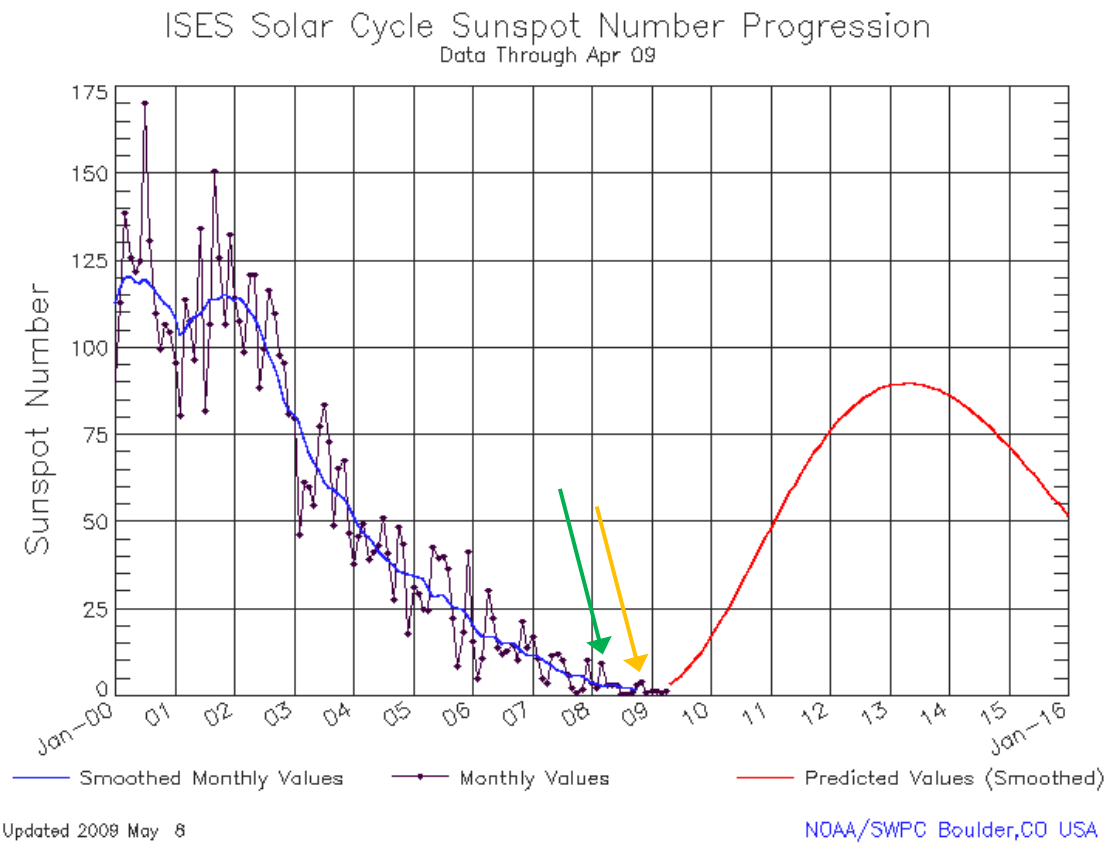

Figure 2-5: May 2009 Solar Cycle 24 Prediction Update (NOAA 2009)

Chapter Three: Data Collection Criteria, Locations, Equipment and Procedures

In this section the data collection planning, activities and equipment that provided the observations of ionospheric scintillation and pulsations will be detailed. First in terms of the initial selection criteria for the types of data to be gathered, the locations that were available and desirable to station equipment, and the equipment used, in the field.

3.1 Desired Data Collection Criteria

The desired data collection criteria involved both a primary and multiple secondary criteria. The primary criteria was the collection of IF sample data of ionospheric scintillation events from multiple strong civil carriers of a GNSS satellite.

Moving to secondary criteria, the most important of these was that the data should be collected from locations which experience frequent scintillation activity, while also collecting samples of scintillation caused by differing ionospheric conditions. Ideally this was planned to include at least one location in the polar cap region of effect, and one within the traversal path of the auroral oval. Since it was known in advance that the solar cycle was either at, or would be close to minimum when the data collection efforts were being planned, the location selected for collecting data in the traversal path of the auroral oval would have to be at higher latitude than Calgary. Calgary seldom experiences disturbed ionospheric effects during solar minima.

In Figure 3-1 it is apparent that a collection location at roughly 60^{o} latitude is necessary to make an overhead pass by the southern extent of the auroral oval during a non disturbed or slightly disturbed evening a likely occurrence. This restriction would allow the use of multiple Canadian cities including Yellowknife and Churchill. In contrast, collection from the polar cap region would necessitate the use of a position on Ellesmere Island, which possesses very few potential bases to operate from.

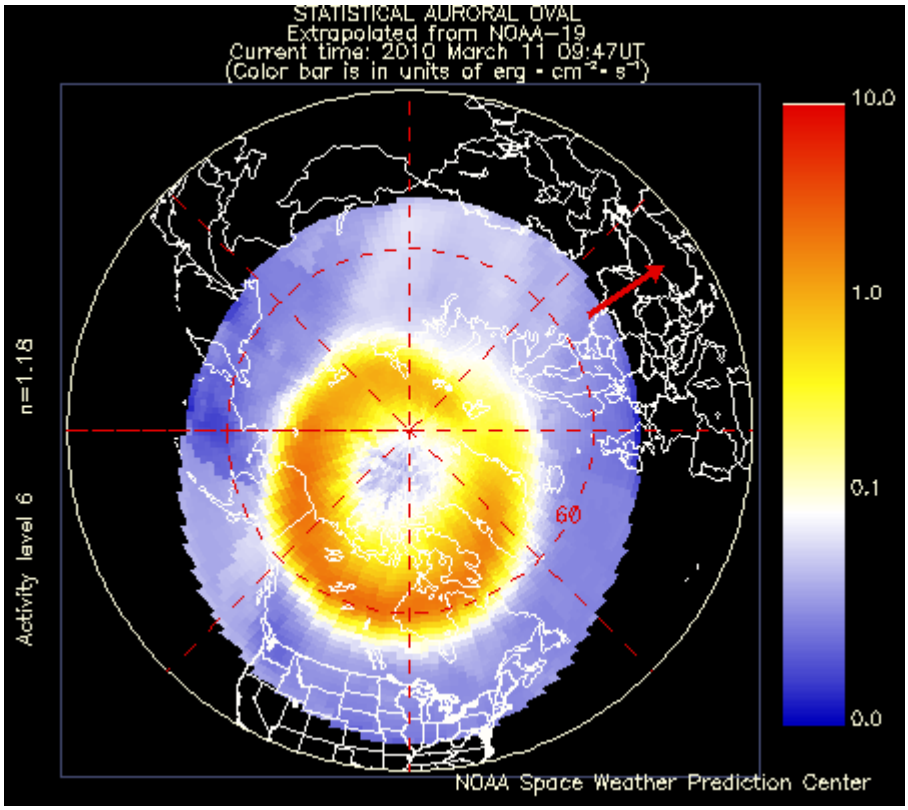

Figure 3-1: Auroral Oval extent for the evening of March 11 2010 clearly showing the auroral oval, polar cap, and sub auroral zones (Space Weather Prediction Centre 2010).

3.2 Selected Data Collection Locations

The selection of the first data collection location ended promptly when it was discovered that the Churchill Northern Studies Centre located outside of Churchill Manitoba Canada at approximately 60^{o} latitude could provide a convenient, heated, powered and otherwise sheltered environment for equipment and operator alike, at minimal cost. The author promptly arranged and executed a one week collection campaign between March 24^{th} and 28^{th} 2008, which fortuitously coincided with elevated solar and geomagnetic activity levels. The selected antenna deployment position during the Churchill collection effort is shown in Figure 3-2.

Figure 3-2: Antenna placement by the author on the roof of the Churchill Northern Studies Centre, a former support building for the Churchill rocket range components of which can be seen in the distance.

In terms of the polar cap collection site, it is not accurate to say that the author selected the collection site, but that the collection site administrators selected the author. The author was honoured to be selected as the 2008 recipient of the 'Research Support Opportunity In Arctic Environmental Studies' award. This award, administered by the Association of Canadian Universities for Northern Studies (ACUNS) allows one researcher per year to conduct experimental activity at the Eureka High Arctic Weather Station. The weather station is located at 80^{o} North latitude on Ellesmere Island, with core staffing of Environment Canada personnel, and research support staff and facilities from the Canadian Network for Detection of Atmospheric Change (CANDAC). The extraordinary support provided by Environment Canada and CANDAC unexpectedly provided a rare opportunity to personally conduct data collection in the polar cap region, and made the de facto choice of polar locale Eureka. The author conducted a two month data collection effort at this location spanning early October through November 2009. A photograph of the author at one of the potential antenna placement sites located on the roof of the CANDAC 'Pearl' station atop a small local mountain is shown in Figure 3-3.

Figure 3-3: The author at one of the potential antenna placement sites on the CANDAC Pearl lab roof. This location was not selected due to the long distance (14 km) between this site and the main base.

3.3 Data Collection Systems

During the Churchill data collection effort, the antenna shared by the front-end and the GPS Silicon Valley/ AJ Systems GSV4004 commercial Ionospheric Scintillation Monitor (ISM) was mounted on the roof of the Churchill Northern Studies Centre at coordinates 58.73° N 93.82° W. During the Eureka collection period the antenna was placed on top of the CANDAC sapphire lab located adjacent to the Eureka High Arctic Weather Station at coordinates 80.00° N 85.95° W. The physical arrangement of this equipment is shown for the auroral collection efforts in Figure 3-4, while each of the important system elements are discussed below and shown in Figure 3-5.

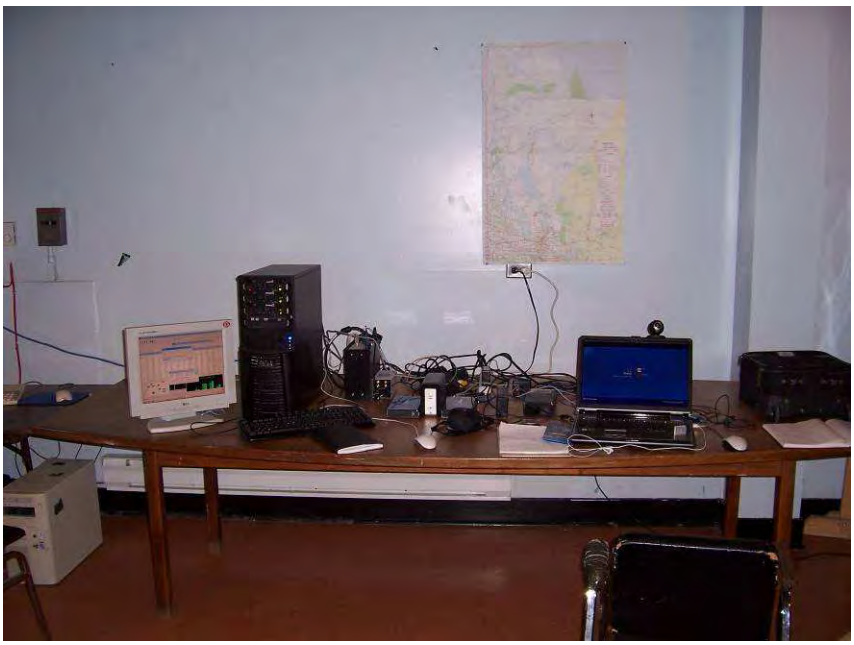

Figure 3-4: Data collection setup as deployed during the Churchill collection effort.

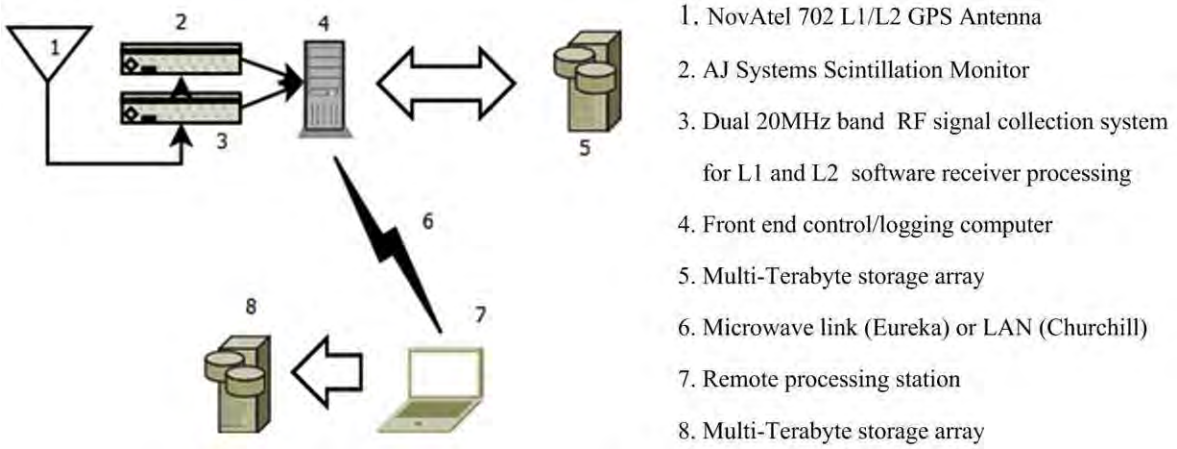

Figure 3-5: Data collection setup used at the Churchill Northern Studies Centre between March 24 and 28, and at the Eureka Weather Station (CANDAC Sapphire Seatainer lab) between October 6 and November 29, 2008.

In both instances of data collection, the hardware was set up to collect data simultaneously using both a commercial scintillation monitor, as well as a co-located high bandwidth L1/L2 GPS front-end and logging PC. Both the scintillation monitor, and front-end were driven from a common NovAtel 702 pinwheel antenna. The front-end is in this case a composite system developed by the PLAN Group for general data collection as well as ionospheric monitoring, which consists of a specially modified NovAtel Euro 3M receiver, an Altera FPGA board, and a National Instruments data acquisition card within a desktop PC. The NovAtel Euro 3M receiver contains a customized FPGA configuration which routes the IF bit stream from the receiver RF and digitization section to the Altera FPGA board, where it is packed into 32 bit double-words of data for transfer via the NI-DAQ card to the PC storage array.

The data output by the GPS front-end, detailed in Table 3-1 includes the GPS L1 and L2 bands including approximately 1565-1585 MHz and 1217-1237 MHz respectively. By storing these digitized frequency bands to disk, the collected scintillation data was thereby made available for subsequent post processing and analysis using the PLAN group GSNRx^{TM} software GNSS receiver.

Table 3-1: GPS Front-End specifications and data outputs

Channel	I	II
Sample Rate	20 MHz	20 MHz
Sample Format	I/Q Pairs	I/Q Pairs
Sample Resolution	2 Bits per sample	2 Bits per sample
Band Centre	L1 GPS (IF Mag. 0.58 MHz)	L2 GPS (IF Mag. 0.10 MHz)
Data Output	80 Mbit/second	80 Mbit/second

Software on the logging PC, previously developed by the PLAN Group, would collect and store the packed sample data on the storage array in files containing 1 minute of interleaved L1 and L2 data per file. While the data could also be stored as one continuous file, division into 1 minute segments aided efficient data retention.

3.4 Data Collection Procedures

In the case of the Churchill collection effort output from the scintillation monitor was observed in near real time by the author via a custom created visualization program, to select events and satellites of interest. This was accomplished by showing the elements seen in Table 3-2 for each PRN in view once per minute on the system screen. The importance of this data is that it provided an indication that scintillation was affecting the received GPS signals, including the S4 and $\sigma_{\Delta\phi}$ indices introduced in Chapter 2.

Table 3-2: ISMRA log contents displayed for each PRN in view once per minute. Note that all scintillation indices from the AJ systems ISM are produced with a 1 minute de-trending interval

PRN	Azimuth	Elevation	L1 C/N_0	S4	$\sigma_{\Delta\phi^1}$	$\sigma_{\Delta\phi^3}$	$\sigma_{\Delta\phi^{10}}$	$\sigma_{\Delta\phi^{30}}$	$\sigma_{\Delta\phi^{60}}$

Events of interest in the ISMRA reports were used to identify which segments of logged high-rate IF sample data would be retained for post-processing in by the software receiver.

Due to issues of fatigue, this process was substantially automated for the subsequent, much longer Eureka data collection expedition. In this case ISMRA (at 1/60 Hz) data records from the scintillation monitor were collected on the front-end logging PC, and processed once or more daily by the operator to identify data segments of note. In this way it was possible to collect long, continuous segments of data without continuous operator supervision.

During both deployments data was collected during local evening hours through the early morning hours of the following day, or during times of forecast ionospheric disturbance. In Churchill this was typically done between local 23:00 hours and local 04:00 hours the following day. Due to the substantially lessened operator requirements gained through automation, the collection hours in Eureka often spanned from 20:00 hours local to 07:00 hours the following day. In the case of forecasted events during the Eureka polar collection (e.g. Oct 9-10) it was possible to collect for nearly 24 consecutive hours before element 5 in Figure 3-5 (Multi-Terabyte storage array) reached usable capacity.

Data selection for retention and further processing was based on the assessments of the co-located Ionospheric Scintillation Monitor, which indicated the phase scintillation and S4 indices of scintillation magnitude.

The selection criteria for data acceptance was narrowed to accept only events recorded by the ISM from satellites above certain elevation thresholds, while also meeting secondary criteria for the intensity of the phase scintillation indices that would be considered

indicative of noteworthy scintillation activity. IF sample data from the minutes identified as containing scintillation as well as the preceding and following minutes of IF sample data were retained. As such, the minimum length of retained IF sample data surrounding an event would ideally be 1 minute both before and after the event, as well as the minute containing the event. The specific thresholds used by the author divided the sky into three elevation bins, A, B and C. The respective elevation ranges were {over 45^o, 35^o to 45^o, 30^o to 35^o} with minimum thresholds of phase scintillation in radians set as {0.4, 0.7, 1.5} respectively. The basis of these criteria was the published behaviour of the scintillation monitor provided in Van Dierendonck (1999) as well as previous analysis by the author of the data produced by this type of scintillation monitor.

An additional restriction was placed on the range of PRNs for which data would be retained, to be those that were assigned to GPS satellites transmitting dual frequency civil codes. The motivation behind the exclusive use of signals broadcast by Block IIR-M GPS satellites is twofold, with the first being the simple lack of field portable equipment capable of logging the far more numerous GLONASS dual frequency observations simultaneous to those of GPS. While the author has attempted to overcome this limitation via the front-end development documented in Appendix A, the data utilized in this study was collected up to two years prior to the design of this new front-end. The second, and more important motivation behind the use of only L2C capable GPS satellites rests in the desire to address questions as to the relationship between scintillation effects on multi-frequency GNSS. Included in these open questions are the correlation, or lack thereof, between the presence of phase scintillation on the L1 and

L2C carriers, in addition to the correlation between the fading effects experienced by the two carriers. While it has been previously established that a negative correlation of roughly 60% exists between the phase and amplitude scintillation effects on the L1 carrier as indicated in Yu et al (2006), the relationship between phase and fading across carriers is a relative unknown. Some respected researchers including Psiaki (2007) have indicated that high correlation between fading effects on the two carriers is expected for equatorial users, without providing insight into expected behaviour at higher latitudes. The interrelation between the phase effects observed on the L1 and L2C GPS carriers are discussed in depth in the subsequent chapter.

Chapter Four: Scintillation Characteristic Analysis and Detection Method Development

The goal of this chapter is to identify the level of correlation of ionospheric phenomena affecting the GPS L1 and L2 civil signals, as well as to quantify the scale sizes of disturbed ionospheric activity detectable during scintillation events at low arctic as well as polar latitudes. To accomplish this goal, the analysis of available data is subdivided into four sequential tasks shown in Figure 4-1.

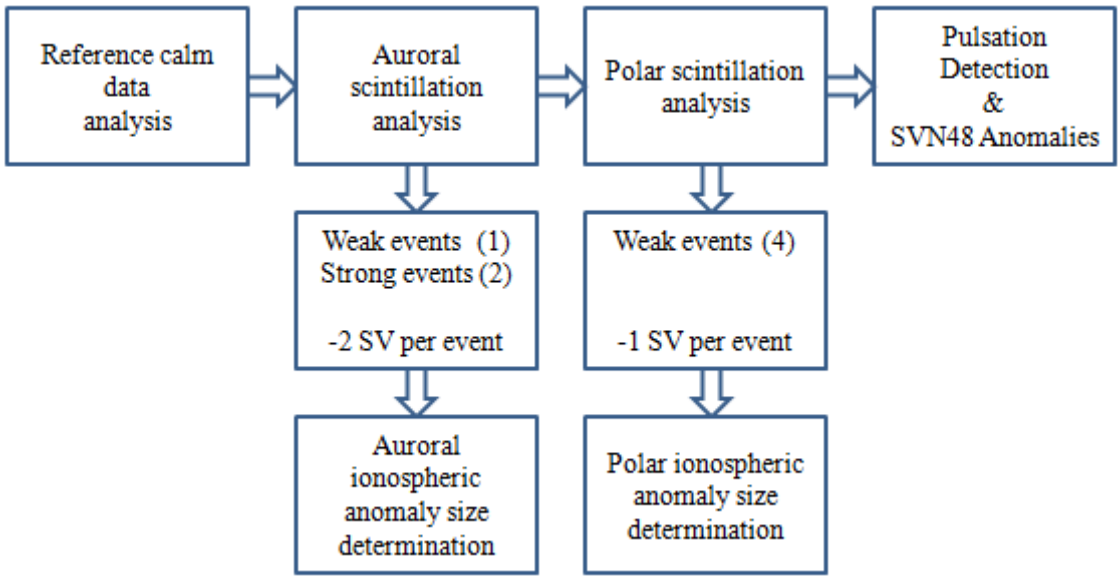

Figure 4-1: Data Analysis Tasks

The analysis of each data set is subdivided into four categories that will be investigated in order, starting with consideration of the ionospheric conditions at the times of observation through the use of space weather and local magnetic field measurements for auroral data, and the use of forecasting services in the case of polar data. The second category of analysis is the examination of the behaviour of the ionosphere as measured

with dual frequency civilian GPS observations, as well as the production of phase scintillation indices from each carrier individually to further quantify the level of activity in the ionosphere. Thirdly, the de-trended L1 and L2 GPS carriers will be compared to identify any signal features of interest. The fourth and final category of consideration will be to determine the level of correlation between the ionospheric influence on the L1CA signal and that present on the L2C signal. This correlation is calculated in terms of the spectra of the ionospheric disturbances identified, and subsequently mapped into the physical feature size within the ionosphere that this frequency content represents for a given satellite ray path velocity.

4.1 Reference Calm Data Analysis

Since each of the auroral scintillation events considered was accompanied by significant visible aurora, and since it is known that aurora borealis are caused by substorm events (Skone 2010b), it was appropriate to consider the space weather and local magnetic conditions that typically accompany these events. The parameters considered were therefore the magnitude of the solar wind velocity preceding the observations of interest, the strength and direction of the interplanetary magnetic field prior to the disturbance, and the local magnetic field variation before and during ionospheric scintillation events. Both the Interplanetary Magnetic Field (IMF) and solar wind velocity measurements used are produced by the Advanced Composition Experiment (ACE) satellite, which was launched in 1997 to provide this data (CIT 1998).

To serve as the point of comparison, data was collected from a modernized Block IIR-M satellite broadcasting two civil signals (L1 C/A and L2C) at a moderately high elevation angle during a period of solar and ionospheric calm. Beginning with the space weather conditions during the reference data set, the solar wind velocity during the July 18th reference data set is shown in Figure 4-2. The solar wind is an important indicator of present or future disturbed ionospheric conditions as the higher the velocity of the solar wind towards Earth, the more rapidly charged particles will interact with the Earth's magnetic field, as described in SWPC (2010). Typical velocities for the solar wind are between 300 and 800 km/second according to Hathaway (2007), placing the reference case in Figure 4-2 at the low end of the expected range of values, commensurate with calm conditions.

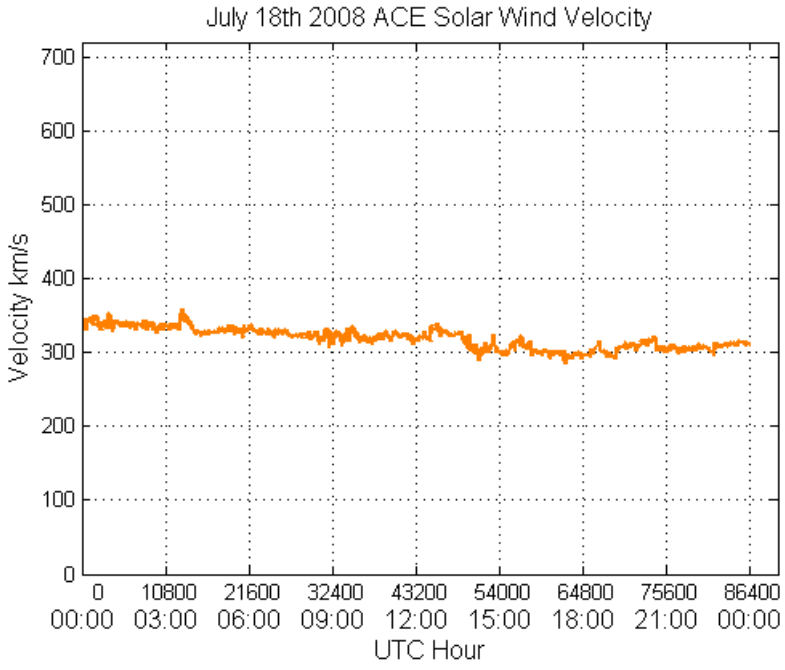

Figure 4-2: July 18th 2008 solar wind velocity towards earth, as reported by the ACE satellite (ASC 2010)

Finalized IMF data recovered from the ACE satellite for the entirety of March and July 2008 is listed as ‘not available’ through some automated plotting services including (NOAA 2010). It was however possible to retrieve this data by processing the level 2 HDF (Ullman 1999) files from the ACE satellite containing the periods of interest.

Decoding the available HDF data files from the ACE mission for the days of interest in this study yields data that appears to contain many gaps and artifacts which cannot be explained, including periodically repeating IMF values of exactly -1000 nT at fixed intervals. Since this value is absurd in the context of IMF, in addition to being perfectly repeated, it is not possible to attribute these data features to actual observations. The presence of these anomalies may indicate why this data has not been made available for automated plotting in the two years following collection. To work around this unfortunate reality, the obvious anomalies are interpolated through. The data as it appears for the reference case after interpolating through and thereby eliminating obvious data anomalies is shown in Figure 4-3.

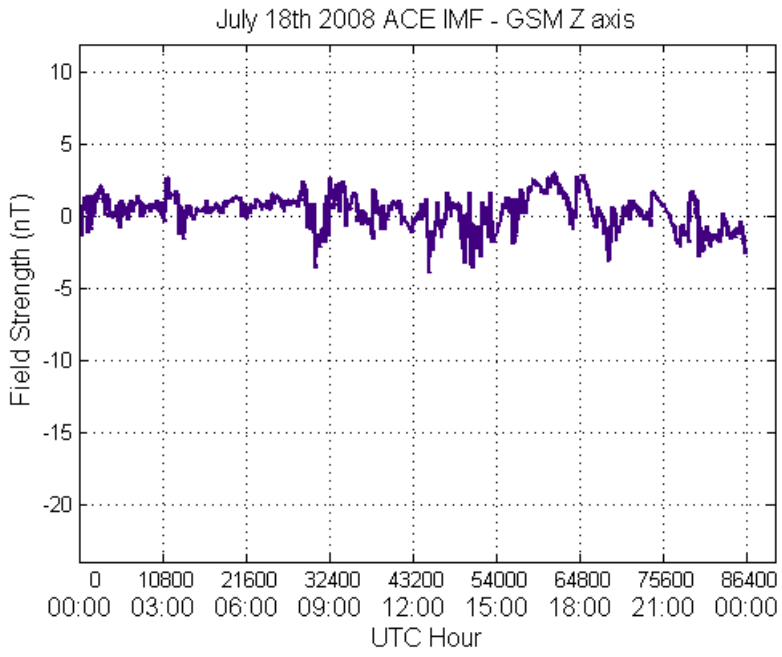

Figure 4-3: July 18th 2008 Interplanetary Magnetic Field (IMF), as reported by the ACE satellite (ASC 2010)

While the data must be viewed with some caution due to the necessary manipulation to remove obvious errors, the data in Figure 4-3 does indicate stable, low magnitude, primarily Northward (positive) interplanetary magnetic field data with a mean value of 0.293 nT. Since charged particles in the solar wind are inhibited from directly entering the Earth atmosphere by a northward IMF, this observation is again consistent with calm ionospheric conditions.

Local magnetic field change over time data in Figure 4-4 was taken from the Meanook Alberta magnetic observatory, via the Geological Survey of Canada plotting service. Meanook Alberta is approximately 400 km North of Calgary, but is still indicative of calm magnetic conditions.

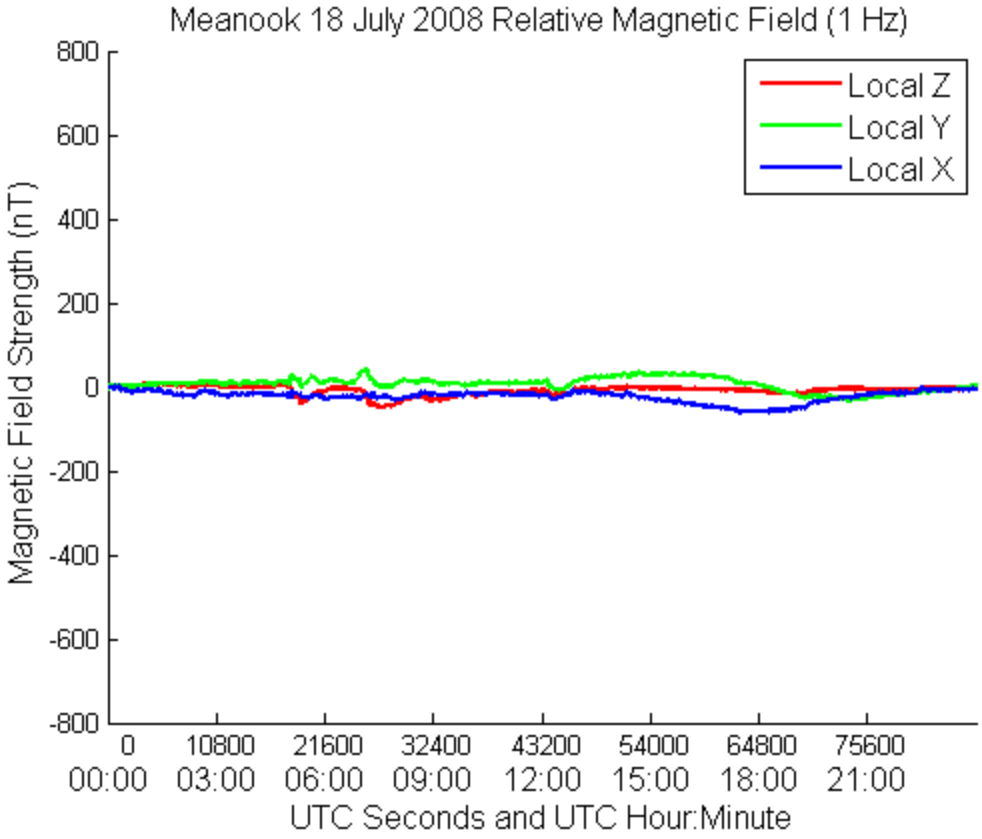

Figure 4-4: Geomagnetic field change versus time observed at Meanook AB, July 18, 2008 (Natural Resources Canada 2010)

While the absolute magnetic field data shown in Figure 4-4 does indicate variation during the first half of the day on July 18th, the latter half, during which the reference GNSS observations were collected is stable, with maximum rates of change in magnetic field less than 8 nT per minute at all times and lower still during the collection of the auroral GNSS scintillation observations.

Moving to the analysis of Ionospheric change using GNSS observations, the ionosphere is, as discussed in Chapter 2, a dispersive medium. As a consequence, the use of multi-

frequency observations from the same satellite enables direct computation of the change in TEC encountered over the observation interval. Under the assumption that both carriers encounter the same charge distribution between the satellite and user, this dual frequency measurement approach allows the removal of the vast majority of ionospheric influence from the resulting observations. For a thorough treatment of the observation of higher order ionospheric effects which are much smaller in magnitude, but not observable using only two carriers, the reader is directed to (Wang et al 2005). To calculate the first order variation of the ionosphere using the L1 and L2 phase observations, one must form the difference between the L2 and L1 carrier derived Accumulated Delta Range (ADR) in unit of length (metres here), and divide the result by a constant. The ADR is the change in satellite to user range over the observation interval as measured using the GNSS carrier.

To calculate the constant factor which converts the ADR difference between L1 and L2 GPS observations to TEC variation, recall from Equation (2.2) that for GPS L1 the apparent range change caused by 1 TECU of electron content will be 0.162 metres, while the same quantity of charge will cause a change of 0.267 metres on GPS L2. Therefore the constant factor is 0.105 with units of metres/TECU resulting in the following expression for the ionospheric variation in units of TECU:

$$TEC = \frac{\phi_{L1} - \phi_{L2}}{0.105}. \tag{4.1}$$

This formulation requires that the sign convention used for phase or ADR change within the receiver be defined such that the phase change reported due to satellite motion is of

the same sign as the pseudogrange change value, such as is the case with the GSNRx™ software receiver.

Since the phase observables provide only range change values and not absolute range measurements, they are used to determine the change in the ionosphere over the interval of observation rather than the absolute value of TEC encountered by the signals. For the July 18 2008 reference case this TEC variation over the observation interval calculated using equation (4.1) is seen in Figure 4-5, where it is plotted on axes that will later allow direct comparison between this reference data and the auroral scintillation events.

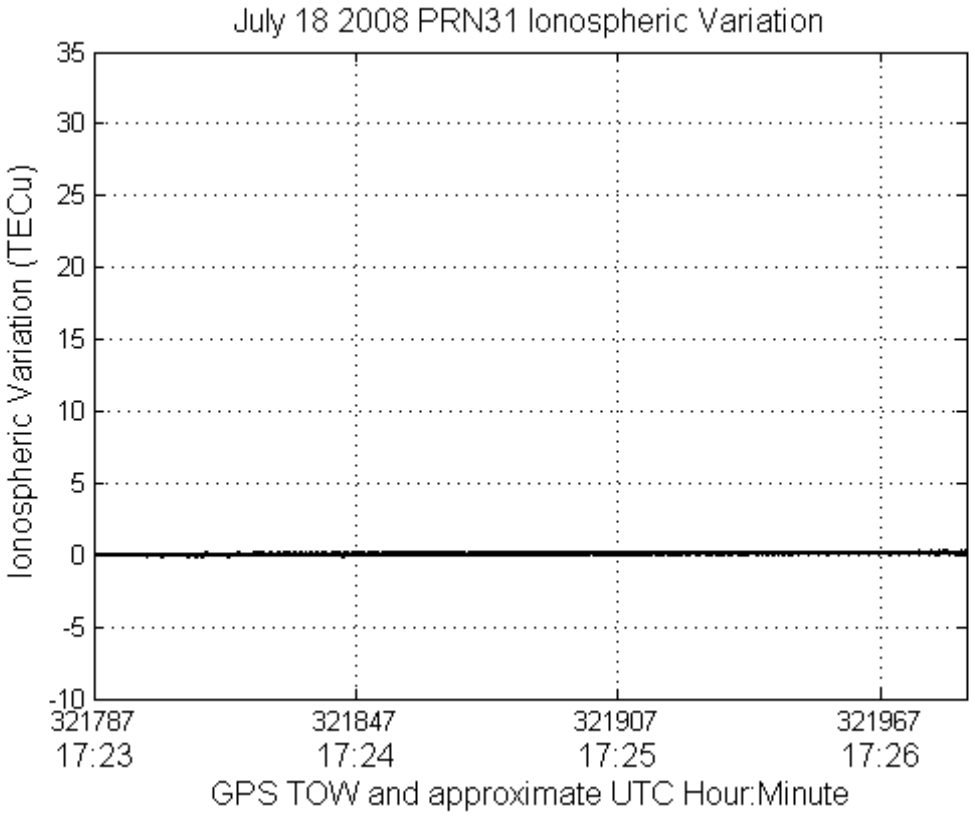

Figure 4-5: Ionospheric change over the reference data interval. Satellite descending from approximately 60.5 to 60.2 degrees elevation is likely responsible for the very slight increase in measured TEC

In Figure 4-5 it is apparent that the levels of TEC observed by the dual frequency GPS measurements are nearly constant during the observation period, representing a total change of less than 0.2 TECU over the course of the data set. The variation that is present is a minute but steadily trend higher in magnitude, likely due to the slowly decreasing elevation angle to the satellite.

Since it is desired to examine not only the variations in the TEC levels during ionospheric disturbances but to also investigate potential methods of quantifying the correlation between carriers during these disturbances, it is important to understand how these variations influence the individual carriers. While the calculated TEC provides an insight only to the relative variation of the carrier pair, it is useful to also analyze the absolute variation of each carrier, as is plotted for the reference data set in Figure 4-6.

Since it is desired to analyze the low frequency content of the carriers in addition to higher frequency components, it is necessary to first de-trend the carrier phase data to allow visualization of relatively small variations, without eliminating potential low frequency features. In this case an averaged polynomial fit to the two carriers is produced, and applied identically to each so as not to modify the TEC information contained in the relative changes between the carriers at either short or long time intervals.

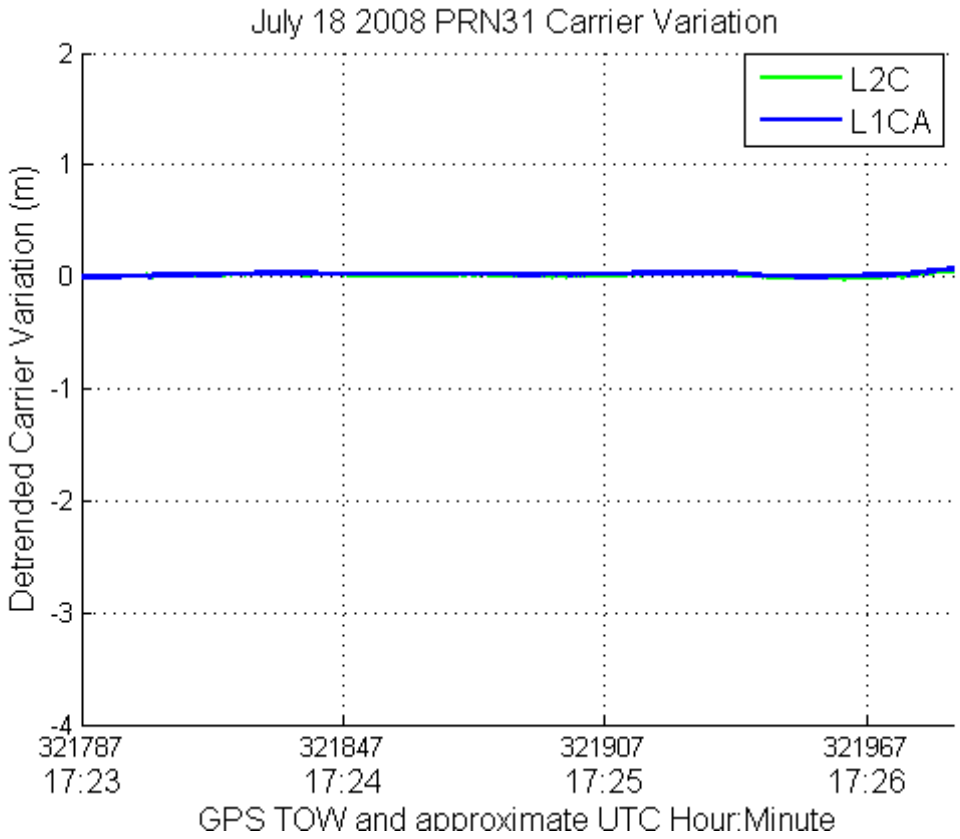

Figure 4-6: L1 and L2C carrier variation over the reference data interval. Slight common mode variation is believed to be due to tropospheric effect.

Over the period of observation an absolute range variation of -2 to +7 centimetres is not exceeded by either the L1 or L2 carriers. Once more the large plotting range has been selected to allow direct comparison with subsequent plots of active data sets. Since the changes that are present in the carriers that remain after considering the ionosphere are virtually identical, it is assumed that these are tropospheric or satellite/user clock variations. Multipath would also possess time varying magnitudes and relative signs between the L1 and L2 carrier phase observations which is not apparent when closely observing the data at a high magnification.

Under these calm conditions, it is of no surprise that ionospheric phase scintillation indices calculated using the reference data and plotted in Figure 4-7 show very low values of activity for both the L1 and L2C carriers. These indices are calculated utilizing the methods introduced in Van Dierendonck et al (1993) and further elaborated in Van Dierendonck & Hua (2001), but using a 6 second de-trending interval as opposed to the typically discussed 1 minute de-trending interval. One additional difference is the use of the polynomial de-trended phase observations as a starting point, rather than the raw carrier phase measurements.

Utilizing the already de-trended carriers as a starting point, the phase observations in units of radians are low pass filtered by a sixth order Butterworth filter, implemented as three iterations of a 2^{nd} order filter with a cutoff frequency of 0.1 Hz. The low pass filtered carrier is computed, and subsequently divided into 6 second intervals. Each of these intervals is subdivided into 6, 3, 2 or 1 equal units of 1, 2, 3, or 6 second length sub-intervals respectively, with the standard deviation being calculated on each sub-interval. The standard deviation values are finally averaged over the 6 second interval, producing the phase scintillation index ($\sigma_{\Delta\phi}$) for the given 6 second interval. This process is repeated independently for both the L1 and L2 GPS carrier phases.

The plot in Figure 4-7 is the degenerate case where the sub-interval length is equal to the de-trending interval length of 6 seconds. An important additional precaution that is not included in the source references is the elimination of initial offsets from the phase data series, as well as the identification of potential cycle slips. Since the carrier is already de-

trended using a polynomial fit, any cycle slips are visually obvious when viewing a plot of carrier variation with time.

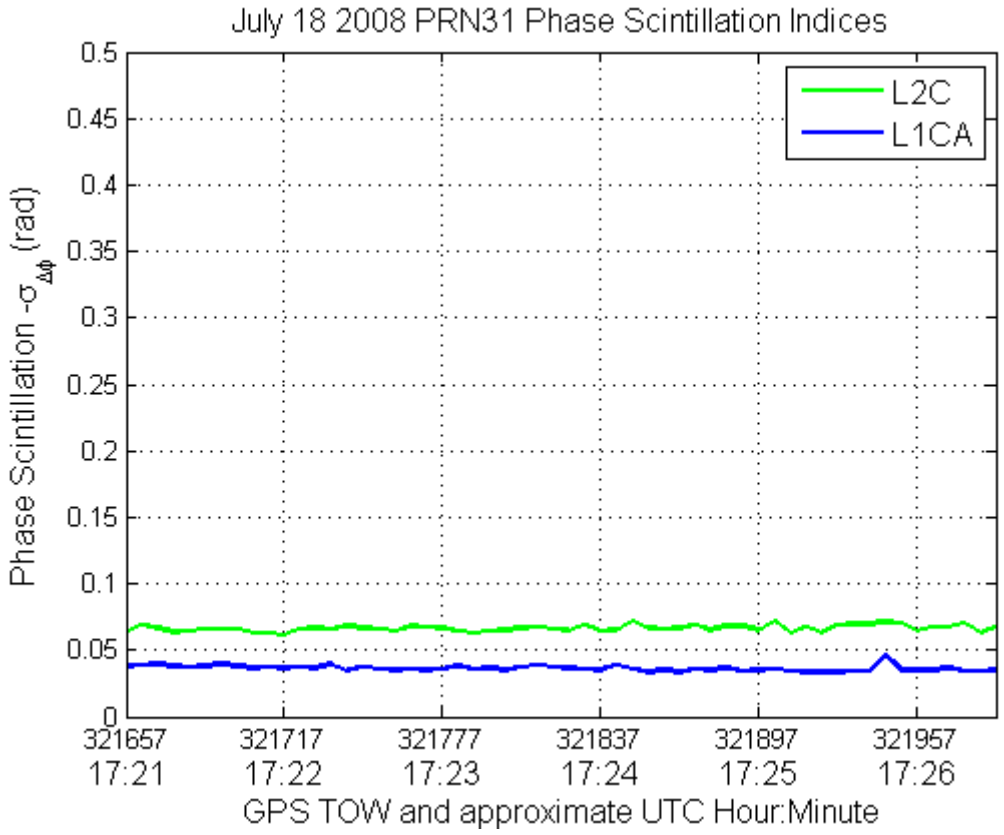

Figure 4-7: Phase scintillation indices over the July 18th 2008 reference data interval. Higher levels on L2C are due to lower L2C carrier power, antenna gain pattern, and GSNRx™ implementation.

The uniformly higher level of phase activity measured by the L2C signal carrier is in this calm data set strictly a function of the lower C/N_0 of the L2C carrier relative to L1CA, and associated increase in carrier phase noise on L2 relative to L1. The reduced apparent carrier strength is due to a combination of the 1.5 dB lower broadcast signal strength (IS-GPS-200D 2004), the discarding of 3dB (half) of the received signal power due to the GSNRx™ software receiver using a pilot only tracking strategy for the L2C signal, and

the 2.5-3.5 dB lower antenna gain pattern at L2 (NovAtel 2010). The important consideration that is drawn from this is that the carrier power reduction by approximately 7 dB relative to L1CA results in only a small increase in the phase scintillation index.

4.2 Auroral Scintillation Analysis

Having established a set of reference data for calm ionospheric conditions in the previous subsection, examination of the same parameters during periods of disturbed ionospheric conditions will now be considered. In each of the auroral cases, the local ionospheric conditions were known a-priori to be disturbed due to the visible presence of brilliant auroral displays during the period of data collection, an example of which is shown in Figure 4-8.

Figure 4-8: Visible aurora on 26 march 2008. Similar displays were seen during all periods of observed auroral phase scintillation.

Phase scintillation activity was also noted by the co-located scintillation monitor as described in Chapter 3, often times indicating scintillation activity on satellites with

azimuth and elevation coordinates in the same vicinity of the sky as the visible aurora, indicating correlation of the visible and L-band observations. Having established the quiet parameters that will be used for comparison, auroral events containing scintillation will now be investigated starting from weak through to very strong phase scintillation.

4.3 Analysis of Weak Auroral Scintillation - Event A:

The weakest auroral event in terms of the observed phase scintillation captured by L2C enabled satellites was interestingly one of the best fits to the space weather and local magnetic parameters that would be expected during a substorm event. Solar wind for this event is depicted in Figure 4-9. Comparing the solar wind speed on the day of event observation with that of the reference data collection, it is apparent that the velocity of the solar wind has roughly doubled. Because the source of the data is a satellite that is more than 1.5 million kilometres from Earth (CIT 1998), there is a lag between data as shown in Figure 4-1 and the interaction of the solar wind with the earth of approximately 45 minutes given the average velocity of the solar wind for this day.

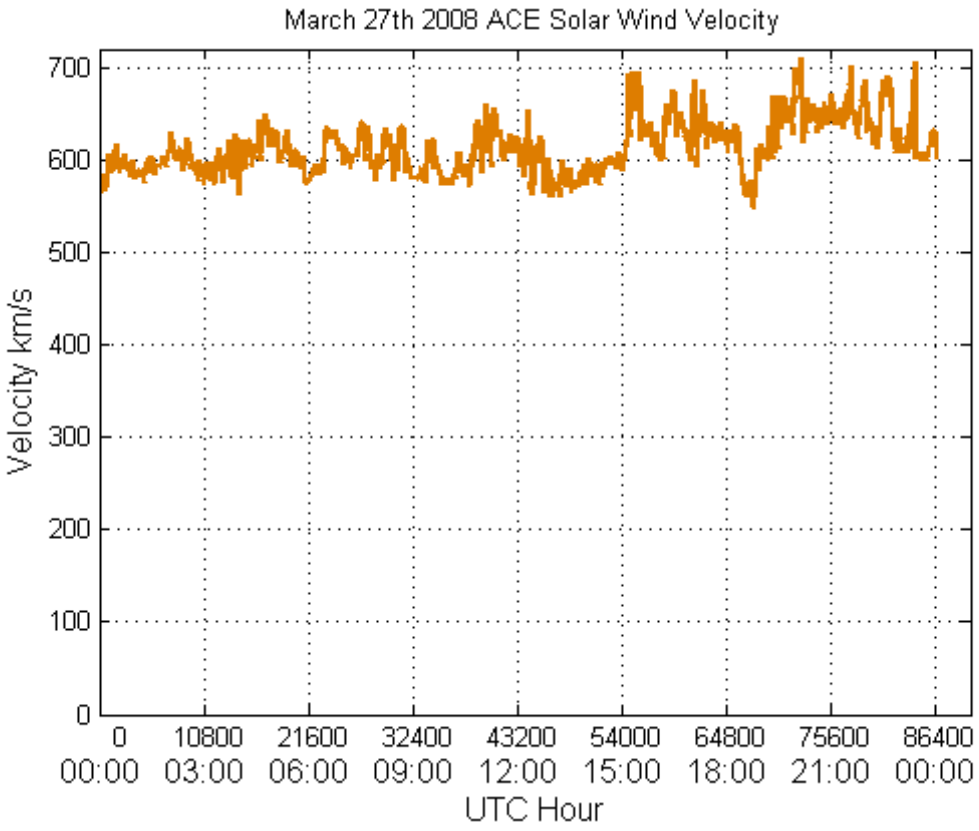

Figure 4-9: March 27th 2008 Event A Solar Wind Velocity towards earth, as reported by the ACE satellite (ASC 2010)

Having already stated the reasons for viewing the ACE magnetometer data from the periods of interest with some scepticism, the IMF during the first scintillation event is depicted in Figure 4-10.

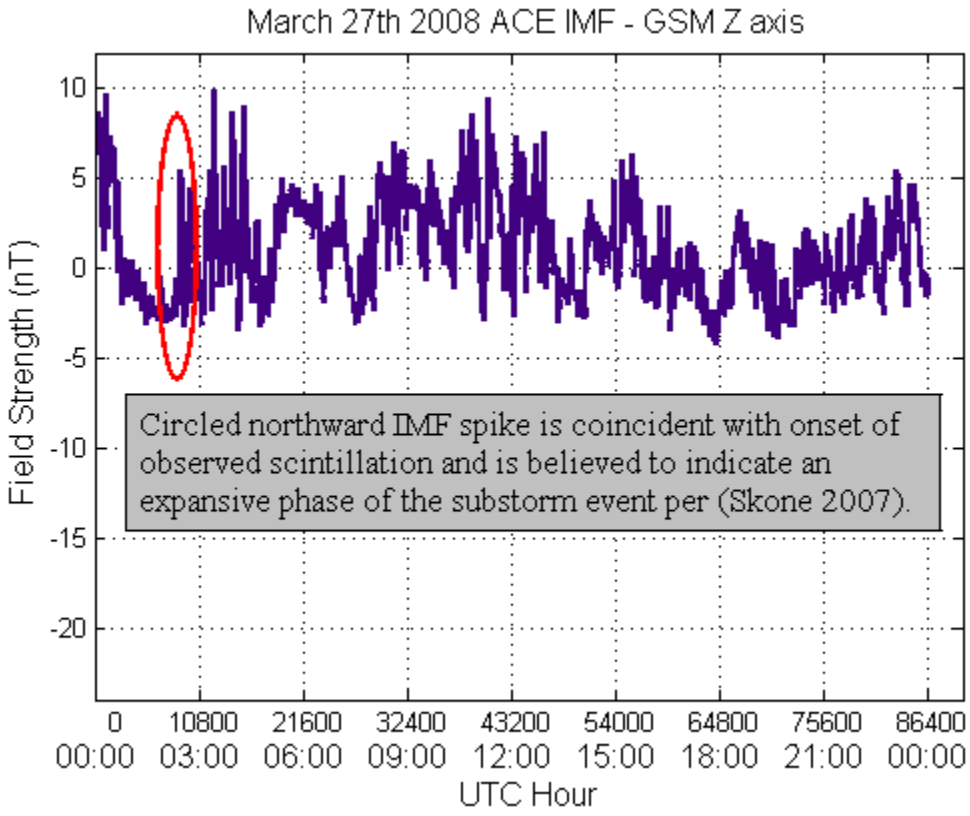

Figure 4-10: March 27th 2008 Interplanetary Magnetic Field, as reported by the ACE satellite

Contrasting this 24 hour period of IMF data with that collected on the reference calm day indicates that the IMF does turn northward almost immediately prior to the event as would be expected during a substorm recovery phase (Skone 2007). Additionally the field also has much higher overall volatility on March 27th than it did on July 18th 2008.

Similarly the local magnetic field observations at Churchill during the disturbed conditions are much more volatile than during the reference data set. To better relate the short term volatility, this magnetic field change over time information is plotted in Figure

4-11 at 1 Hz, and indicates much higher activity as opposed to the reference magnetic data in Figure 4-4.

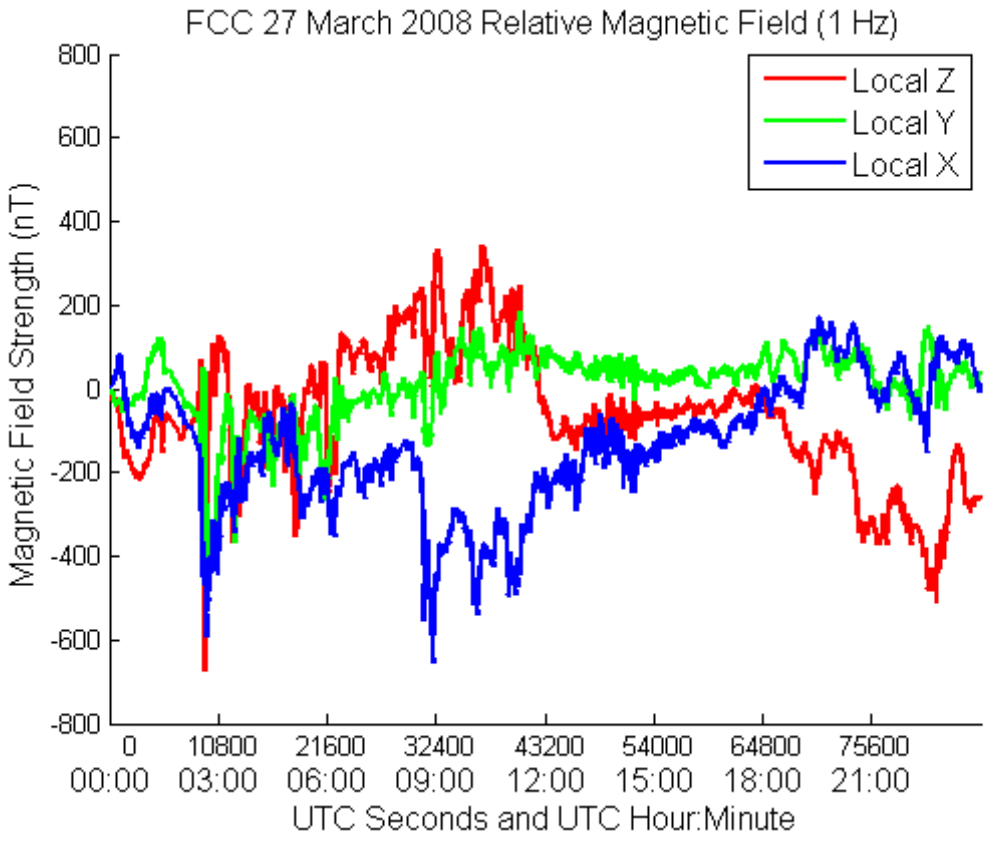

Figure 4-11: March 27th 2008 Event A Churchill MB Magnetic field change versus time (Natural Resources Canada, 2010)

Of note in Figure 4-11 is the sudden negative spike in local magnetic field in the X and Z axes at almost exactly the same time the scintillation activity was observed in the ionosphere. This is the signature of a substorm 'Expansive' or expansion phase, and is caused by the formation of a large East to West current wedge in the ionosphere (Skone 2007). The fact that both the local X and local Z axes show negative deflection indicates that the current wedge is south of the ground station. Another potential recovery event is

present just prior to 9 UTC, but no scintillation data was collected from an L2C enabled satellite at this point in time.

During the event starting shortly after 2:30 UTC, two L2C enabled satellites were in view of the receiving antenna, with the scintillation monitor reporting weak scintillation on only PRN31. While the level of the phase index produced for PRN29 are below what is termed 'very weak', metrics of this observation are also considered. The TEC variations calculated using the dual frequency measurements from these satellites during this event are shown in figures Figure 4-12 and Figure 4-13.

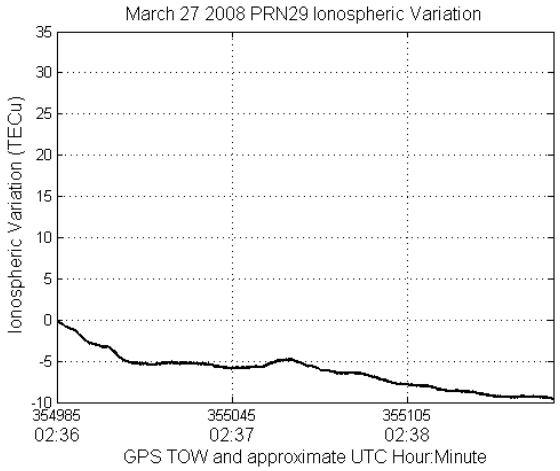

Figure 4-12: Ionospheric change measured via PRN29 observations over auroral Event A.

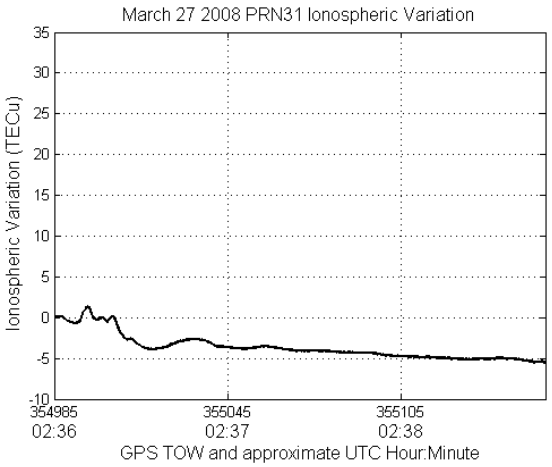

Figure 4-13: Ionospheric change measured via PRN31 observations over auroral Event A.

Since both satellites are in the process of setting it would be expected to see a gradual increase in the level of observed TEC. While this was the case for the reference data set, it is not the case here for either satellite, further indicating abnormal ionospheric conditions. Additionally the rate of change of the ionosphere is approximately 25 times

greater for both PRN29 and PRN31 in this case than it was for PRN31 in the case of the reference data. The scintillation monitor report of no scintillation on PRN29 and weak scintillation on PRN31 is confirmed here, and depicted in Figure 4-14 and Figure 4-15.

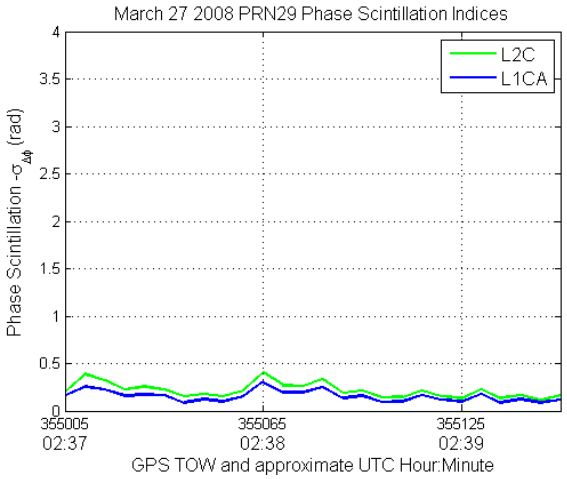

Figure 4-14: Phase scintillation indices over the event measured from PRN29 carriers auroral Event A.

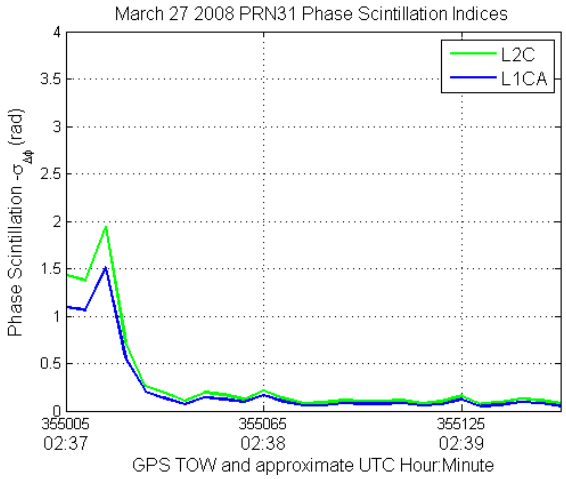

Figure 4-15: Phase scintillation indices over the event measured from PRN31 carriers auroral Event A.

While the 1.5 radian phase scintillation index on the L1 carrier shown for PRN31 in Figure 4-15 appears to exceed the 0.6 radian value that is introduced as demarcating 'strong' phase scintillation by Yu (2007), it is important to recall that the 0.6 radian qualification is based on a one minute averaging interval. In this case, while the phase scintillation is obviously very strong during the initial 18 seconds of data for PRN 31, no subsequent scintillation is observed, resulting in the commercial scintillation monitor reporting the 60 second averaged 'weak' scintillation.

The minor phase scintillation index increase in Figure 4-15 is manifest in the de-trended carrier phase plots for this satellite in Figure 4-17. The relatively constant very low, or

non-scintillation values from Figure 4-14 are also confirmed by the relative stability of the carriers of PRN29 plotted in Figure 4-16. The amplification of the PRN29 phase scintillation indices floor relative to the minimum PRN31 indices is likely attributable to the higher TEC trend rate of the ray path of PRN29 as well as the lower carrier strength expected from the lower elevation PRN29. The TEC irregularities encountered by the L1CA and L2C signals of PRN31 have produced phase scintillation levels that are very strong at six second intervals, but considered weak on both L1 and L2 for a one minute de-trending interval. Interestingly, even though the observed phase scintillation on PRN31 is very strong on short intervals, the relative levels of change on the L1 and L2 carriers appear extremely well correlated over the entire data set.

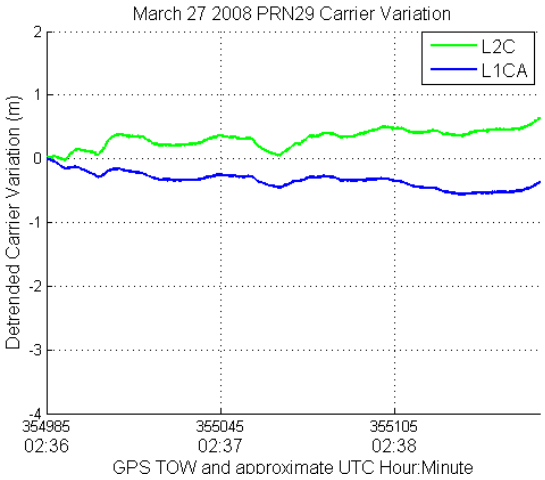

Figure 4-16: PRN29 L1 and L2C carrier variation over auroral Event A.

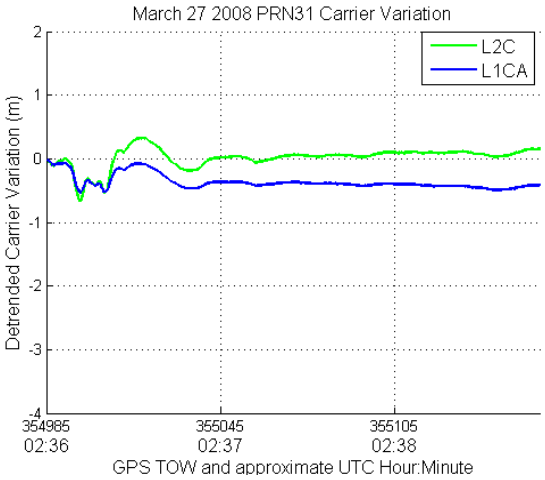

Figure 4-17: PRN31 L1 and L2C carrier variation over auroral Event A.

One can conclude that from Figure 4-17 that the L1 and L2 GPS carriers appear to be encountering the same features within the disturbed ionosphere as they vary in unison without fail. Having established a quiet reference case in addition to a low scintillation

level case, we now proceed to investigate an event in which substantial scintillation is observed, to determine if this near perfect correlation is representative.

4.4 Analysis of Strong Auroral Scintillation Case I – auroral Event B:

Similar to auroral Event A, auroral Event B occurred during space weather conditions conducive to disturbed ionospheric conditions, including elevated solar wind levels leading up to and during the observed scintillation effects, the magnitude of which is plotted in Figure 4-18.

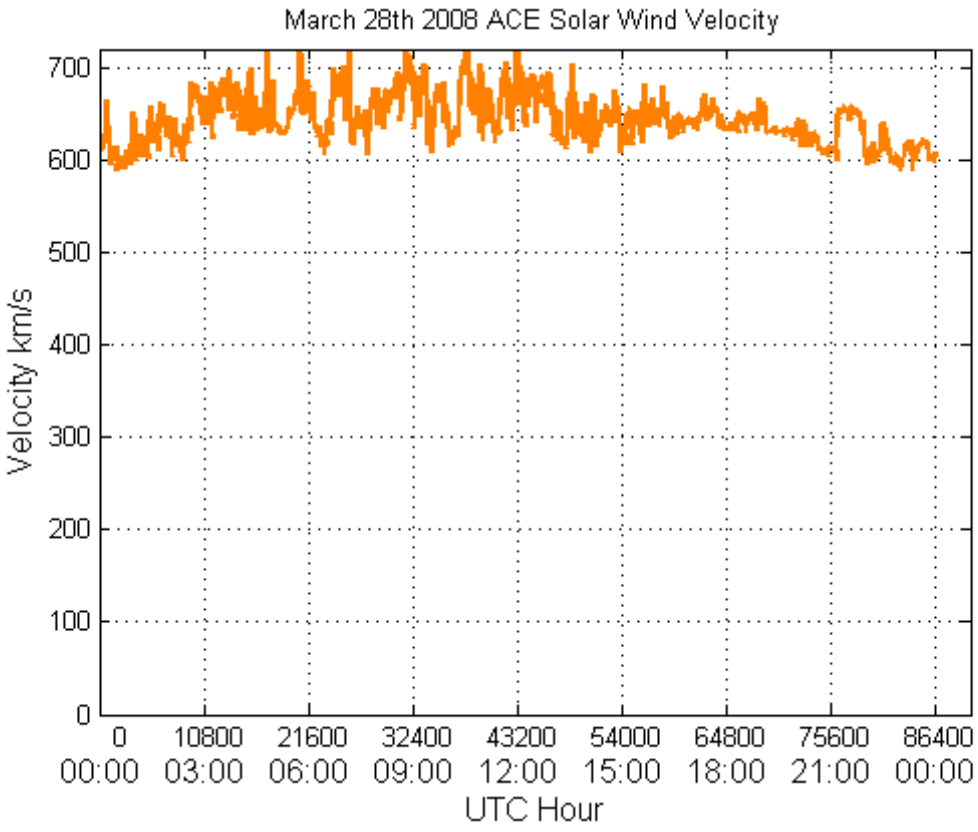

Figure 4-18: March 28th 2008 Solar Wind Velocity towards earth, as reported by the ACE satellite (ASC 2010).

Unlike the previous case which provided the expected case of a negative IMF swinging to a positive value immediately prior to the observation of an ionospheric disturbance by ground based users, the interpolated interplanetary magnetic field did not reach a positive value at any point on this date, as seen in Figure 4-19.

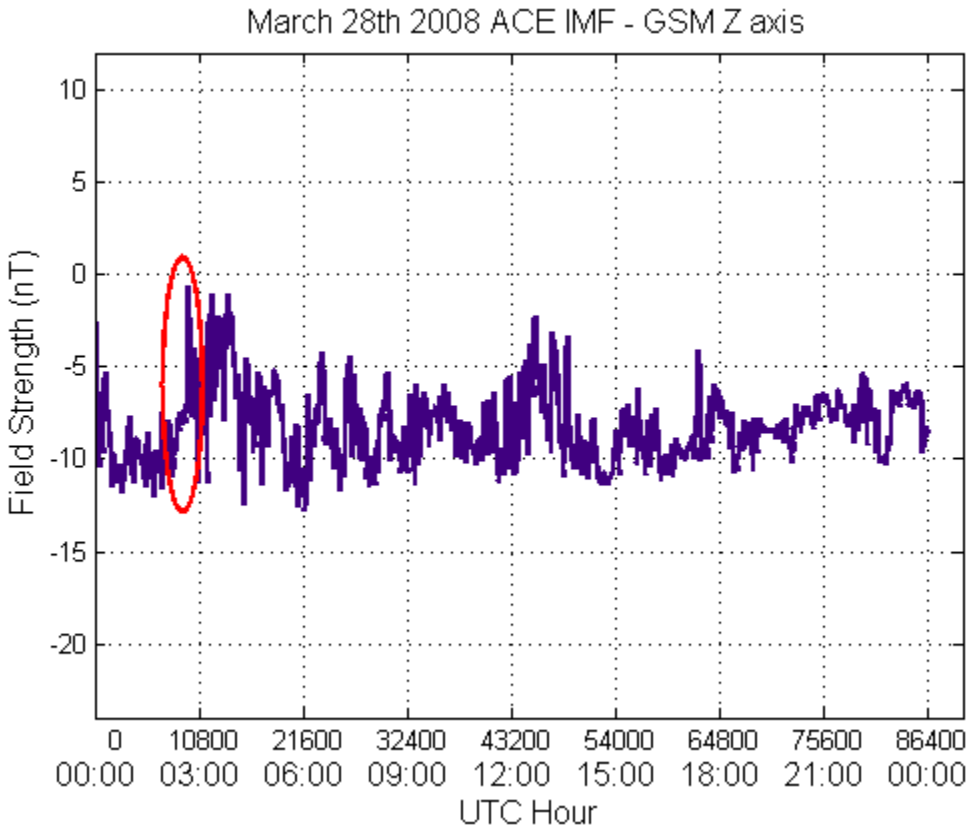

Figure 4-19: March 28th 2008 Interplanetary Magnetic Field, as reported by the ACE satellite (ASC 2010)

While the IMF data presented here does contain the feature of the IMF increasing sharply a short time prior to observing the scintillation described in Event C which is circled in Figure 4-19, it does not turn positive at any point, and no such local increase is seen prior to Event B. The data is however consistent with disturbed ionospheric conditions since

the negative IMF coupled with the elevated solar wind velocity would allow an extended growth phase.

Turning attention to the change vs. time ground based magnetometer measurements near the point of ionospheric observation, shown for this event in Figure 4-20, confirmation of substorm activity is again seen in the form of current wedges manifested as strong local magnetic disturbances. The large negative spike in the X component as well as the Z component at or prior to 1:47 UTC in Figure 4-20 once more indicates the presence of an East West current arc in the ionosphere south of the ground observation point.

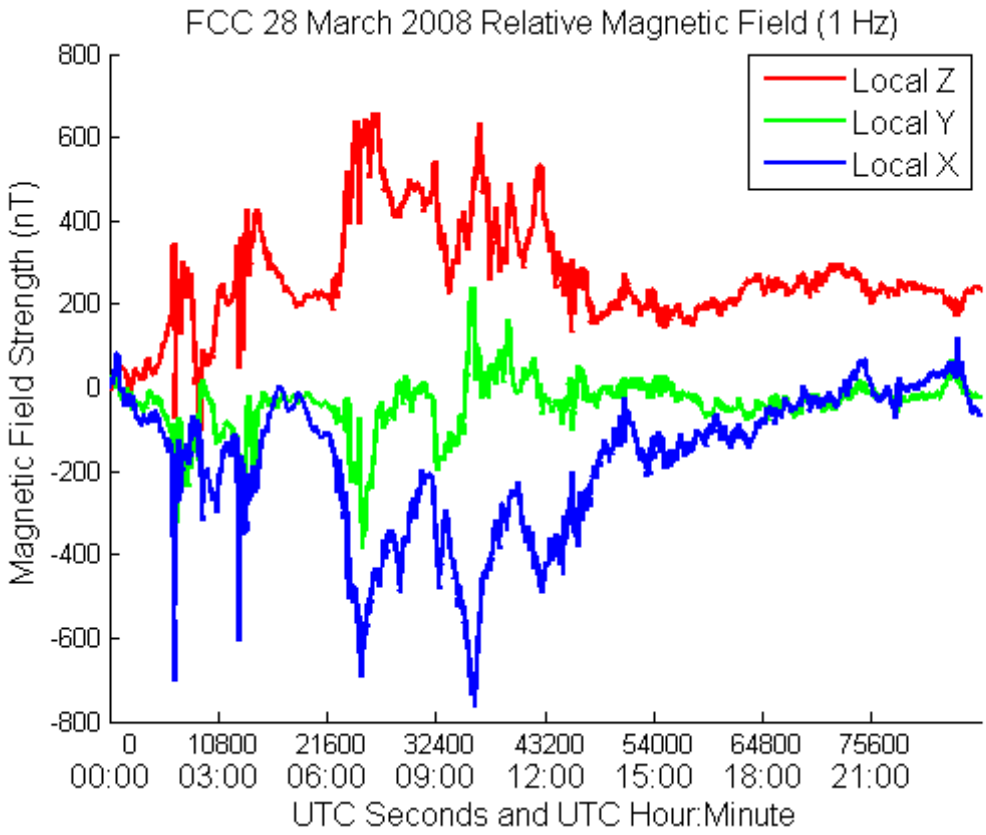

Figure 4-20: March 28th 2008 Churchill MB Magnetic field change versus time (Natural Resources Canada, 2010)

While an additional current wedge signature is prominent between 3:00 and 4:00 UTC, no L2C satellites observed scintillation during this timeframe. However, the event discussed in the next subsection occurred shortly before 3:00 UTC on the 28th of March, and appears correlated with the smaller negative spike seen primarily in the Z direction at this point in time. While the lower extent of the Z trace is partially obscured here, the peak to trough movement in this short interval on the Z axis magnetometer reading is greater than 450 nT.

The ionospheric activity as calculated using the L2C satellites indicated to be affected by ionospheric scintillation by the co-located ISM are shown in Figure 4-21 and Figure 4-22. In these two figures a variation level between 50 and 110 times the absolute TEC variation is observed compared to that observed during the reference July 18th observations.

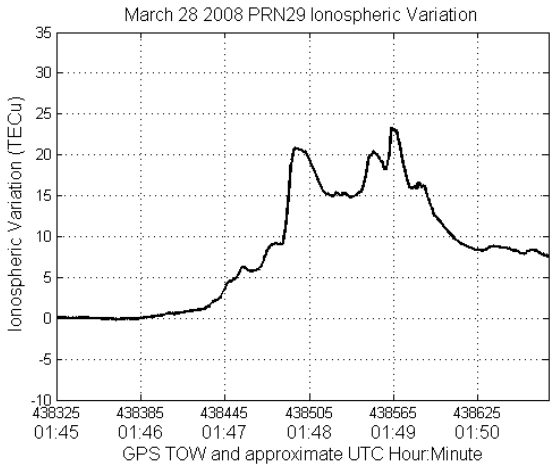

Figure 4-21: Ionospheric change measured via PRN29 observations over auroral Event B.

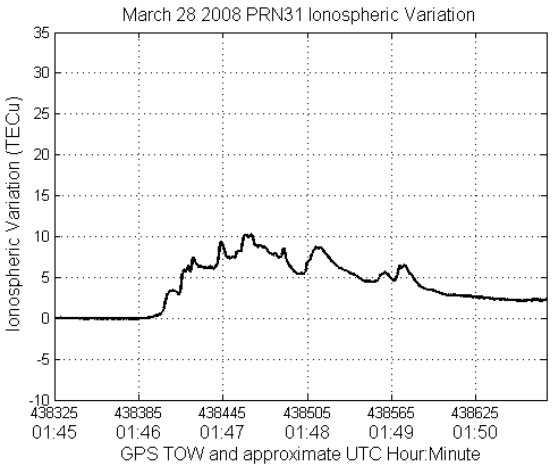

Figure 4-22: Ionospheric change measured via PRN31 observations over auroral Event B.

Confirming that these TEC plots are indeed indicative of disturbed ionosphere, the phase scintillation indices produced independently for L1 and L2 for both PRN 29 and PRN 31 over this event are plotted in Figure 4-23 and Figure 4-24.

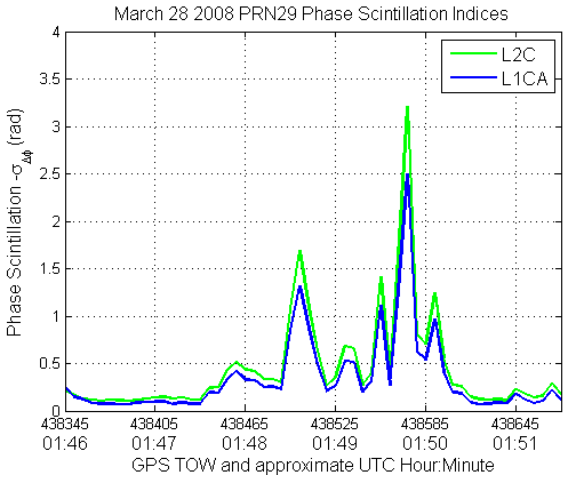

Figure 4-23: Phase scintillation indices over auroral Event B measured from PRN29 carriers.

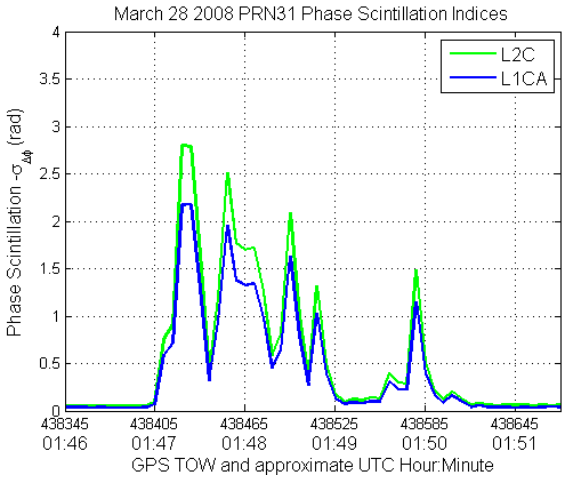

Figure 4-24: Phase scintillation indices over auroral Event B from PRN31 carriers.

Once more, adopting the same classification standards as Yu (2007) the phase effects observed by both satellites are considered to be very strong on both L1, and L2 observed phase scintillation. Despite this, the indices of phase scintillation between L1 and L2 appear to obey the scaling factor posited by Van Dierendonck et al (1993) in so far as

$$\sigma_{\Delta\varphi}(f_{L2}) \cong \sigma_{\Delta\varphi}(f_{L1}) \cdot \frac{f_{L1}}{f_{L2}}, \tag{4.2}$$

where f_{L1} and f_{L2} are the L1 and L2 carrier frequencies respectively.

Since this assertion by Van Dierendonck et al (1993) is based on the assumption that both carriers observe very similar ionospheric disturbances between the satellite and the user, it is once more constructive to view the time variation of the L1 and L2C carriers of each

satellite for qualitative correlation, which are plotted for this event in Figure 4-25 and Figure 4-26.

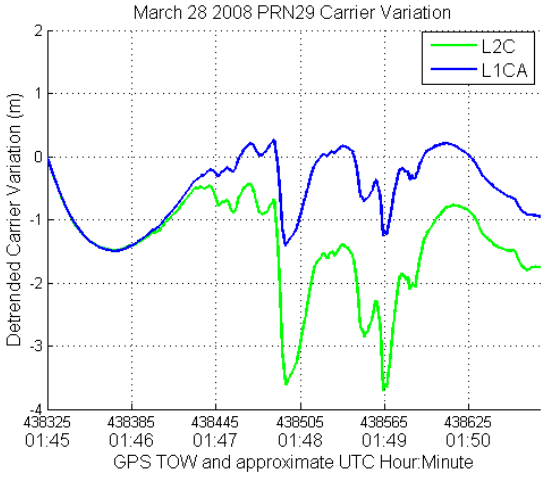

Figure 4-25: PRN29 L1 and L2C carrier variation over auroral Event B.

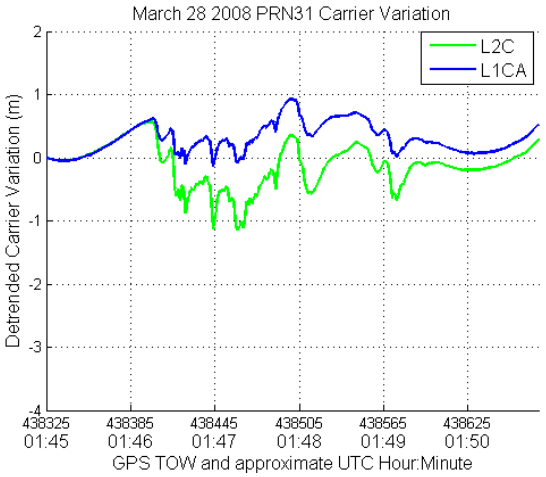

Figure 4-26: PRN31 L1 and L2C carrier variation over auroral Event B.

Here the pattern of nearly identical profiles of carrier variation between L1CA and L2C signals from the same satellite are seen again, for both moderately high elevation and relatively low elevation observations. Also of considerable interest is the fact that even the very small time scale variations captured in the phase series of L1 and L2 carriers from PRN31 seem to indicate excellent correlation even at smaller time, and therefore at smaller physical scale sizes. This correlation shows that equation (4.2) holds for de-trending intervals much shorter than those proposed by the original authors.

Having now considered both weak and strong auroral phase scintillation events which indicate a high level of correlation between the L1 and L2 GPS carriers, it is desirable to confirm the tentative correlation observations through consideration of further instances of strong auroral phase scintillation.

4.5 Analysis of Strong Auroral Scintillation Case II – auroral Event C:

Since Event C occurs later during the same day as Event B, the pertinent solar wind, interplanetary magnetic field, and local magnetic field data have already been introduced in Figure 4-18, Figure 4-19, and Figure 4-20 respectively. For this reason the first new plots in this subsection are those of the observed TEC variation measured once more by PRN 29 and 31 in Figure 4-27 and Figure 4-28.

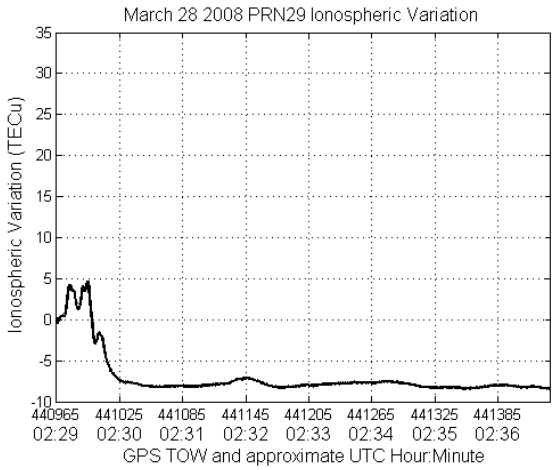

Figure 4-27: Ionospheric change measured via PRN29 observations over auroral Event C.

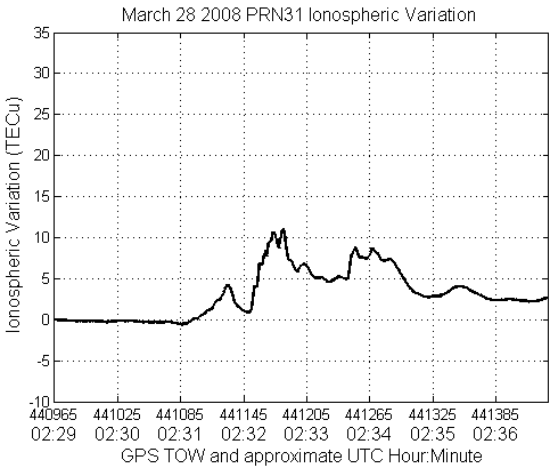

Figure 4-28: Ionospheric change measured via PRN31 observations over auroral Event C.

Although the magnitudes of these TEC variations are smaller than those encountered in Event B, they still represent approximately 25 to 60 times the total variation of TEC over the observation interval when compared to the reference data set. The appearance of rapidly varying, small magnitude changes in TEC content are confirmed once more by the phase scintillation indices in Figure 4-29 and Figure 4-30, which demonstrate that

despite the lower absolute TEC range traversed during this event relative to Event B, the rate and nature of the variation is sufficient to once more generate what could be considered very strong phase scintillation on both carriers of PRN31, as well as both carriers of PRN29 over a shorter duration.

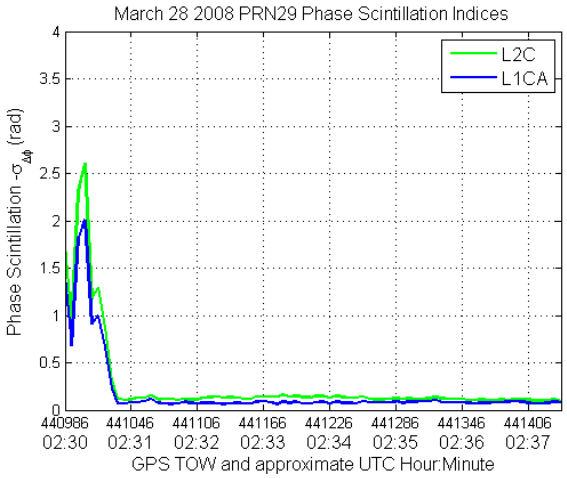

Figure 4-29: Phase scintillation indices over auroral Event C measured from PRN29 carriers.

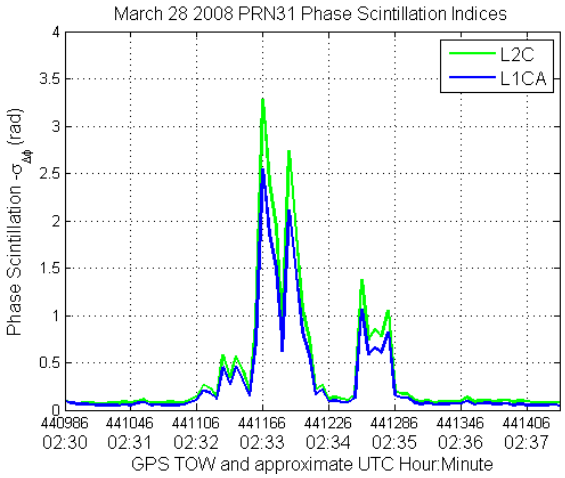

Figure 4-30: Phase scintillation indices over auroral Event C measured from PRN31 carriers.

The relative variation of the phase scintillation indices determined using the L1 and L2C carriers of each satellite once again appear to obey the scaling projection that was asserted by Van Dierendonck et al (1993), while the de-trended carrier plots in Figure 4-31 and Figure 4-32 once more seem to indicate a very high level of correlation between the features encountered by the L1 and L2 carriers of a GPS satellite. For both PRN's the de-trended carriers show what appears to be perfect agreement in their variation over the entire period of scintillation.

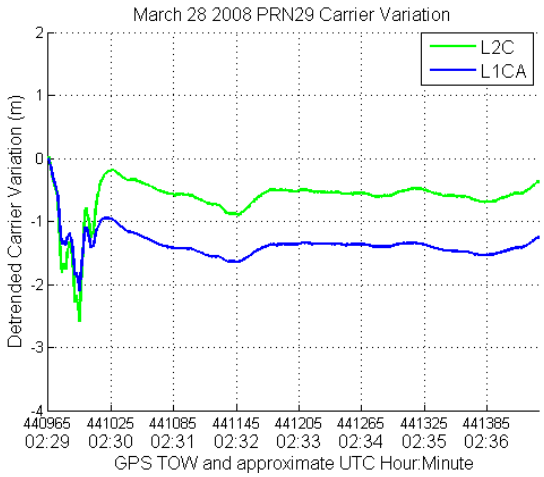

Figure 4-31: L1 and L2C carrier variation on PRN29 over auroral Event C.

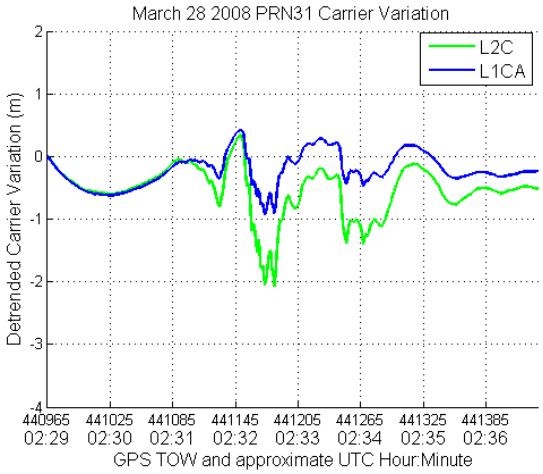

Figure 4-32: L1 and L2C carrier variation on PRN31 over auroral Event C.

While investigation of the small undulations observable in the de-trended carriers led to further observation of interesting disturbed ionospheric phenomena known as 'pulsations' (Lipko et al 2001, Menk et al 2003), said observations are not directly related to the current line of inquiry and are therefore relegated to a later sub-section. The immediate question of the relationship between the variability of the ionosphere as it relates to the correlation between the L1 and L2 carriers and of the scale sizes of the disturbances causing the correlated changes is pursued first.

4.6 Determination of Auroral Anomaly Sizes Inducing Correlated Carrier Activity

In order to characterize the approximate sizes of the ionospheric irregularities which were responsible for causing the identified scintillation to manifest, it is necessary to first complete two related sub-tasks. The first of these is the calculation of the ray path

velocity through the region of the ionosphere believed to contain the anomalies. The latter is the determination of the spectral content of the correlated ionospheric activity between the L1 and L2 carriers. The second task requires the first, since the spectrum of the observations must be related to the physical displacement rate of the ray path between the satellite and user, which will vary between each satellite in view.

The approach taken to approximating the ray path sweep rate through the disturbed ionosphere is to use the known receiver antenna coordinates along with the reported azimuth and elevation angles between the user and each satellite affected by scintillation. Together the position of the receiving antenna along with the azimuth and elevation angle to the satellite can be used to determine the latitude and longitude where the ray path intersects a specified altitude of the ionosphere. This point of intersection is referred to as the Ionospheric Pierce Point (IPP). Using the distance between the ionospheric pierce points at the start and conclusion of the scintillation events, as well as the data set length, the velocity of the ray path through the ionosphere can be approximated.

Proceeding according to the method of IPP determination presented in Gaussiran et al (2004), one first calculates the earth central angle Ψ as

$$\Psi = \frac{\pi}{2} - El \cdot \sin^{-1}\left(\frac{R_e \cos(El)}{R_e + h_I}\right) \tag{4.3}$$

where *El* is the user to satellite elevation angle, R_e is the radius of the earth, and h_I is the height above ground at which the pierce point is to be calculated. Fixing the parameter of the earth Radius as 6378136 metres, the ionospheric height of interest of 350 km is assumed due to the association of F-layer irregularities with substorm events (Skone 2007).

The latitude of the IPP, φ_{pp} and longitude of the IPP, λ_{pp} are calculated as

$$\varphi_{pp} = \sin^{-1}(\sin(\varphi_u)\cdot\cos(\Psi) + \cos(\varphi_u)\cdot\sin(\Psi)\cdot\cos(Az)) \tag{4.4}$$

$$\lambda_{pp} = \lambda_u + \sin^{-1}((\sin(\Psi)\cdot\sin(Az))/\cos(\varphi_u)) \tag{4.5}$$

where φ_u is the user latitude, and λ_{pp} is the user longitude, and *Az* is the user satellite azimuth angle.

The average position of the user antenna over the course of the Churchill auroral scintillation data sets was approximately 58.7377^o North Latitude and 98.8193^o West Longitude. The tabulated start and finish azimuth and elevation angles of the satellites encountering ionospheric scintillation for each auroral event are presented in Table 4-1.

Table 4-1: Azimuth and Elevation changes for IIR-M GPS satellites tracked during auroral scintillation

Auroral Event and PRN	Initial Azimuth and Elevation	Final Azimuth and Elevation
Event A, PRN29	45.2^o Az, 21.6^o El	44.3^o Az, 21.5^o El
Event A, PRN31	81.7^o Az, 35.7^o El	82.0^o Az, 34.9^o El
Event B, PRN29	65.4^o Az, 17.8^o El	63.2^o Az, 18.7^o El
Event B, PRN31	80.1^o Az, 56.3^o El	79.7^o Az, 53.9^o El
Event C, PRN29	46.3^o Az, 21.6^o El	43.4^o Az, 21.4^o El
Event C, PRN31	81.4^o Az, 36.8^o El	82.2^o Az, 34.0^o El

By applying equations (4.3), (4.4) and (4.5) to the user position and each azimuth and elevation pair, the latitude and longitude at the ionospheric pierce points at the start and end of the observations are calculated as shown Table 4-2. Additionally the changes in pierce point latitude and longitude are calculated for each event and each satellite.

Table 4-2: Ionospheric pierce points of satellite to user ray path of IIR-M GPS satellites tracked during auroral scintillation, assuming a 350 km ionosphere altitude.

Auroral Event and PRN	Initial Pierce Point (Lat., Lon.)	Final Pierce Point (Lat., Lon.)	Change on Interval (Lat., Lon.)
Event A, PRN29	63.0126^o,-84.7952^o	63.1115^o,-84.9028^o	0.0989^o,-0.1076^o
Event A, PRN31	59.0854^o,-86.2514^o	59.0672^o,-86.0377^o	-0.0182^o,0.2137^o
Event B, PRN29	61.1677^o,-80.2457^o	61.3832^o,-80.9999^o	0.2155^o,-0.7542^o
Event B, PRN31	59.0212^o,-90.0860^o	59.0565^o,-89.7507^o	0.0353^o,0.3353^o
Event C, PRN29	62.9094^o,-84.6234^o	63.2101^o,-85.0135^o	0.3007^o,-0.3901^o
Event C, PRN31	59.1006^o, -86.5324^o	59.0551^o,-85.7915^o	-0.0455^o,0.7409^o

Since the duration of observations is relatively short, the velocities of the ray paths are treated as constant values. The arc lengths traversed by the IPPs, the durations of observation and the calculated sweep rates of the auroral events are tabulated in Table 4-3.

Table 4-3: Arcs of travel, event durations, and resulting sweep rates for satellite to user ray paths during auroral scintillation events

Auroral Event and PRN	Arc Lengths (metres)	Event Duration (seconds)	Sweep rate through shell (m/s)
Event A, PRN29	12260	180	68
Event A, PRN31	12380	180	69
Event B, PRN29	46890	360	130
Event B, PRN31	19580	360	54
Event C, PRN29	38790	480	81
Event C, PRN31	42430	480	88

This calculation of sweep rate does however carry the caveat that the ionospheric drift rate parallel to the direction of ray path travel is not known and not accounted for here. However, equipped with the approximated ray path sweep rates for the carrier signals that encountered scintillation causing anomalies, and with the desire to determine the physical scale size of anomalies which are simultaneously observable across both L1 and L2C measurements, one can now turn to quantitatively defining the level of agreement between the carriers.

4.7 Determining TEC change weighted carrier correlation

Since the metric of agreement between the L1 and L2 carriers must convey both the certainty that the observation indicates a relevant ionospheric change, in addition to the determination as to whether the change is confirmed or contradicted by the variation in each carrier independently, calculation is subdivided along these lines.

To provide a confidence, or weighting value for each sample of data, the probability that the measured TEC variation across each epoch is simply the contribution of noise is

calculated. This can be approached by observing that the distribution of epoch to epoch change in the measured TEC is Gaussian for both the calm and disturbed ionospheric conditions presented. Since this is the case, the weighting vector *W(n)* is set as

$$W(n) = 1 - Q\left[\frac{abs(\Delta dTEC(n))}{NP_{\Delta dTEC}}\right] \tag{4.6}$$

where *Q* is the right tail Gaussian probability, $\Delta dTEC(n)$ is the epoch to epoch change in the measured TEC value, and $NP_{\Delta dTEC}$ is the estimate noise power of the TEC change series. In this way, low levels of ionospheric variation will produce weighting values in the vicinity of 0.5, while TEC levels that vary rapidly with respect to the level of noise in the TEC observations will produce weightings approaching 1.

The question of estimating the value of and $NP_{\Delta dTEC}$ in a way that is not influenced by the presence of scintillation is important, as an error in the determination of this value would skew the weighting vector to either exaggerate or diminish the estimate of the level of ionospheric activity present. To produce an estimate largely free of ionospheric influence, it was decided to assume a flat noise spectrum and to form the estimate using only the high frequency range of the $\Delta dTEC$ measurements, believed to be above the frequency of interest for scintillation observation. To facilitate this, the GSNRx™ software receiver was configured to provide 100 Hz observations, with a carrier tracking loop noise bandwidth of 50 Hz. To maintain stability at this high bandwidth it was necessary to restrict coherent integration time as discussed by Kazemi (2010), resulting in

the selection of 1 ms coherent integration periods. The selected region of spectral density used to estimate the noise density in the $\Delta dTEC$ observations was between 40 and 50 Hz since it is assumed that this frequency band will experience the lowest influence of ionospheric scintillation effects.

Applying this method to the reference July 18th 2008 data produces the expected nearly constant weighting near 0.5, as the epoch to epoch ionospheric variations are not significant relative to the measured level of carrier noise. The application of this method to one of the scintillation scenarios however correctly produces higher values during higher periods of ionospheric activity. These *W(n)* weighting vectors are shown in Figure 4-33 and Figure 4-34 for the duration of the data sets stated in the title of each.

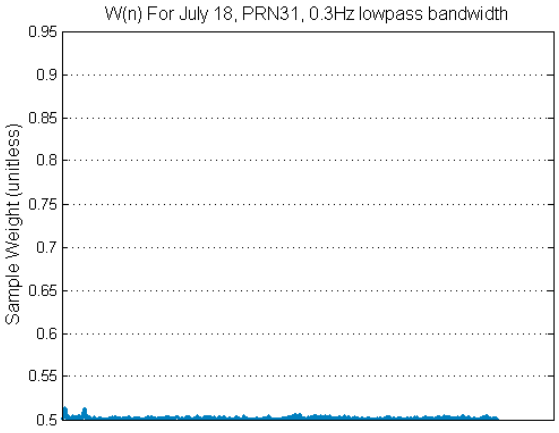

Figure 4-33: Weighting vector for July 18 reference data, 0.3 Hz lowpass bandwidth.

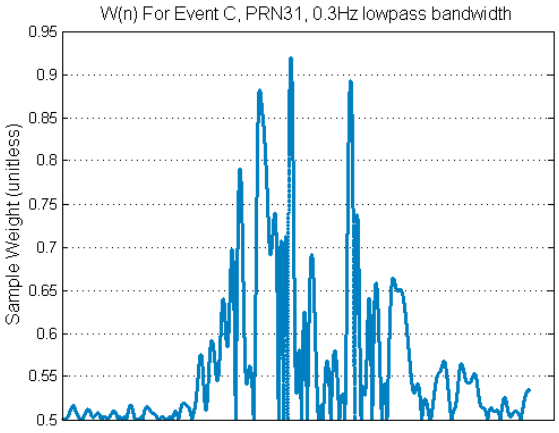

Figure 4-34: Weighting vector for auroral Event C observed on PRN 31.

Having selected the method of weighting of the observations, the determination as to whether the change is confirmed or contradicted by the variation in each carrier is calculated in a concise manner. Specifically, the decision is based on whether the signs

of the epoch to epoch changes in each of the L1 and L2 GPS carriers match. Since this measure of agreement would be nearly total for even a stationary receiver due to satellite motion, it is required that the carriers first be de-trended such that phase changes due to relative satellite motion are not considered. Using the same de-trended phase observations as were plotted earlier for every data set considered, this determination is then

$$D(n) = sign(\Delta\phi_{Det.L1}(n)) \cdot sign(\Delta\phi_{Det.L2}(n)) . \quad (4.7)$$

The term $\Delta\phi_{Det.L1}$ represents the vector of epoch to epoch changes in the de-trended L1 carrier phase vector, while $\Delta\phi_{Det.L2}$ is the analog of the same for the L2 carrier.

This phase change sign product will have a high likelihood of taking on a value of +1 during periods of correlated carrier change due to outside influences, but will take on values of -1 due either to noise or to a lack of agreement between the sign of the change in the de-trended phase observations. This sign agreement for the July 18 reference case and event C are plotted in Figure 4-35 and Figure 4-36.

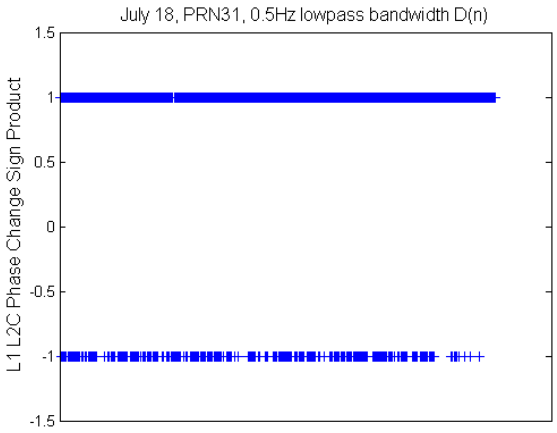

Figure 4-35: Determination vector for July 18 reference data, 0.5 Hz lowpass bandwidth.

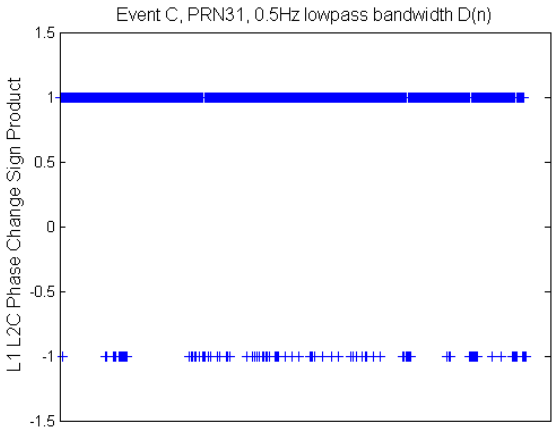

Figure 4-36: Determination vector for Event C observed on PRN31.

As expected, the sign products produced for the reference case possess a large population of negative values, resulting in a mean agreement rate of 0.52 for the July 18th *D(n)* vector. In the reference case the population is not evenly distributed due to the underlying trend in the ionosphere plus correlated tropospheric variation causing carrier change sign agreement more frequently than the 50% that would occur in the case of pure noise. By comparing the reference case with the Event C example shown beside, it is clear that the increased level of correlated ionospheric variation due to scintillation has increased the probability that the changes in each carrier will be of the same sign, resulting in a mean weighting of 0.87 for the Event C *D(n)* vector.

The reference determination vector could be moved closer to an average value of zero by pre-filtering the carriers with a high pass filter similar to that used when calculating the phase scintillation indices. This was not done here however as it was desired to retain the low frequency contributions for the time being. Likewise the scintillation event

determination vector could be increased in average value by omitting the initial and/or final quiet portions of the data set, however for the sake of simplicity this was not done here.

The TEC variation weighted carrier agreement *'T'* is finally calculated over the length of the set of data using the results of equations (4.6) and (4.7) as

$$T = \sum_{1}^{n} \left[D(n) \cdot W(n) \right]. \tag{4.8}$$

The sum *T* ideally scales only due to increased correlated carrier variation, or with decreased observation noise, however due to the slow yet correlated changes in background TEC during calm days, as well as changing tropospheric delay or satellite/system oscillator effects, the value of *T* will increase in value with longer length data sets. Despite this, the magnitude of *T* divided by the length of the observation set remains much lower for the reference set than that calculated for the data sets which contain scintillation. As such the preferable metric is the scaled *T* value, *Ts*, which takes the number of observations '*n*' into account as

$$Ts = \frac{1}{n} \sum_{1}^{n} \left[D(n) \cdot W(n) \right]. \tag{4.9}$$

Since the desired application of *Ts* is the determination of the ionospheric anomaly scale sizes that are most responsible for the correlated scintillation activity, it is now necessary to relate *Ts* to the spectral content of ionospheric effects that are correlated between the L1 and L2 GPS carriers. As the sweep rate of the satellite to user ray path for each data set is known, it is possible to equate a given bandwidth of carrier observation via the *Ts*

index to a physical displacement perpendicular to the ray path in the region containing the ionospheric irregularities responsible for scintillation.

To allow this, the evaluation of the *Ts* value is produced using low pass filtered versions of the de-trended L1 and L2 carriers and by incrementally increasing low pass filter bandwidths between 0.1 and 10 Hz. An increase in the level of correlation between the ionospheric effects on the L1 and L2 carriers is seen as an increase in the *Ts* index from one filtering level to the next. This increase indicates that the incremental bandwidth contained more correlated information power than noise. The low-pass filtered versions of the de-trended carrier change series are produced by passing the polynomial de-trended carriers through a 6^{th} order low-pass Butterworth filter implemented in the same fashion as that used when calculating the phase scintillation indices but with a variable bandwidth. The low-pass filtered TEC is then computed per equation (4.1) before the epoch to epoch difference series of each of the filtered carrier series and TEC are formed.

Once more under the assumption of spectrally flat noise, the noise power in the filtered delta TEC series is calculated as the low pass bandwidth multiplied by the noise density in the 40-50 Hz region of the unfiltered TEC changes. This produces the low-pass filtered weighting vector as

$$W^{LPF}(n) = 1 - Q\left[\frac{abs(\Delta dTEC^{LPF}(n))}{NP_{\Delta dTEC}^{LPF}}\right]. \qquad (4.10)$$

Similarly the phase change sign product is recalculated using the low pass filtered data to produce

$$D^{LPF}(n) = sign(\Delta\phi^{LPF}_{Det.L1}(n)) \cdot sign(\Delta\phi^{LPF}_{Det.L2}(n)) \tag{4.11}$$

which together with the product of equation (4.9) is used to form the expression for the low pass filtered, scaled, TEC variation weighted carrier agreement

$$Ts^{LPF} = \frac{1}{n}\sum_{1}^{n}\left[D^{LPF}(n) \cdot W^{LPF}(n)\right]. \tag{4.12}$$

From the understanding that the majority of systemic effects visible on and correlated between the L1 and L2 carriers should have power spectra below 0.1 Hz (Olynik et al 2001), the proportional increase in noise with each incremental increase in filter bandwidth beyond 0.1 Hz should result in a decrease in the apparent level of correlation. This is the result of the addition of uncorrelated noise without an expected commensurate addition of correlated carrier change in the added frequency band. If, however, an increase is seen with added bandwidth, this indicates that the level of correlated power between the L1 and L2 carriers in the newly added band of observation exceeds that of the noise increase due to the addition of the extra bandwidth. It must be understood that a decline in the value of Ts^{LPF} does not necessarily indicate a lack of correlated information in the incremental bandwidth. The other interpretation of this decline is the case where the noise power increases by a greater degree than correlated carrier activity.

Since the value of Ts^{LPF} for a given cutoff frequency is dependent on the level of correlated carrier activity, the raw value produced for any data set containing scintillation is far higher than that present in the reference data set. To allow better focus on the relative spectral content of the different data sets, the Ts^{LPF} vectors from 0.1 to 10 Hz are normalized to the 0.1 Hz Ts^{LPF} value of the given data set to produce a constant value of

1 at 0.1 Hz of lowpass cutoff for any data set. For the reference data set, this normalized Ts^{LPF} is plotted as the green trace in Figure 4-37 for low pass frequencies between 0.1 and 10 Hz. Also plotted in this figure in red is the projected behaviour of Ts^{LPF} under the assumptions that the noise in the band of interest is spectrally flat and that the carriers posses no correlated variation above 0.1 Hz of bandwidth. Taking the difference between the actual value of Ts^{LPF} and the projected trend for the July 18 reference data set yields the difference plotted in Figure 4-38. It can be inferred from this plot that the carriers do pose a correlated variation slightly in excess of noise for frequencies up to 0.3 Hz, where the ratio of correlated carrier activity to noise reaches maximum.

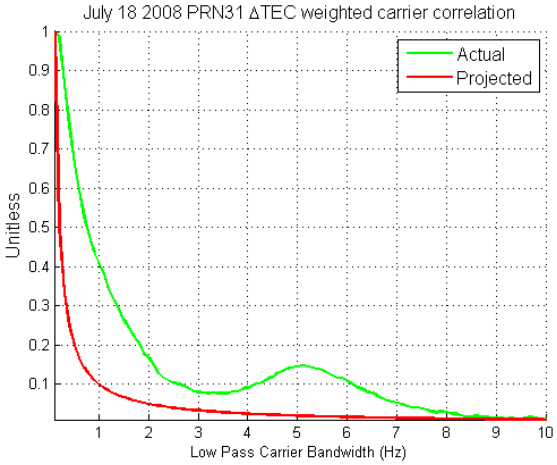

Figure 4-37: Actual and projected delta TEC weighted carrier correlation, July 18 reference data.

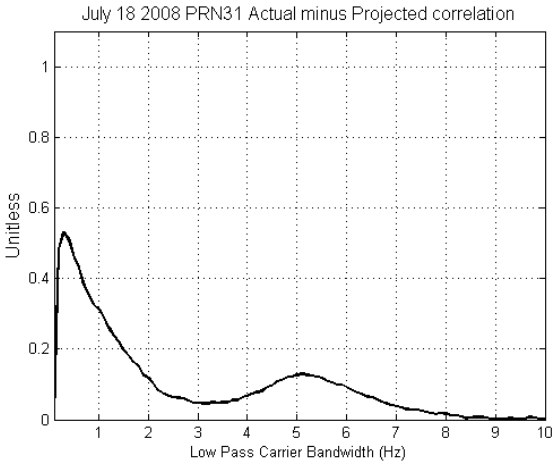

Figure 4-38: Difference between actual and projected delta TEC weighted carrier correlation, July 18 reference data.

Of potential interest is the local maximum peak in Figure 4-37 at 5.1 Hz. Since this peak appears in both the reference data as well as some but not all auroral scintillation data sets, it is not believed to be an ionospheric contribution. Additionally since this feature

appears on both PRN29 and PRN31 it is thought to be a product of either the Block IIR-M satellites, or the noise floor of the RF front end used to collect the IF samples.

Applying the same methods of analysis to the data sets containing scintillation provides insight into the frequency and by extension via the calculated ray path sweep rate, the physical scale sizes responsible for the majority of correlated scintillation activity. Starting with Event A, the TEC change weighted carrier correlation and the projected value of the same for PRN29 are plotted in Figure 4-39 while the difference is plotted in Figure 4-40. Though PRN29 was not subjected to levels of variation associated with scintillation during Event A, the background ionosphere was still highly variable compared to that seen in the reference case. This disturbed ionosphere is still of some interest and was therefore analyzed in addition to the scintillating PRN31.

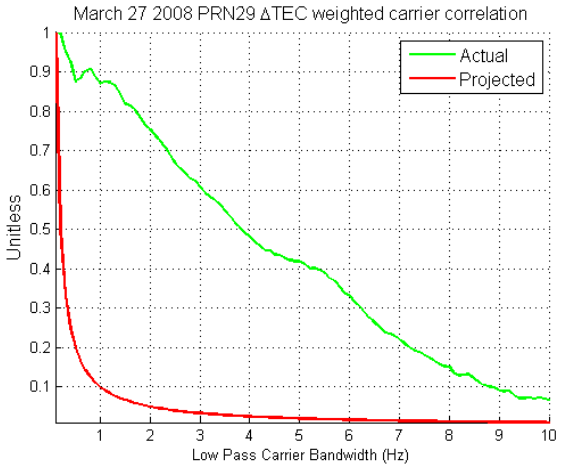

Figure 4-39: Actual and projected delta TEC weighted carrier correlation, auroral Event A PRN29.

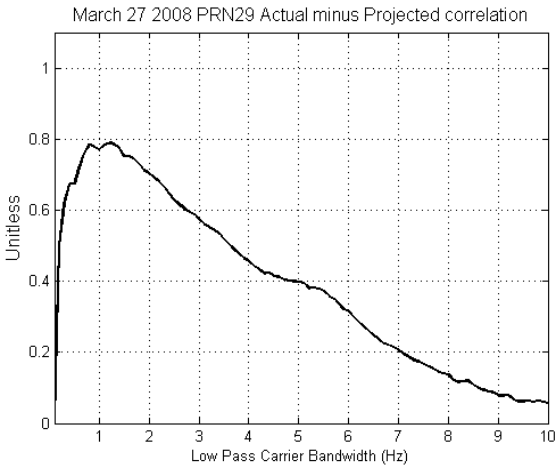

Figure 4-40: Difference between actual and projected delta TEC weighted carrier correlation, auroral Event A PRN29.

The same plots, produced for PRN 31 are shown in Figure 4-41 and Figure 4-42 respectively.

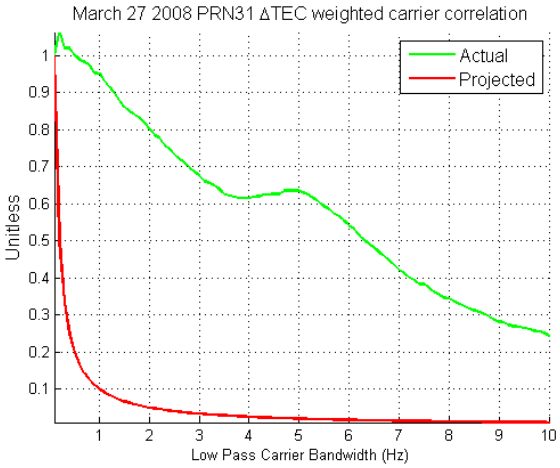

Figure 4-41: Actual and projected delta TEC weighted carrier correlation, auroral Event A PRN31.

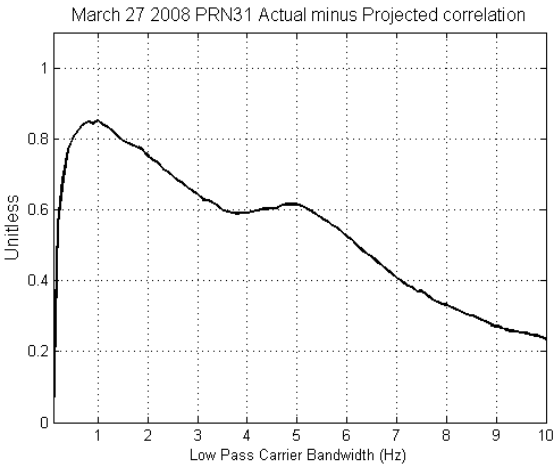

Figure 4-42: Difference between actual and projected delta TEC weighted carrier correlation, auroral Event A PRN31.

When compared to the reference data set, the subdued phase scintillation present on PRN31 during Event A, and even the disturbed but not scintillating ionosphere observed by PRN29 has noticeably pushed the maximum correlated power point by a factor of 3-4 times. The frequency of maximum correlated carrier activity relative to noise is now 1 Hz for PRN31, and 1.2 Hz for PRN29. Recalling that these can be related to physical anomaly sizes using the previously calculated sweep rates, Ts^{LPF} data will be presented for the other auroral data sets without further comment. Identical plots as those produced for auroral Event A in Figure 4-41and Figure 4-42 are presented for auroral Event B in Figure 4-43 through Figure 4-46 while those produced for auroral Event C are found in Figure 4-47 through Figure 4-50.

Auroral Event B Delta TEC weighted Carrier Correlation

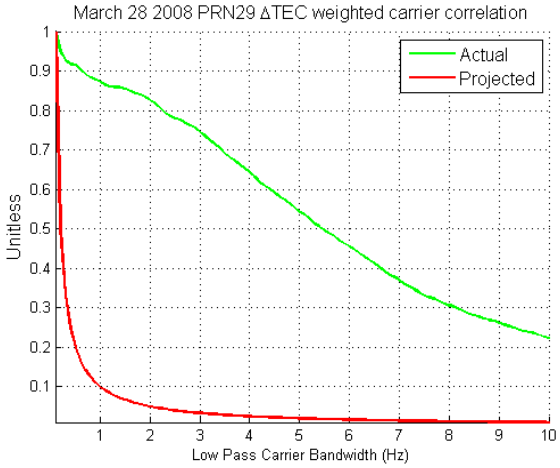

Figure 4-43: Actual and projected delta TEC weighted carrier correlation, auroral Event B PRN29.

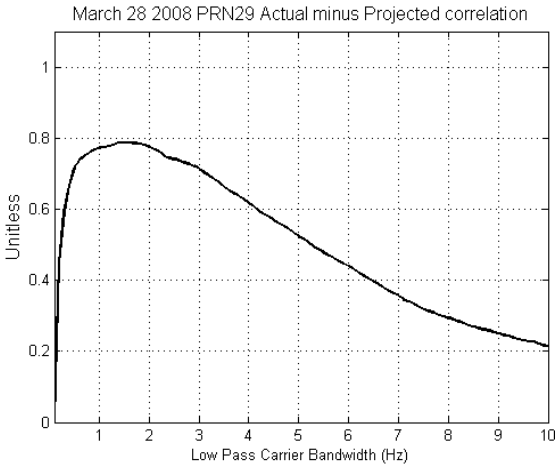

Figure 4-44: Difference between actual and projected delta TEC weighted carrier correlation, auroral Event B PRN29.

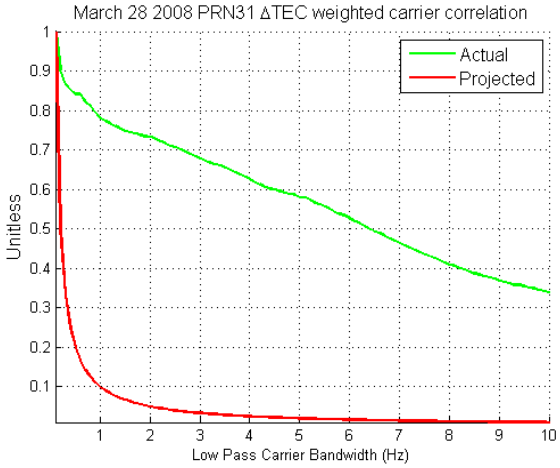

Figure 4-45: Actual and projected delta TEC weighted carrier correlation, auroral Event B PRN31.

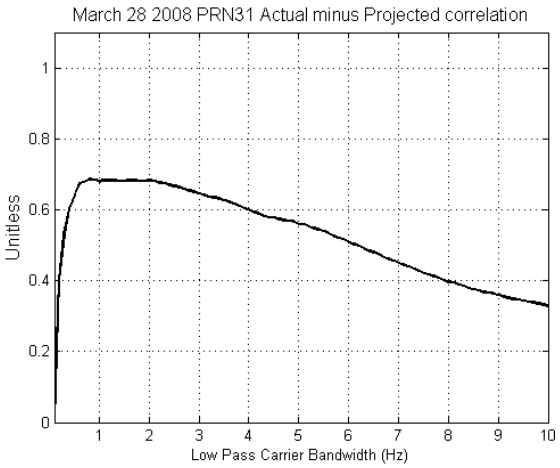

Figure 4-46: Difference between actual and projected delta TEC weighted carrier correlation, auroral Event B PRN31.

Auroral Event C Delta TEC weighted Carrier Correlation

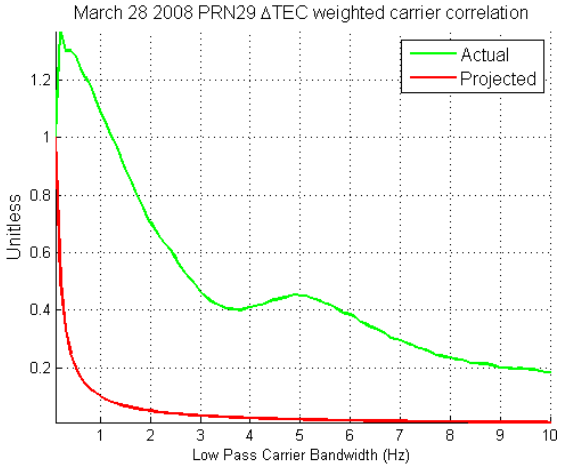

Figure 4-47: Actual and projected delta TEC weighted carrier correlation, auroral Event C PRN29.

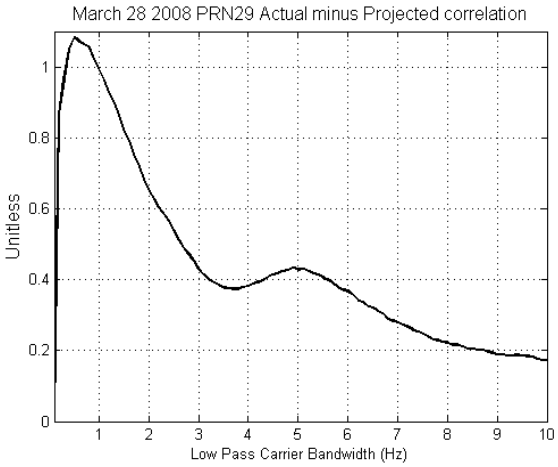

Figure 4-48: Difference between actual and projected delta TEC weighted carrier correlation, auroral Event C PRN29.

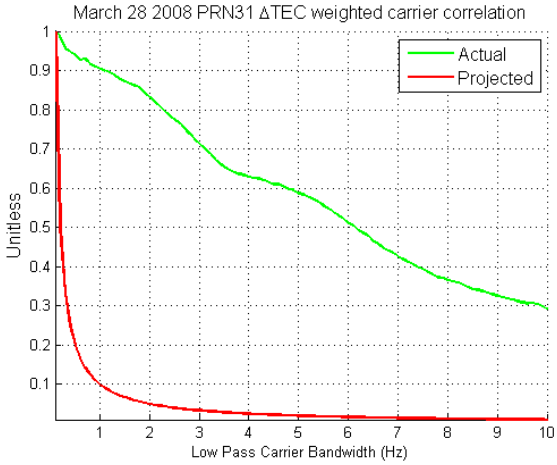

Figure 4-49: Actual and projected delta TEC weighted carrier correlation, auroral Event C PRN31.

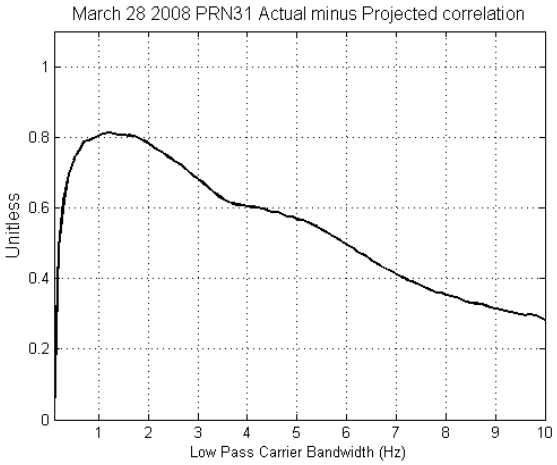

Figure 4-50: Difference between actual and projected delta TEC weighted carrier correlation, auroral Event C PRN31.

Tabulating the frequencies of peak TEC weighted correlated carrier change, and dividing the sweep rates determined earlier by these frequency values in Table 4-4, the anomaly sizes producing the maximum level of correlated activity are determined.

Table 4-4: Frequencies of maximum TEC weighted carrier correlation converted to encountered auroral ionospheric anomaly sizes.

Auroral Event/PRN	Freq. of Maximum Correlated Carrier Variation vs. Noise	Sweep Rate in metres/second (See Table 4-3).	Associated Anomaly Size (metres)
Event A PRN29	1.3-1.4 Hz	68	49 – 52
Event A PRN31	1 Hz	69	69
Event B PRN29	1.7 Hz	130	76
Event B PRN31	1.1-2.1 Hz	54	26 – 49
Event C PRN29	0.6 Hz	81	135
Event C PRN31	1.2 Hz	88	73

If this data is representative, the average physical ionospheric anomaly size which produces the maximum observable correlated carrier change between L1 and L2 GPS signals is 74 metres. This agrees with the lower range of expected sizes of ionospheric irregularities expected to be present during scintillation events.

However, as previously mentioned this is likely not the limit of information that can be gained about the disturbed ionosphere during scintillation using the GNSS carriers. In Table 4-4 the anomaly size calculated is the one which produces the highest level of correlated carrier information relative to noise in the measurement bandwidth, not the anomaly size associated with de-correlation of the L1 and L2C carriers. To calculate this latter feature size, it would be necessary to determine the frequency at which the incremental bandwidth produces a decline in correlated carrier activity larger than can be explained by the addition of the noise power in the added bandwidth.

Due to the apparently lower noise density near 5 Hz in many of the data sets, it is not currently possible to determine this de-correlation frequency with certainty. However, early attempts to do so suggest that in all of the auroral scintillation cases discussed, this de-correlation point occurs above 10 Hz, and may reach as high as 37.5 Hz in some cases. It is therefore likely the case that the limit of correlated ionospheric information between the L1 and L2 GPS carriers occurs at scale sizes smaller than those presented in Table 4-4, by a factor between five and fifteen for the auroral events considered.

Since the data from which the 'optimally detectable' anomaly size of 74 metres is thus far based entirely on auroral zone scintillation events, it is desirable to repeat the analysis for disturbed ionospheric conditions in the polar region.

4.8 Polar Scintillation Analysis

Since the physical processes causing disturbed ionospheric conditions are not the same in the Polar region, it stands to reason that there may be quantitative differences in the level or frequency range of correlated ionospheric activity between the L1 and L2 GPS carriers. Unlike the Churchill northern studies centre, the Eureka Nunavut polar collection site is at 80^{o} North latitude, located above the auroral oval.

Due to the location of Eureka above the auroral oval, visible aurora displays are not common and do not serve as a good proxy indicator of scintillation. For this reason, the

forecasting and now-casting facilities of SpaceWeather.com were employed to predict when best to collect IF samples in conjunction with co-located scintillation monitor outputs. On October 11 2008 the observation of a Coronal Mass Ejection (CME) was announced by SpaceWeather.com (2008), along with the prediction that this ejection could begin interacting with Earth on October 11th.

Due to the potential for scintillation as a consequence of this CME, data was logged for nearly 22 consecutive hours during the October 11-12 period. While it is confirmed that a geomagnetic storm resulted from the interaction of this CME with Earth on October 12th 2008 per SpaceWeather.com (2008a), only sporadic and low magnitude phase scintillation events were observed.

4.9 Reference Calm Data Re-Plotted For Polar Data Comparison

To facilitate comparison with the comparatively lower magnitude polar events, the reference calm ionospheric changes, phase scintillation indices, and carrier variations initially plotted in Figure 4-5 Figure 4-6 and Figure 4-7 respectively are re-plotted in figures Figure 4-51, Figure 4-52, and Figure 4-53 on axes that aid comparison with the polar scintillation.

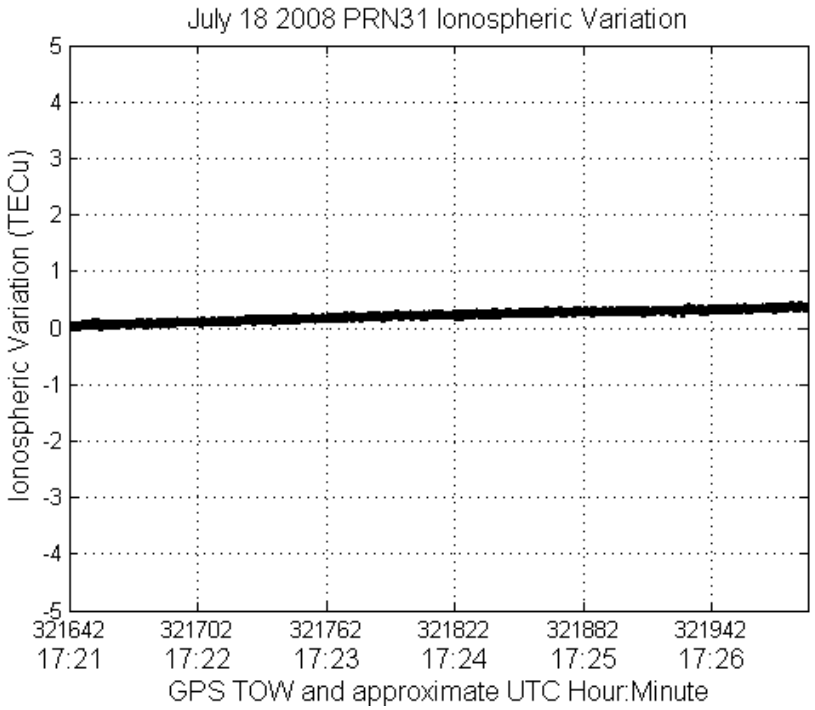

Figure 4-51: Ionospheric change over the reference data interval. Identical to Figure 4-5 with vertical scale adjusted for polar scintillation comparison.

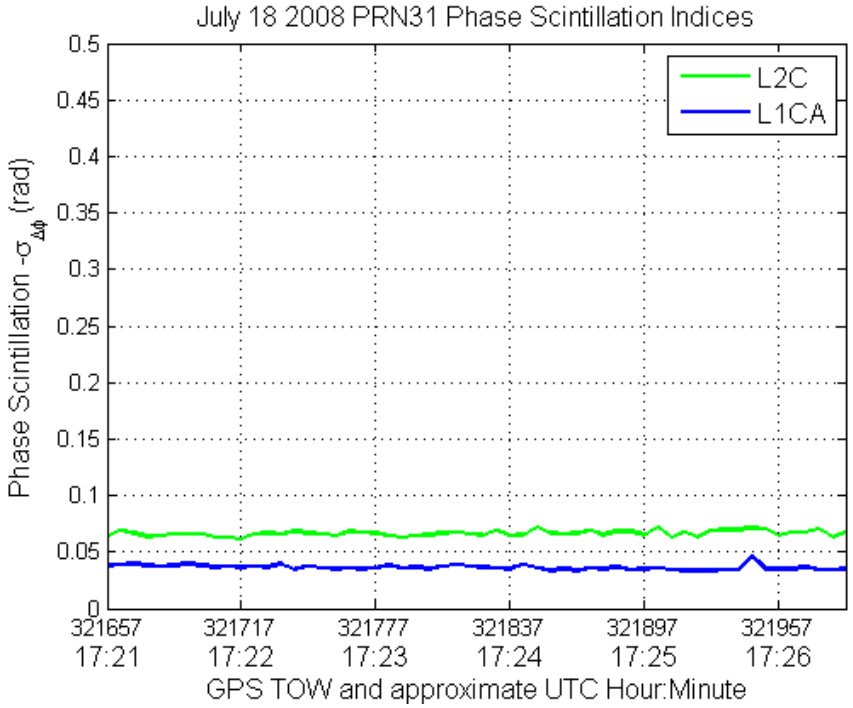

Figure 4-52: Phase scintillation indices over the July 18th 2008 reference data interval. Identical to Figure 4-7 with vertical scale adjusted.

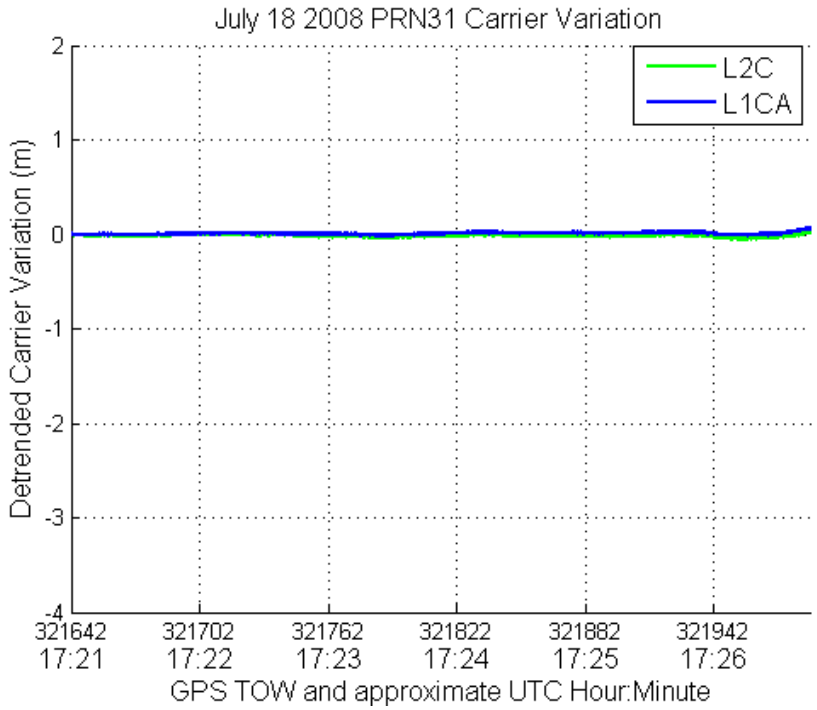

Figure 4-53: L1 and L2C carrier variation over the reference interval. Identical to Figure 4-6 with vertical scale adjusted for polar event comparison.

Unlike the auroral zone scintillation effects, it was anticipated that amplitude fading incidents would be observed frequently during polar scintillation events. S4 fading indices were calculated per equations (2.5) through (2.10) for all polar scintillation data, but it was found that the events which appeared to contain amplitude fading were also influenced by the effects of multipath. The chief indicator of multipath induced fading was that the C/N_0 levels and S4 fading indices would pose obvious periodic variations, which would not be expected from naturally occurring amplitude fades.

With this in mind, the analysis of polar phase scintillation effects was constrained to satellites and events which did not appear to be influenced by multipath, which comprised four events, each with satellites above 40 degrees of elevation.

Analysis of Weak Polar Scintillation Case I – polar Event A:

The relative TEC changes for polar Event A, plotted in Figure 4-54 are roughly ten times greater than in the reference case over the entire data interval, but local rates of change, particularly prior to 15:45 UTC are considerable, resulting in modest phase scintillation.

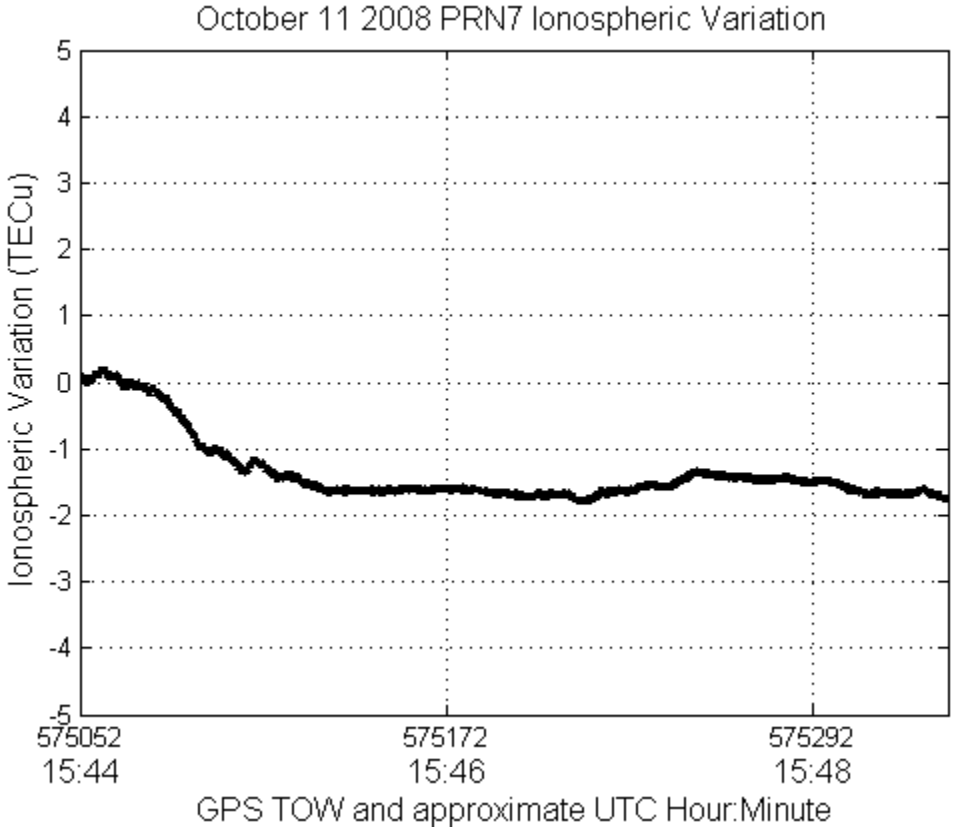

Figure 4-54: Ionospheric change measured via PRN7 observations over polar Event A.

The weak phase scintillation indices for polar Event A, plotted in Figure 4-55 indicate that the effects of polar phase scintillation seem to scale between L2 and L1 in a fashion similar to that noted of auroral phase scintillation. Similarly, the L1 and L2 carrier changes seen in Figure 4-56 confirm that the scintillation events observed by the carriers

are caused by interaction with nearly identical ionospheric conditions, as the carrier variations appear very well correlated.

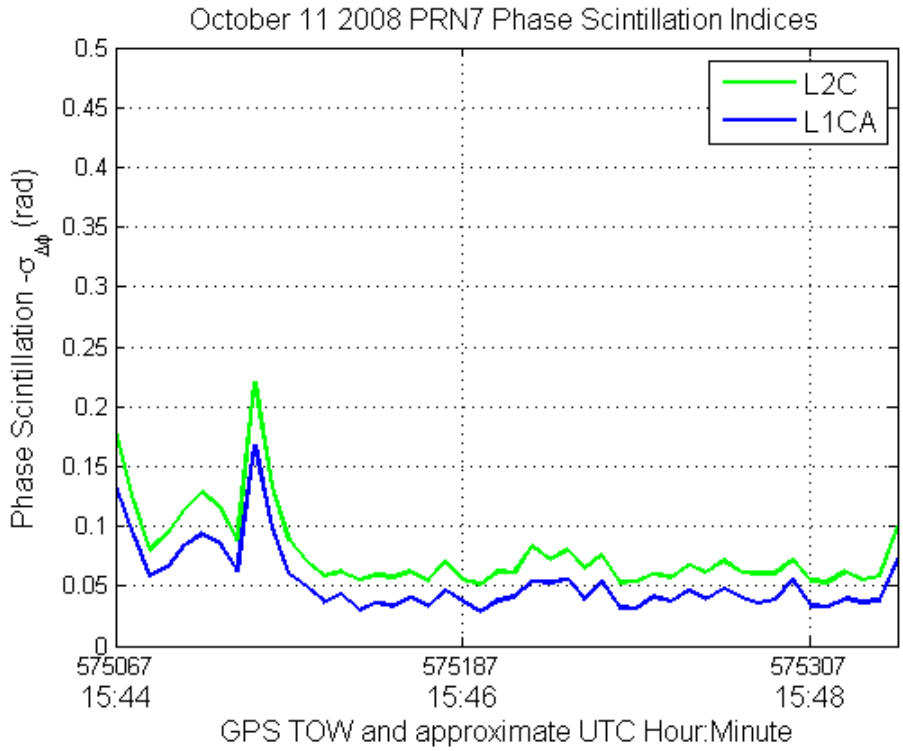

Figure 4-55: Phase scintillation indices over polar Event A measured from PRN7 carriers.

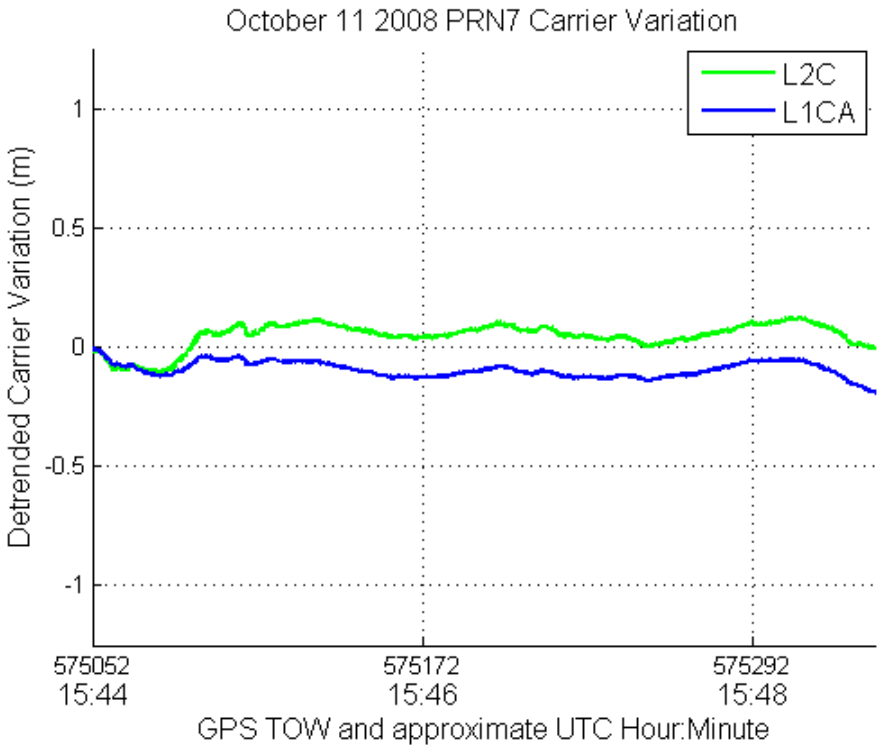

Figure 4-56: L1 and L2C carrier variation on PRN7 over polar Event A.

Analysis of Weak Polar Scintillation Case II – polar Event B:

Polar event B indicates a similar range of traversed relative TEC values as those of polar event A. Depicted in Figure 4-57, the relative TEC change for polar Event B again shows rapid small time duration variations indicative of disturbed ionospheric conditions.

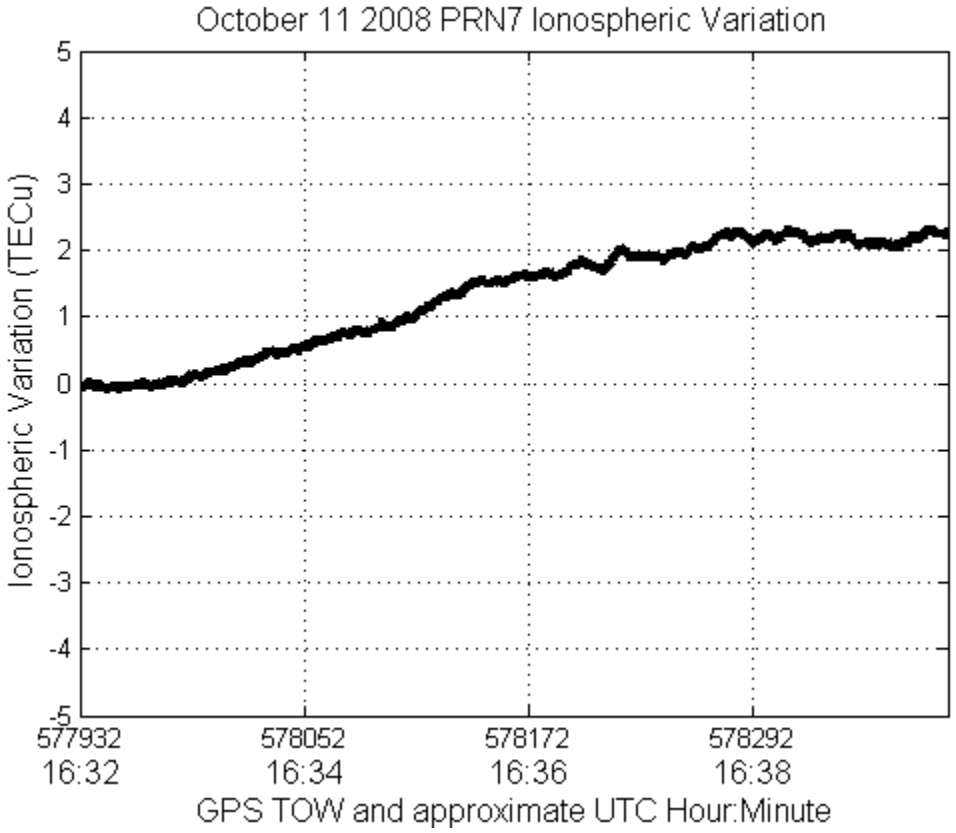

Figure 4-57: Ionospheric change measured via PRN7 observations over polar Event B.

The phase scintillation indices of polar Event B in Figure 4-58 as well as the carrier variation in Figure 4-59 confirm the observations of all auroral phase scintillation events, and of polar scintillation Event A. Thus far all scintillation observations considered have universally indicated high levels of correlation between the ionospheric features observed by the L1 and L2 GPS carriers.

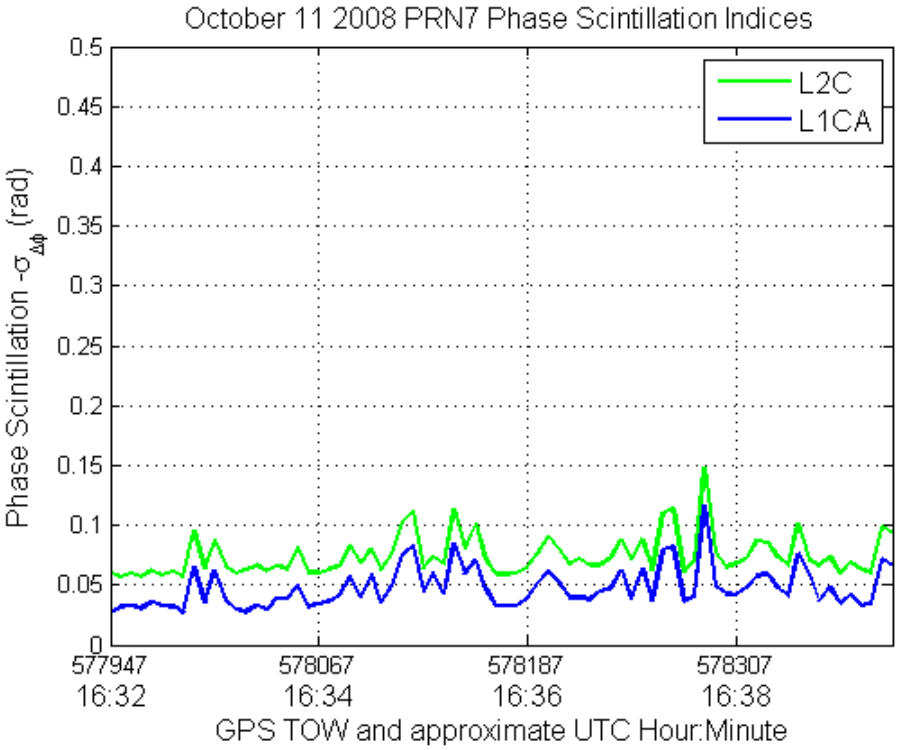

Figure 4-58: Phase scintillation indices over polar Event B measured from PRN7 carriers.

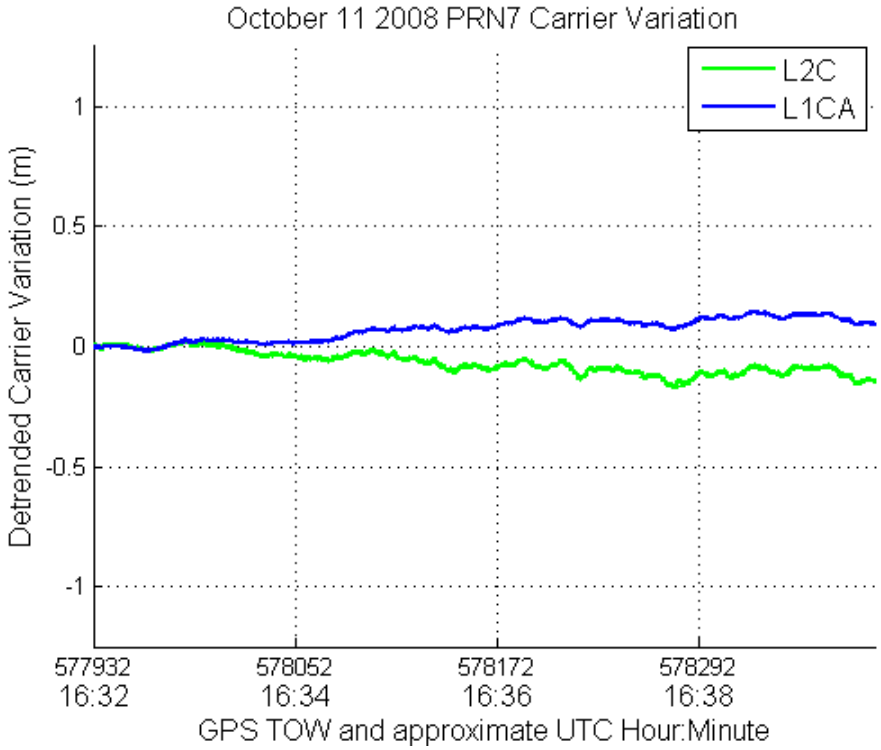

Figure 4-59: L1 and L2C carrier variation on PRN7 over polar Event B.

Analysis of Weak Polar Scintillation Case III – polar Event C:

The scintillation experienced by the PRN15 carriers during polar Event C could be described as quite low, barely meeting the 0.05 radian standard deviation threshold for 'very weak' phase scintillation with a 60 second detrending interval. However, using the six second detrending interval indicates that multiple events approaching 0.7 radians are recorded for L1. The TEC variations during polar Event C are plotted in Figure 4-60, while the phase scintillation indices and carrier variations are shown in Figure 4-61 and Figure 4-62 respectively.

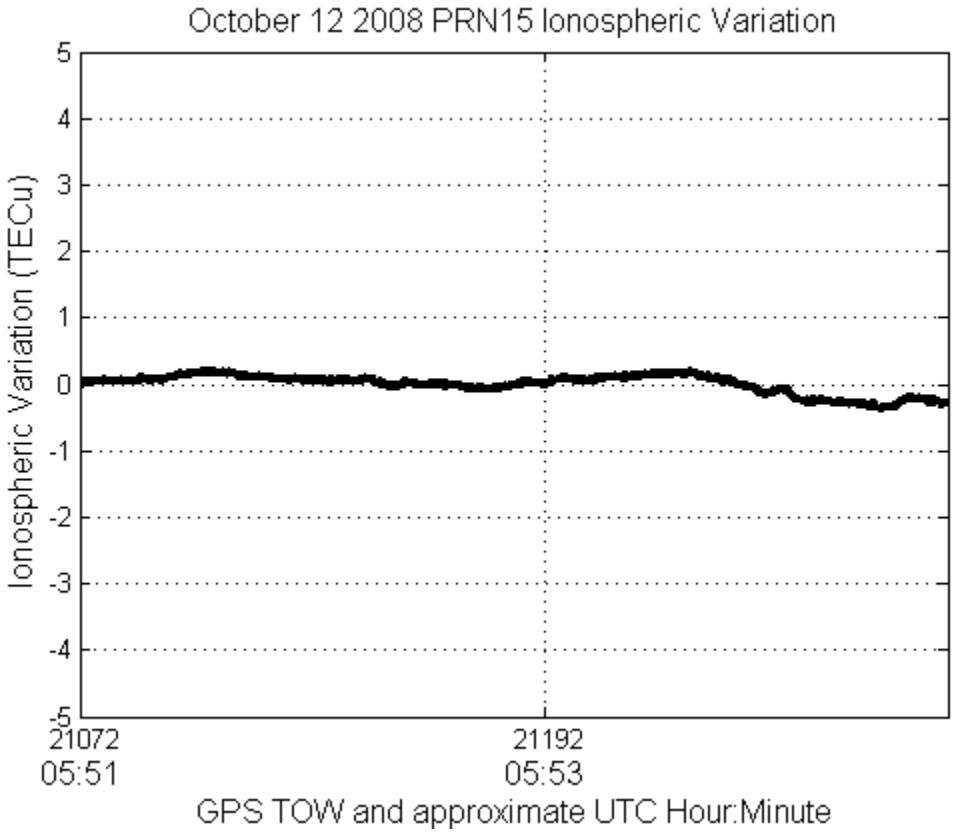

Figure 4-60: Ionospheric change measured via PRN15 observations over polar Event C.

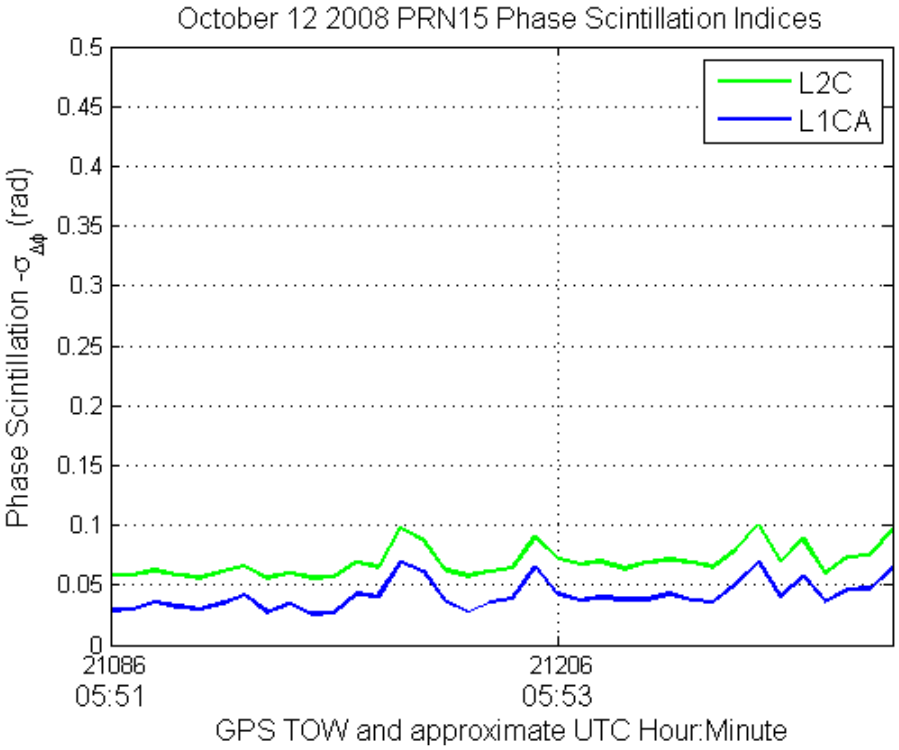

Figure 4-61: Phase scintillation indices over polar Event C measured from PRN15 carriers.

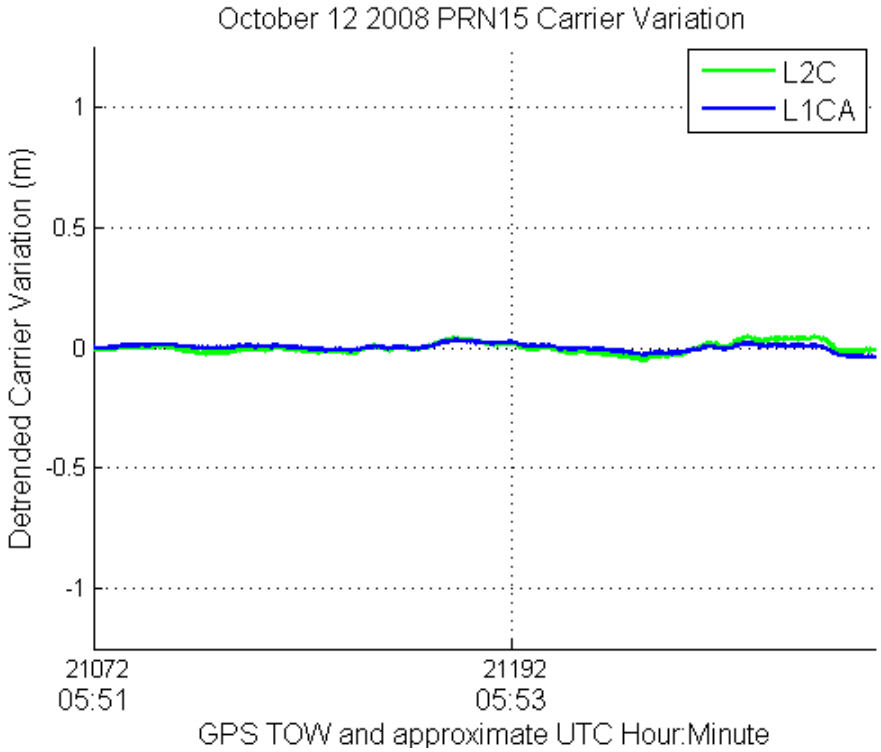

Figure 4-62: L1 and L2C carrier variation on PRN15 over polar Event C.

Analysis of Weak Polar Scintillation Case IV – polar Event D:

The TEC changes calculated by L1 L2 observations from PRN15 during polar Event D, plotted in Figure 4-63 are quite similar in character to those of the other polar events. Relative TEC variation is again roughly 10 times the range of the July 18 reference case, but unlike the reference data possesses several small, yet rapid changes, especially between 6:36 and 6:40 UTC.

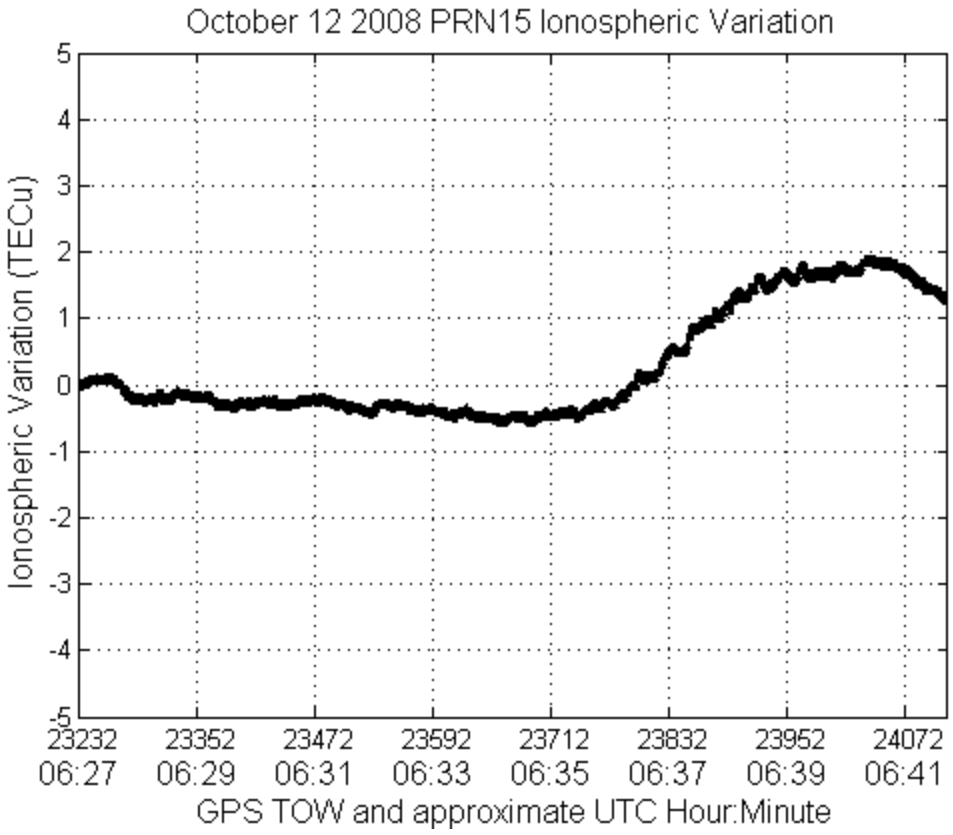

Figure 4-63: Ionospheric change measured via PRN15 observations over polar Event D.

The scintillation index and carrier variation plots in Figure 4-64 and Figure 4-65 confirm that the 6:36 to 6:40 UTC timeframe contained long duration, correlated phase scintillation effects on both L1 and L2 GPS carriers.

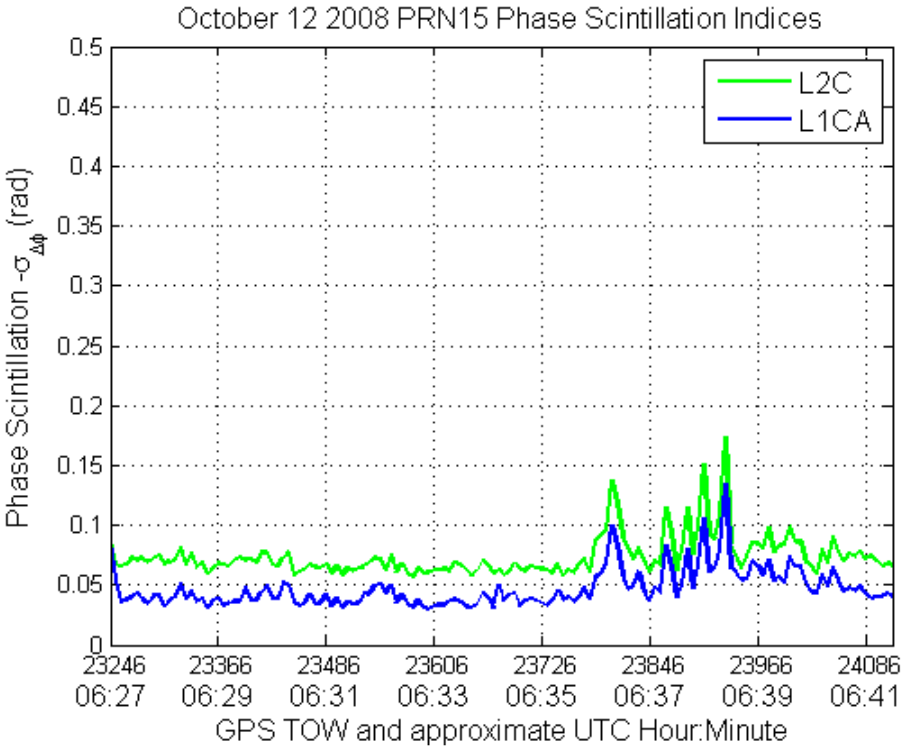

Figure 4-64: Phase scintillation indices over polar Event D measured from PRN15 carriers.

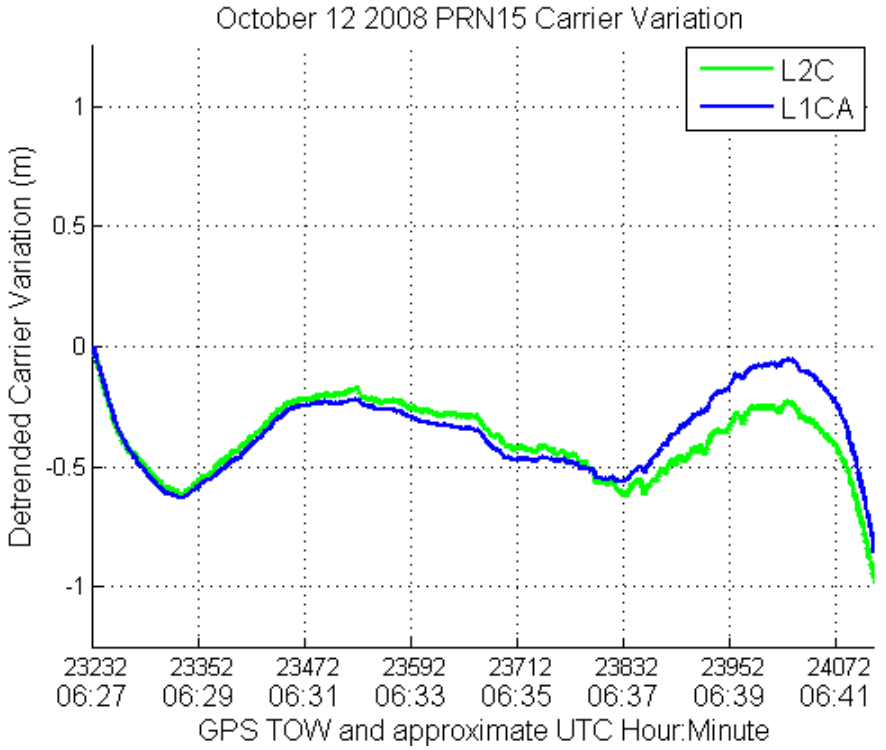

Figure 4-65: L1 and L2C carrier variation on PRN15 over polar Event D.

4.10 Polar Ray Path Sweep Rate Determination

Executing the same data processing strategy used to determine the ray path sweep rate through the disturbed ionosphere in the auroral scintillation scenarios, the polar scintillation event sweep rates are also calculated. Table 4-5 contains the initial and final azimuth and elevation angles between the GPS IF sample collection antenna and satellites experiencing phase scintillation, while Table 4-6 holds the associated initial and final IPP's for each SV.

Table 4-5: Azimuth and Elevation changes for IIR-M GPS satellites tracked during polar scintillation.

Polar Event and PRN	Initial Azimuth and Elevation	Final Azimuth and Elevation
Event A, PRN7	229.3^o Az, 54.4^o El	225.9^o Az, 55.0^o El
Event B, PRN7	193.5^o Az, 51.2^o El	189.3^o Az, 49.0^o El
Event C, PRN15	108.8^o Az, 50.5^o El	106.5^o Az, 49.9^o El
Event D, PRN15	90.5^o Az, 41.2^o El	86.1^o Az, 35.9^o El

Table 4-6: Ionospheric pierce points of satellite to user ray path of IIR-M GPS satellites tracked during polar scintillation, at 350 km altitude.

Polar Event and PRN	Initial Pierce Point (Lat., Lon.)	Final Pierce Point (Lat., Lon.)	Change on Interval (Lat., Lon.)
Event A, PRN7	78.5063^o,-95.1653^o	78.4613^o,-94.4860^o	0.04500^o,-0.6793^o
Event B, PRN7	77.6852^o,-89.1068^o	77.4743^o,-88.303^o	-0.2109^o,0.8038^o
Event C, PRN15	78.9745^o,-72.6678^o	79.0347^o,-72.2092^o	0.0602^o,0.4586^o
Event D, PRN15	79.4389^o,-66.611^o	79.5044^o,-62.7474^o	0.0655^o,-3.8636^o

Table 4-7 contains the calculated ray path sweep rates for each satellite used to observe polar scintillation events.

Applying the same analytical methods used with the auroral scintillation data to determine the frequency dependence of the TEC change weighted carrier correlation produces the data in Table 4-8. It must be noted however that the assumption of a fixed altitude charge distribution may not be an accurate representation of polar ionospheric anomalies. While not ideal, this approximation still provides insight.

Table 4-7: Arcs of travel, event durations, and resulting sweep rates for satellite to user ray paths during polar scintillation events

Polar Event and PRN	Arc Lengths (metres)	Event Duration (seconds)	Sweep rate through shell (m/sec.)
Event A, PRN7	15890	300	53
Event B, PRN7	30320	480	63
Event C, PRN15	11810	480	25
Event D, PRN15	78820	900	88

Table 4-8: Frequencies of maximum TEC weighted carrier correlation converted to encountered polar ionospheric anomaly sizes.

Polar Event/PRN	Freq. of Maximum Correlated Carrier Variation vs. Noise	Sweep Rate in metres/second (See Table 4-7).	Associated Anomaly Size (metres)
Event A PRN7	0.8 – 1.2 Hz	53	44 - 66
Event B PRN7	0.8 Hz	63	79
Event C PRN15	0.8 Hz	25	31
Event D PRN15	0.7 Hz	88	126

While the range of values varies by a factor of four between the smallest optimum correlation to noise associated scale size and the largest, the average value of these scale sizes is 72.75 metres. While encouraging, the tight agreement between the 72.75 metre optimum correlation size calculated here for weak polar scintillation events, and that of 74 metres calculated for strong auroral events must be taken in the context of the available data. A wide variation between individual data points within the polar and even

the auroral scintillation data sets exists whereby the removal or addition of a single additional data set to either could significantly alter the level of agreement between the average scale sizes.

The noted presence of correlated carrier activity well beyond the maximum correlation versus noise point in the auroral data remains true in the polar data, with preliminary testing showing the scale size at which actual carrier de-correlation occurs to be perhaps an order of 10 smaller than that calculated in Table 4-8.

4.11 Pulsation Events

During the analysis of Event C, an unexpected ionospheric disturbance not universally associated with scintillation was observed. The phase discriminator outputs of several but not all satellites tracked during this event showed a spectral spur at 0.648 Hz which was not present in the reference data set, nor in the other scintillation data sets. This spur indicated that the received signal carriers were modulated by a periodic variation in the ionosphere. This phenomena, known as 'ionospheric pulsation' is due to the interaction of the Earth magnetic field with the ionosphere (Skone 2010c). In this case it is also associated with the onset of a substorm event during auroral Event C, which is thought by some to be a common relationship (Posch et al 2006).

Pulsations are divisible into broad categories of those that are considered continuous and denoted 'Pc', and those which are described as irregular and denoted 'Pi'. Within each

category, subcategories are established based on the period or frequency of the pulsations occurring. The type of pulsations observed within Event C would be called irregular, since their character is irregular insofar as the pulsations are intermittently present over short time periods. Since the period of the pulsations in question is less than 1 second, their full classification would be Pi1.

Table 4-9: Constellation membership during auroral Event C pulsation event, with Elevation and Azimuth angles at 2:31 AM UTC.

PRN	Elevation	Azimuth
2	10.9	340.6
4	10.3	305.9
6	19.4	106.2
13	29.3	296.9
16	53.8	155.8
20	33.9	221.0
23	67.2	271.8
25	17.3	258.8
29	21.6	46.3
31	36.8	81.4

Note that while pulsation is present on almost all satellites it is not synchronized between satellites across the sky. A potential method of leveraging multiple carriers for the detection of small magnitude pulsation events was proposed by Skone (2010c) where it was shown that satellites with elevation angles above 60 degrees could observe the ionospheric manifestations of pulsation synchronously. Unfortunately since the auroral Event C data set contained few satellites which could be considered ‘close’ in the sky, and no two that were above 60 degrees simultaneously, this approach is not believed to be applicable here.

Confirmation of the difficulty in applying this approach in this case is shown in Figure 4-66, where it is apparent that the only satellites which have a simultaneous and 'in phase' pulsation event in common are PRNs 29 and 31 prior to 2:33 UTC. Since Table 4-9 indicates that these satellites were separated in azimuth by almost 180^{o}, and in elevation by more than 30^{o}, the synchronization of pulsation effects is likely coincidence.

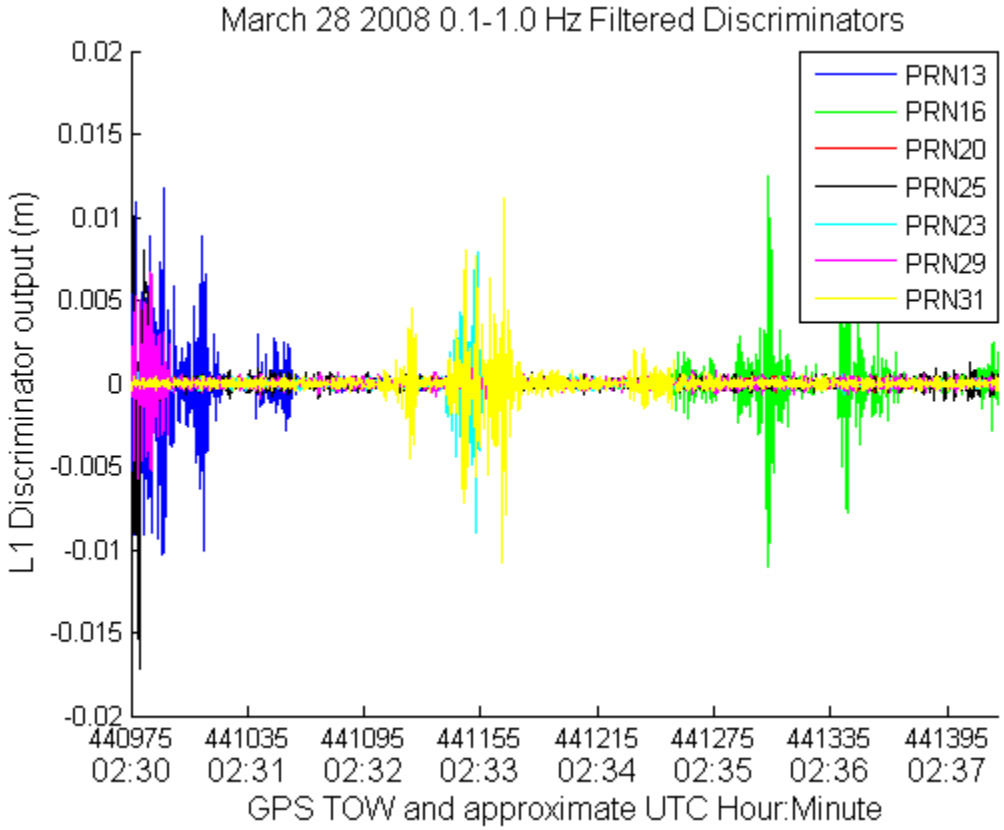

Figure 4-66: Filtered discriminator outputs during auroral Event C.

To serve as a point of comparison, identically filtered discriminator outputs from the July 18th calm reference data set are plotted in Figure 4-67.

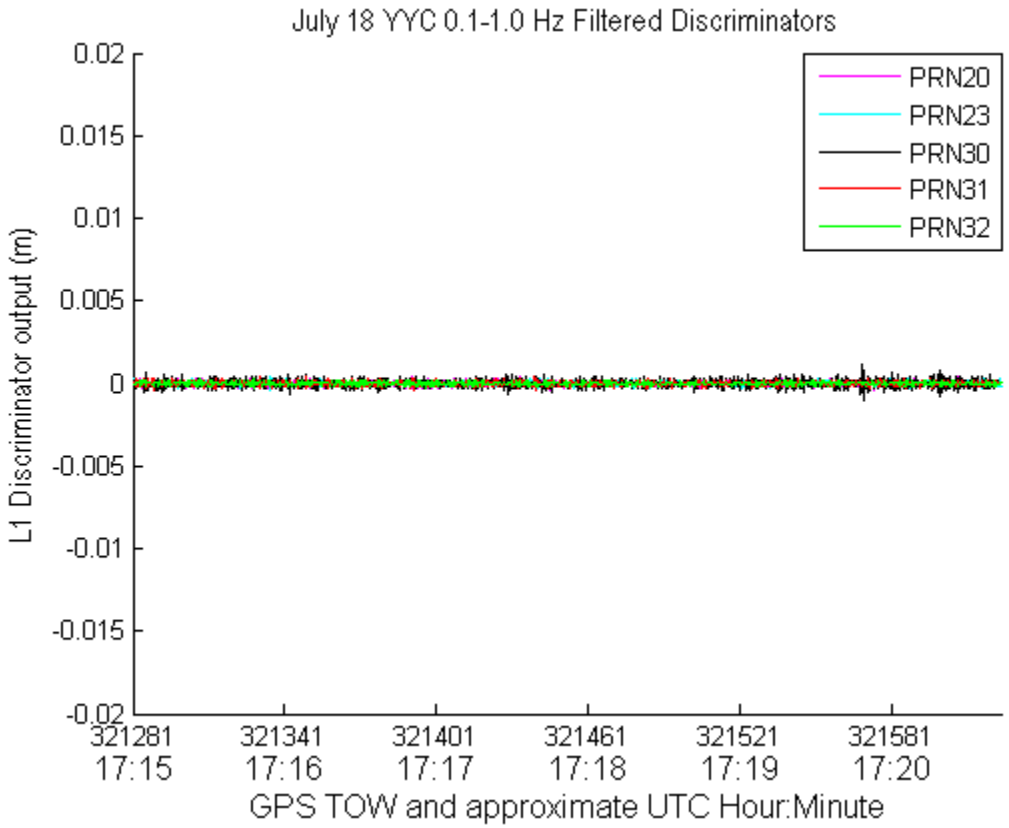

Figure 4-67: Filtered discriminator outputs during quiet reference data.

For all satellites visible in the July 18th reference data the filtered L1 discriminator outputs occupy a limited range., When converted to units of length all discriminators have maximum amplitudes of roughly +/- 1 mm over the entire data set. Compared to the discriminator outputs from auroral Event C, the magnitude of the pulsation effects on the discriminator outputs is roughly ten times greater than the influences of noise within the same bandwidth.

Moving to the question of the relative behaviour of pulsation between the L1 and L2 carriers, the filtered discriminator outputs from both the L1 C/A and L2C signals on

PRN31 are plotted in Figure 4-68 for the sub-segment of auroral Event C which contains pulsation.

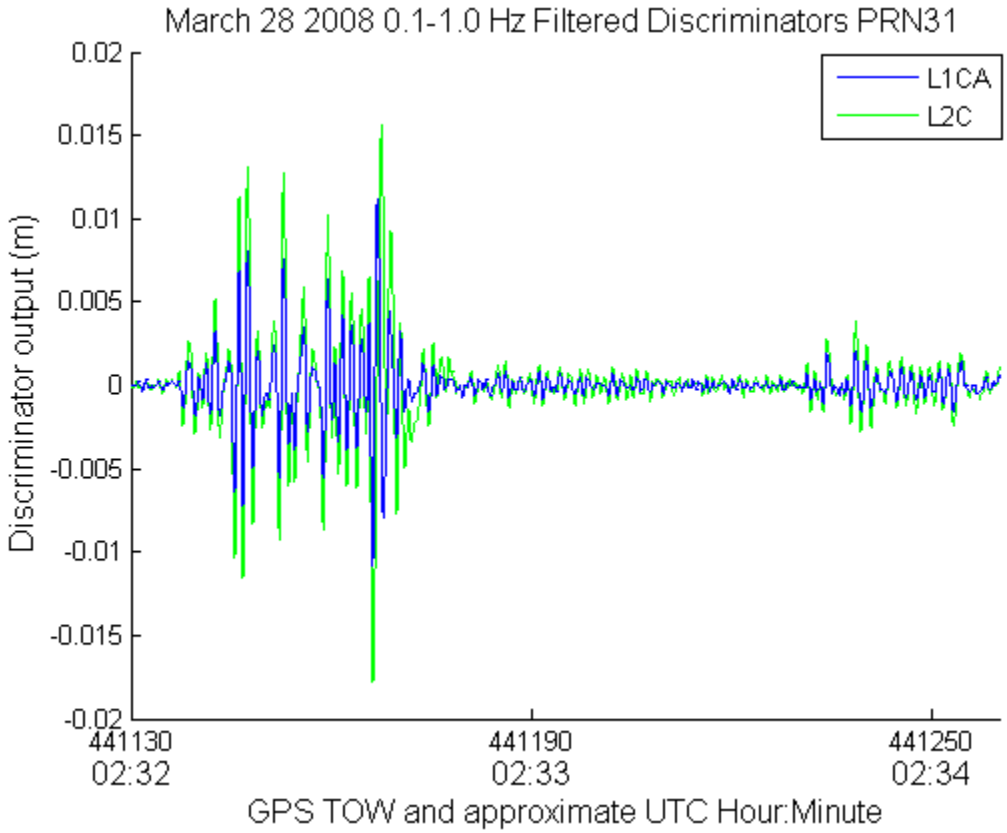

Figure 4-68: Filtered PRN31 discriminator outputs during a segment of auroral Event C.

Between 2:32 and 2:33 UTC the magnitude of pulsations reaches a peak value of +/- 12 mm on L1, or roughly 0.1 TECU. The L2 pulsation effect appears perfectly aligned with the L1 pulsation for the duration and is scaled in magnitude commensurate with the expected increased effect of ionospheric change on L2 relative to L1.

Interestingly, while the discriminator plots from Figure 4-66 appear to show bursts of pulsation events interspersed with quiet periods, the discriminators plotted for PRN31 in

Figure 4-68 show that low amplitude pulsation is present over a much larger portion of the data set. The discriminator outputs of both the L1 C/A and L2C signals near 2:33 UTC are consistent with 9.5×10^{-3} TECU of ionospheric change, and retain the approximate 0.65 Hz periodicity observed for other time periods on PRN31 and other PRNs in the data set.

While pulsations might not be considered rapid phase fluctuations, and are likely not a threat to GNSS carrier tracking, they remain a disturbed ionospheric phenomena, and are therefore of interest. For this reason, methods for detecting the presence of strong and weak pulsations events are now considered.

4.12 Derivation of pulsation detection methods

Detecting the relatively strong pulsation events prior to 2:33 UTC in figure Figure 4-68 could be accomplished by leveraging the much higher level of pulsation content relative to noise by taking the product of the L1 and L2 discriminator outputs. Adopting the notation used by Kay (1998b), and denoting a given epoch of the filtered L1 discriminator output as x_{L1}, and that of the L2 discriminator for the same epoch as x_{L2} produces a figure of merit which can be used to determine the presence or absence of a pulsation peak.

In this case, the test statistic $T(x)$ which indicates the presence or absence of pulsation when compared to a detection threshold γ can be stated as

$$T(x) = x_{L1}\, x_{L2} \rangle \gamma . \qquad \textbf{(4.13)}$$

In equation (4.13) a result greater than gamma would be declared detection of a pulsation event in the 0.1 to 1.0 Hz band, while a result under gamma would not. Gamma is set by selecting an acceptable level of false alarm or missed detection performance, and is discussed later.

The performance of the test statistic can be evaluated by comparing the mean and variance of the test statistic under each hypothesis (H_1: pulsation present, H_0: pulsation absent) if a signal model can be assumed for each of these hypotheses.

In this situation a signal model under H_1 is chosen, using the simplifying assumption that the amplitude of the effect on the L1 discriminator is equal to the effect on the L2 discriminator. This assumption will handicap the apparent performance of the detector somewhat, as ideally the amplitude of the L2 effect would be 1.283 that of the effect on L1, due to the dispersive nature of the ionosphere. Assuming further that the noise on the L1 discriminator is equal to the noise on the L2 discriminator results in an additional compromise to apparent performance as the civil signal broadcast at L2 is usually weaker than L1 by even more than satellite transmitter power levels would suggest. As previously explained in Section 4.1 this apparent signal strength is expected to be up to 7

dB lower on L2C than on L1 C/A for the combination of hardware and software used to collect and process the data considered.

With these assumptions in mind, one can express the signals from the L1 and L2 phase discriminator outputs as

$$x_1 = A + w_1 \quad \text{and} \tag{4.14}$$

$$x_2 = A + w_2 \tag{4.15}$$

where w_1 and w_2 are independent Gaussian noise influences at the output of the L1 and L2 discriminators and A is the immediate influence of the pulsation effect on each of the discriminators. The resulting expressions for the test statistic adopted in the previously introduced method under the given assumptions, as well as its mean and variance become:

$$T(x \mid H_1) = A^2 + A(w1 + w2) + w1w2, \tag{4.16}$$

$$\begin{aligned} E\left[T\left(x \mid H_1\right)\right] &= A^2 + A(0) + 0 = A^2 \\ E\left[T\left(x \mid H_0\right)\right] &= 0 \end{aligned} \quad \text{, and} \tag{4.17}$$

$$Var\left[T\left(x \mid H_0\right)\right] = 2\,\sigma^2. \tag{4.18}$$

where *E*[ ] and *Var*[ ] denote the expected value and the variance of the terms enclosed in the square braces, respectively.

By examining these equations, it is seen that detection performance improves as the ratio of the expected value of the test statistic under H_1 over the variance of the test statistic increases. Unfortunately, it is also obvious that if normalized such that noise power σ^2 was unity, a value of pulsation amplitude A less than unity would suffer 'squaring loss'. For strong pulsation relative to noise content however this squaring loss will actually be a squaring gain, indicating that this form of detector would be well applied to strong pulsation such as that prior to 2:33 UTC in Figure 4-68, but not necessarily to pulsation comparable in amplitude to in-band noise such as those present at or after 2:33 UTC in Figure 4-68.

Following from detection theory as discussed in Kay (1998b) it seems that a better option exists for detecting small amplitude pulsations, based on a matched filter/correlator that will not use the product of the L1 and L2 signals and therefore avoid the potential squaring losses associated with that approach.

If one reinterprets the data to consider the L1 and L2 phase differences to be two samples of the same value, but affected by independent noise processes, one then has 2 samples of the same process such that N=2. The form of x under the two hypotheses H_0, meaning pulsation absent, and H_1 meaning pulsation present becomes:

$$x \mid H_0 = w[n]; \qquad n = 0,1,.....N-1 \text{ or} \tag{4.19}$$

$$x \mid H_1 = s[n] + w[n]; \qquad n = 0,1,.....N-1 \tag{4.20}$$

where *s[n]* is the length 2 weighting vector of expected pulsation observations from the L1 and L2 carriers, and *w[n]* is the length 2 independent noise vector. In this case it is suitably convenient to choose *s[n]* as being either [1,1] to match the assumptions in the previous section, or as [1,1.283] to take into account the larger impact of pulsation effects on the carrier of the L2C signal. However, due to the previously mentioned significantly lower apparent power levels of the L2 carrier relative to the L1 carrier, a de-weighting should be applied to the second element to produce an equal noise contribution between the two samples. Assuming an antenna with equal gain at L1 and L2 GPS frequencies were available, and the L2C signal was tracked using both the pilot and data bearing portions, the de-weighting factor due to lower broadcast power would be 0.767. This value when multiplied with the previously mentioned scaling factor produces 0.985, which is close enough to unity to use 1.

The maximum likelihood ratio of the expressions is

$$L(x) = \frac{p(x;H_1)}{p(x;H_0)} \rangle \gamma \tag{4.21}$$

where H_0 and H_1 respectively indicate the absence and presence of pulsation.
Since the probability distribution function (PDF) of the output of an arctangent discriminator is very nearly Gaussian for a moderate to high C/N_0 levels, we can state these distributions as

$$p(x;H_1) = \frac{1}{\left(2\pi\sigma^2\right)^{N/2}}\exp\left[\frac{-1}{2\sigma^2}\sum_{n=0}^{N-1}\left(x[n]-s[n]\right)^2\right]\text{and} \tag{4.22}$$

$$p(x;H_0) = \frac{1}{\left(2\pi\sigma^2\right)^{N/2}}\exp\left[\frac{-1}{2\sigma^2}\sum_{n=0}^{N-1}\left(x[n]\right)^2\right]. \tag{4.23}$$

Substituting the PDFs of equations (4.22) and (4.23) into equation (4.21) yields

$$L(x) = \exp\left[\frac{-1}{2\sigma^2}\right]\left[\left(\sum_{n=(0)}^{N-1}\left(x[n]-s[n]\right)^2-\sum_{n=(0)}^{N-1}\left(x[n]\right)^2\right)\right]\rangle\ \gamma. \tag{4.24}$$

The log likelihood ratio is then a simplification of this expression and becomes

$$l(x) = \left[\frac{-1}{2\sigma^2}\right]\left[\left(\sum_{n=(0)}^{N-1}\left(x[n]-s[n]\right)^2-\sum_{n=(0)}^{N-1}\left(x[n]\right)^2\right)\right]\rangle\ \ln(\gamma). \tag{4.25}$$

To determine the performance of this new approach, we once again turn to an analysis of the expected values and variances of the test statistic. Utilizing the test statistic

$$T(x) = \frac{x_1 + x_2}{2}\rangle\ \gamma, \tag{4.26}$$

which for a matched filter with weights of unity and identical observed effects of amplitude A would become

$$T\left(x \mid H_1\right) = \frac{2A + w1 + w2}{2}, \tag{4.27}$$

the expected values and variance can then be determined. The expected value when pulsation activity is present is

$$E\left[T\left(x \mid H_1\right)\right] = A, \tag{4.28}$$

while the expected value in the absence of pulsation would simply be

$$E\left[T\left(x \mid H_0\right)\right] = 0. \tag{4.29}$$

The variance under the assumption that pulsation is present then becomes

$$Var\left[T\left(x \mid H_0\right)\right] = \frac{\sigma^2}{2}. \tag{4.30}$$

By examining the expected value and variance of the new detector, it is clear that the detection performance no longer suffers squaring loss for small pulsation effect amplitudes *'A'*, making this a more suitable choice for low amplitude events than the squaring detector.

To assess the performance of this detector it is necessary to quantify the expected noise level at the output of each the L1 CA and L2C discriminators. The standard deviation for unfiltered discriminators is plotted in Figure 4-69. The calculation of these discriminator noise levels is based on equations presented in section 5.5.1 and will not be expanded upon here.

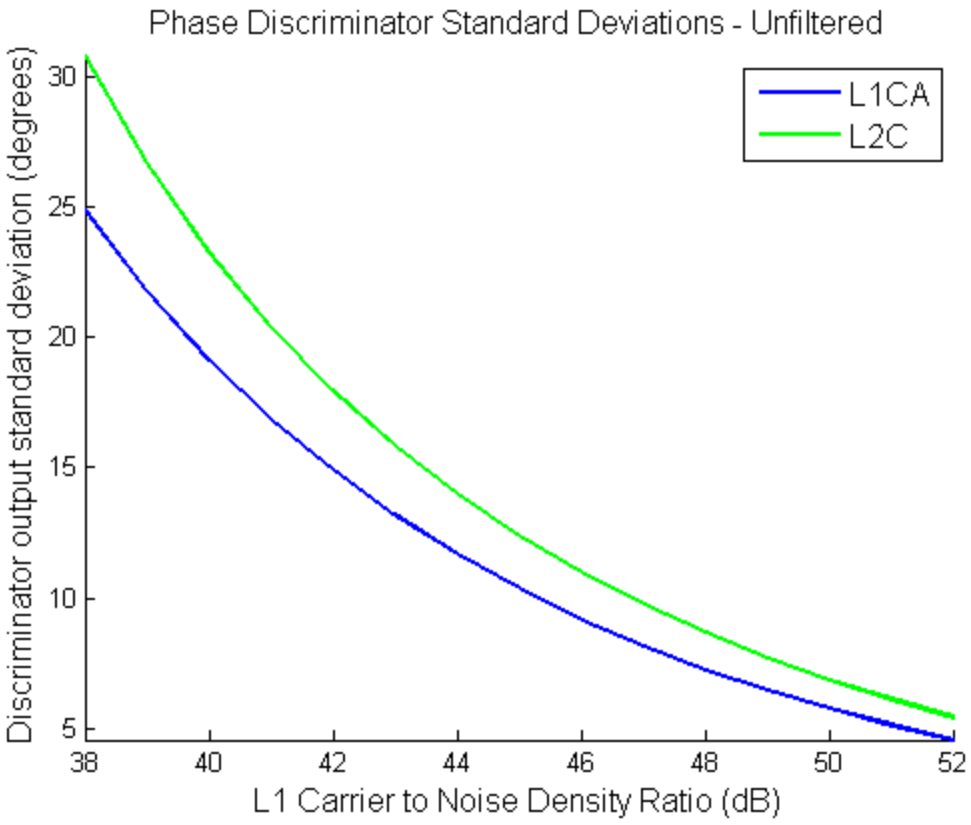

Figure 4-69: Standard deviation of 1 kHz discriminator outputs versus L1 Carrier to Noise Density

Assuming an L1 carrier to noise density ratio of 45 dB, the standard deviations of the L1 and L2 discriminators are 10.35^{o} and 12.39^{o} respectively. Applying these values to the detector described by equations (4.19) through (4.30) with fixed probabilities of false

alarm of 1 per 100 and 1 per 1000 leads to the pulsation magnitude versus pulsation detection probabilities plotted in Figure 4-70. The gamma threshold for the 0.001 probability of false alarm case is 0.152 TECU, while that of the 0.01 probability of false alarm probability is 0.119 TECU.

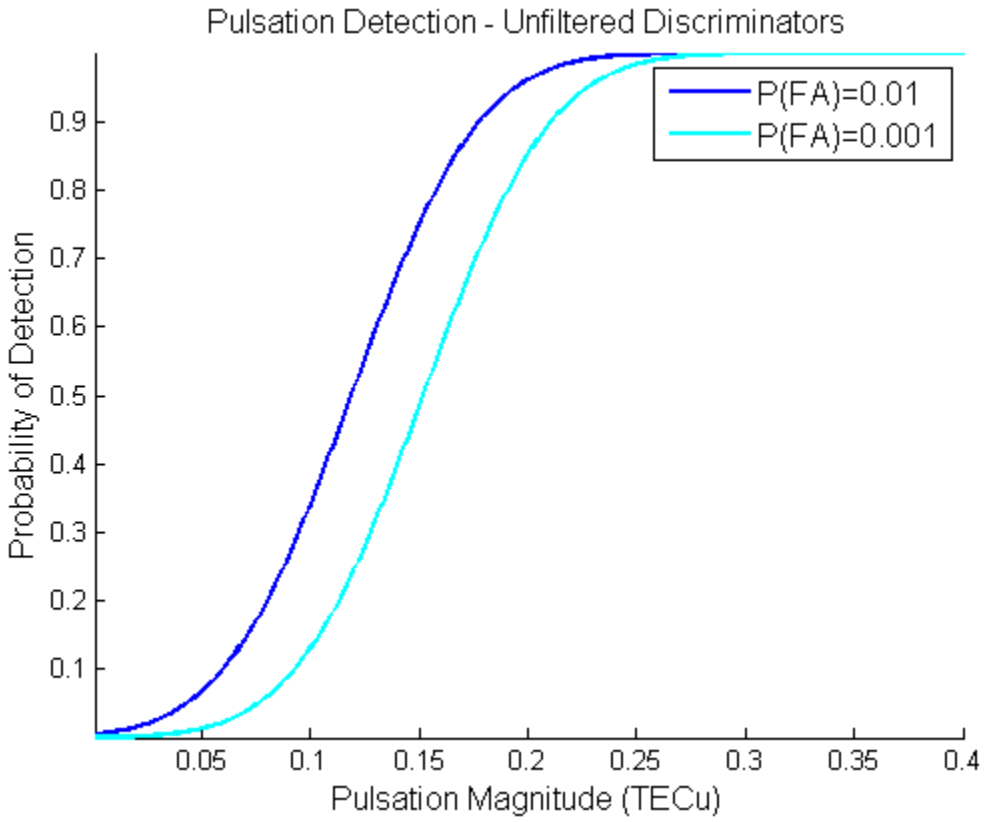

Figure 4-70: Detection Probability Versus Pulsation Magnitude Using Unfiltered Discriminators With L1 C/N_0 of 45 dB.

Recalling that for a coherent integration length of 1 ms, the rate of discriminator outputs will be 1 kHz, the probability of false alarms presented for the unfiltered discriminators may prove excessive. This detector as implemented would be expected to register on

average one or ten false alarms per second to achieve even this modest detection performance, which would likely be an impractically high false alarm rate.

Since the frequency of the pulsation phenomena of interest is known to be less than 1 Hz, it is appropriate to attempt to decrease discriminator output noise by either increasing the coherent integration time used or by filtering the output of the discriminators, both of which reduce the variance in the observation. When band-passed filtered between 0.1 and 1.0 Hz, the standard deviation of the discriminator outputs is reduced to the values shown in Figure 4-71, which is a small fraction of the uncertainty present in the unfiltered discriminator outputs.

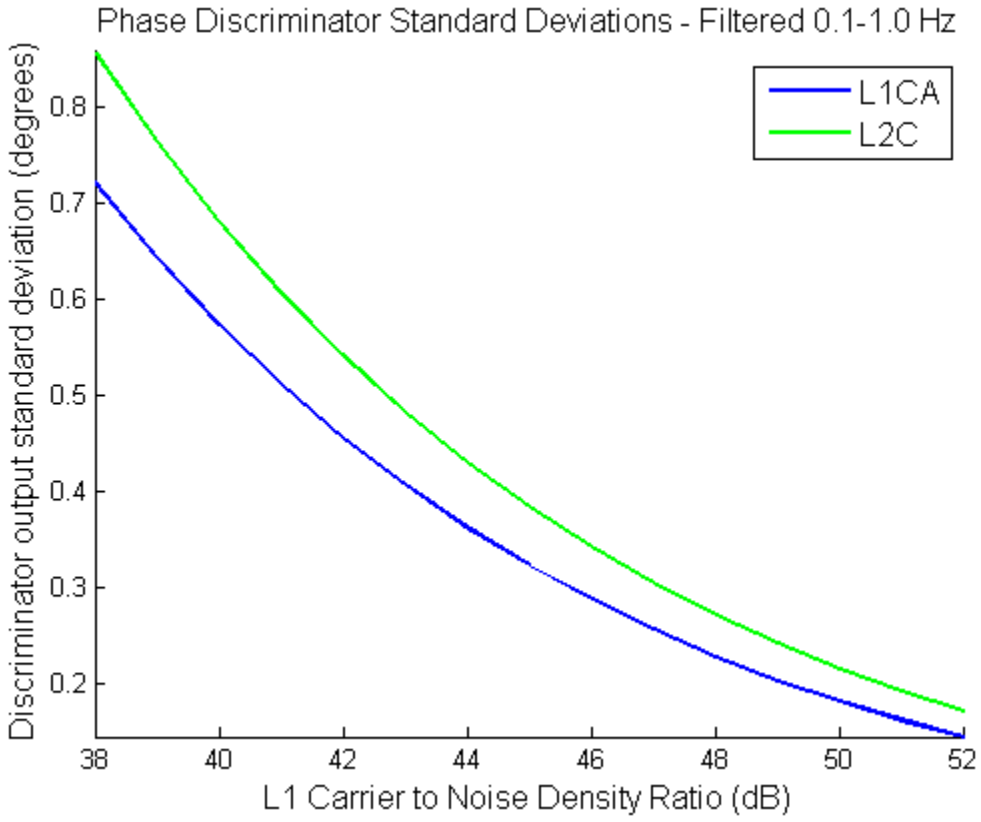

Figure 4-71: Standard deviation of 1 kHz filtered discriminator outputs versus L1 Carrier to Noise Density

The detection performance increases substantially, even after constraining the detector to false alarm rates 100 times less frequent than that in the previous case, as is plotted in Figure 4-72. This plot agrees well with the earlier careful observation of Figure 4-68 which indicated that pulsations creating Ionospheric changes of less than $1x10^{-3}$ TECU would be easily observable when using filtered discriminator outputs, even when allowing for very low false alarm rates.

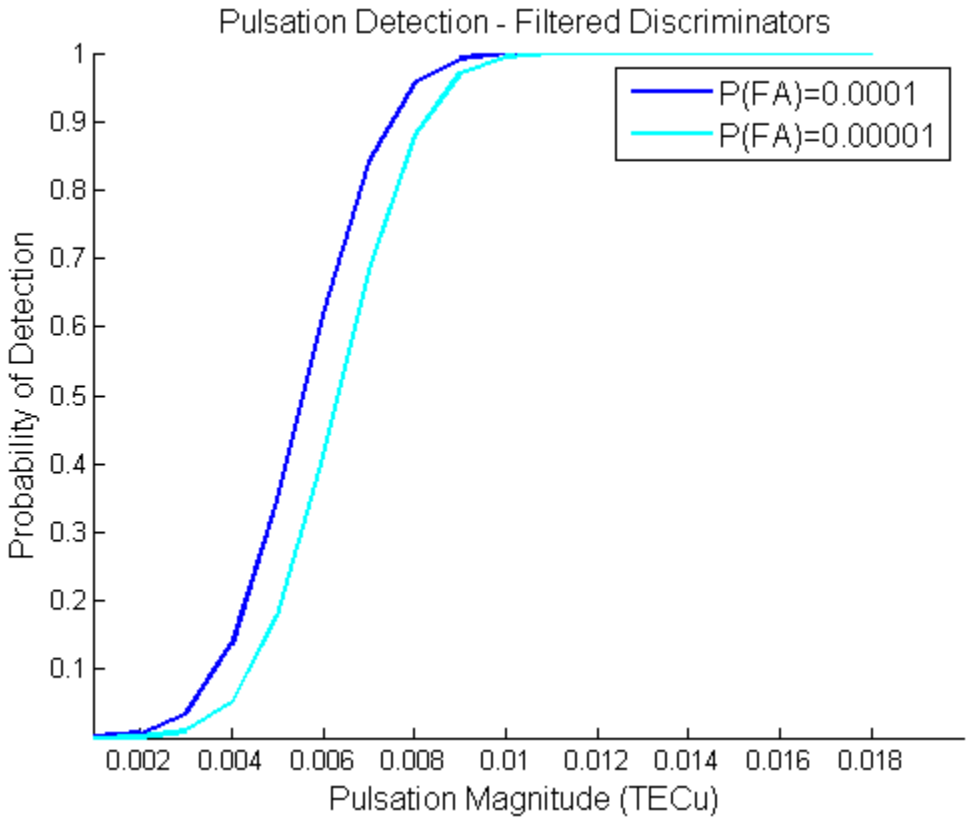

Figure 4-72: Detection Probability Versus Pulsation Magnitude Using Filtered Discriminators With L1 C/N_0 of 45 dB.

4.13 Potential benefits of additional carriers

As the number of civilian accessible signals broadcast by an individual GNSS satellite increases, the potential utility of the latter detection method also increases. This increase in utility derives from three basic factors. Firstly, from the reduction of relative noise influence through the addition of aggregate received carrier power, which is apparent from examination of equations (4.27) through (4.30). This increase of the ratio of the expected value under the presence of scintillation to the variance of the test statistic for N carriers of identical strength experiencing a common pulsation effect would be

$$\frac{N \cdot A}{\sigma^2} \tag{4.31}$$

The second factor which should offer increased observability of the pulsation effects follows from equation (2.2), which when expressed in terms of cycles of the given carrier rather than units of fixed length shows that the phase effect will be more easily observed on lower frequency carriers, and proportional to the inverse of the carrier frequency. Assuming the correlations identified between the L1 and L2C signals were to hold for the L5 signal, the latter would experience an effect roughly 1.34 times that observed on L1.

4.14 SVN48 Anomaly

During the course of both the Eureka and the Churchill data collection periods, many more events of marginal phase scintillation were reported by the co-located scintillation monitor on SVN48/PRN7 than any other. At the time of the Churchill collection, this was considered extremely fortuitous since SVN48 was launched less than two weeks prior. Analysis of this data showed very odd characteristics, not at all consistent with the observations of scintillation collected via other satellite observations. Plotted in Figure 4-73, the apparent ionospheric variation contains what appear to be instantaneous steps in TEC just prior to 6:38 UTC and more obviously just following 6:40 UTC.

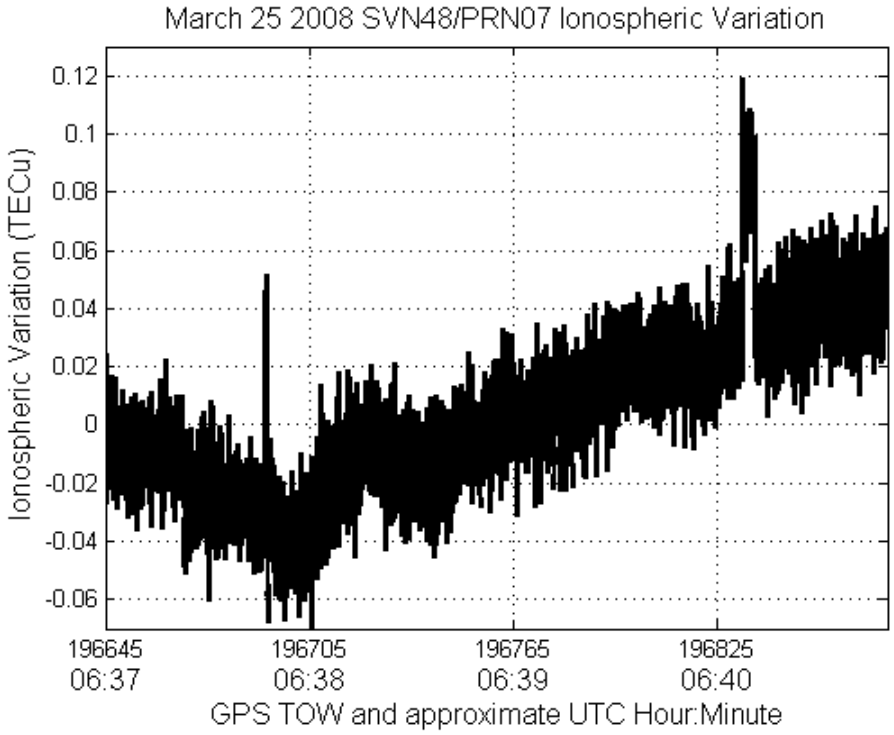

Figure 4-73: Ionospheric variation measured by PRN7 during Chruchill data collection effort, containing apparent step functions in TEC.

Observing the L1 and L2C carriers surrounding the latter step function in Figure 4-74 confirms that these variations are not the result of naturally occurring changes in the

ionosphere between the user and the satellite. Indeed, the apparent change in encountered TEC appears to be caused by a signal anomaly exclusive to the L1 carrier broadcast by this SVN.

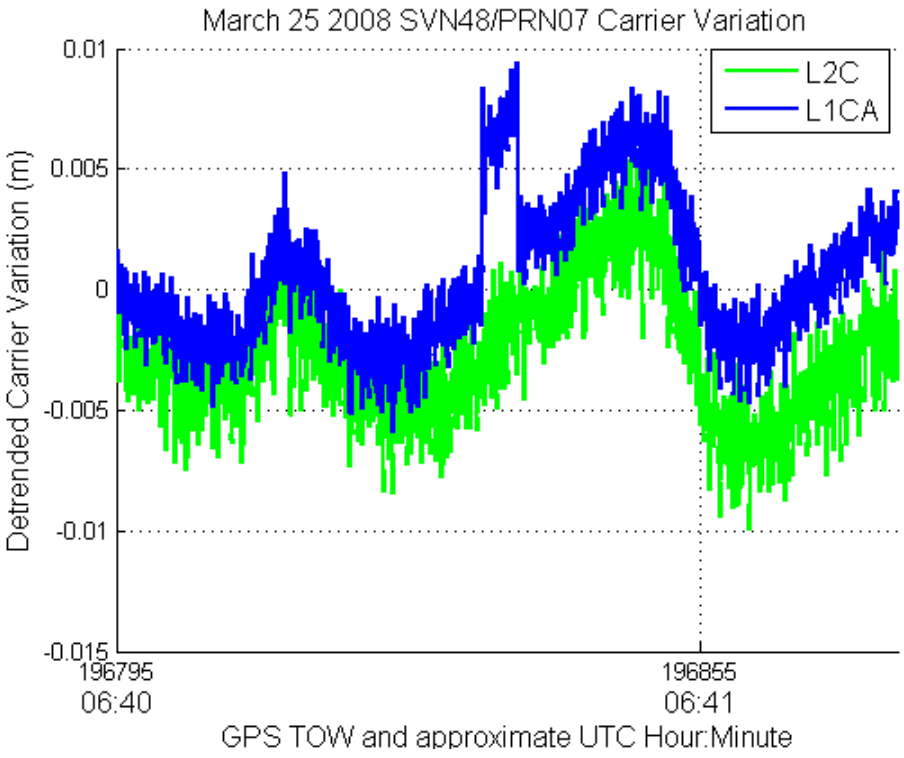

Figure 4-74: L1 and L2C carriers of SVN48 showing L1 carrier anomaly.

This roughly 5 mm step discontinuity has since been confirmed by O'Hanlon et al (2010) and shown to occur at seemingly random intervals on only the L1 carrier of SVN48. Since the presence of this anomaly was not determined prior to the Eureka collection effort, the criteria for declaring scintillation present based on the outputs of the co-located scintillation monitor were not adjusted. This resulted in a large number of 'minor' scintillation events collected that in fact contained no such activity, and were triggered only by the L1 carrier anomaly discussed.

4.15 Other Phase Scintillation Considerations

When considering any of the discussed methods of phase scintillation detection including the standard method created and popularized by Van Dierendonck (1999) and Van Dierendonck & Hua (2003), as well as the newly proposed pulsation detection methods, special attention must be given to the system hardware used. Since phase noise in the local oscillator will map into phase noise in each of the down-converted GNSS carriers, the magnitude of the phase noise in the local oscillator must be limited so as not to artificially inflate the apparent phase scintillation indices.

For any of the methods of phase scintillation or pulsation detection to be effective, the contribution of oscillator phase noise in the observation bands must be kept to a minimum. The most straightforward method of achieving this goal is the use of a low phase noise OCXO, which was done by the author for both the polar and auroral latitude data collection efforts. The utilization of this equipment however adds significant cost, weight, and power consumption to the user equipment needed, making the reliable detection and accurate quantification of ionospheric phase scintillation impossible for consumer grade GNSS receivers.

To allow for ionospheric phase scintillation detection and potential subsequent mitigation in low cost mass produced GNSS hardware, it is necessary to provide a new method for estimating in-situ the phase noise contribution of the local oscillator. To this end, the next chapter introduces a novel method for the determination of the epoch to epoch phase instability in the local system oscillator for a GNSS receiver.

Chapter Five: Oscillator Effects and Mitigation

5.1 Introduction

Inside a GNSS receiver, the local timing reference is a critical component. Depending on the context it may be referred to as the clock, the oscillator, the reference standard or simply the reference, owing to the fact that it is the source of both time and frequency determination within the user equipment. The timing error or 'clock bias' in the local reference is typically dealt with as a term to be solved within the user navigation solution, while any frequency offset in the clock is solved for by observing the rate of change of the clock bias. It is not possible to produce a reference clock which is perfectly synchronous and syntonous to a GNSS constellation, except where this clock is defined as being perfect, such as the Central Synchronizer (CS) of the GLONASS (RISDE 2008) system, or the US Naval Observatory references used in the GPS system (JPO 2004). Even in the special case of these defined reference clocks, their will remain a small time, frequency, and phase error between the defined reference and every satellite in the given GNSS constellation, due to the noise present in all timing references, even the very precise atomic clocks used onboard GNSS satellites as well as the extremely stable terrestrial reference clocks. This noise and instability can be expressed using an Allan Deviation plot of the timing stability of a given oscillator (NIST 2010), where fractional stability is expressed as a function of interval or averaging time.

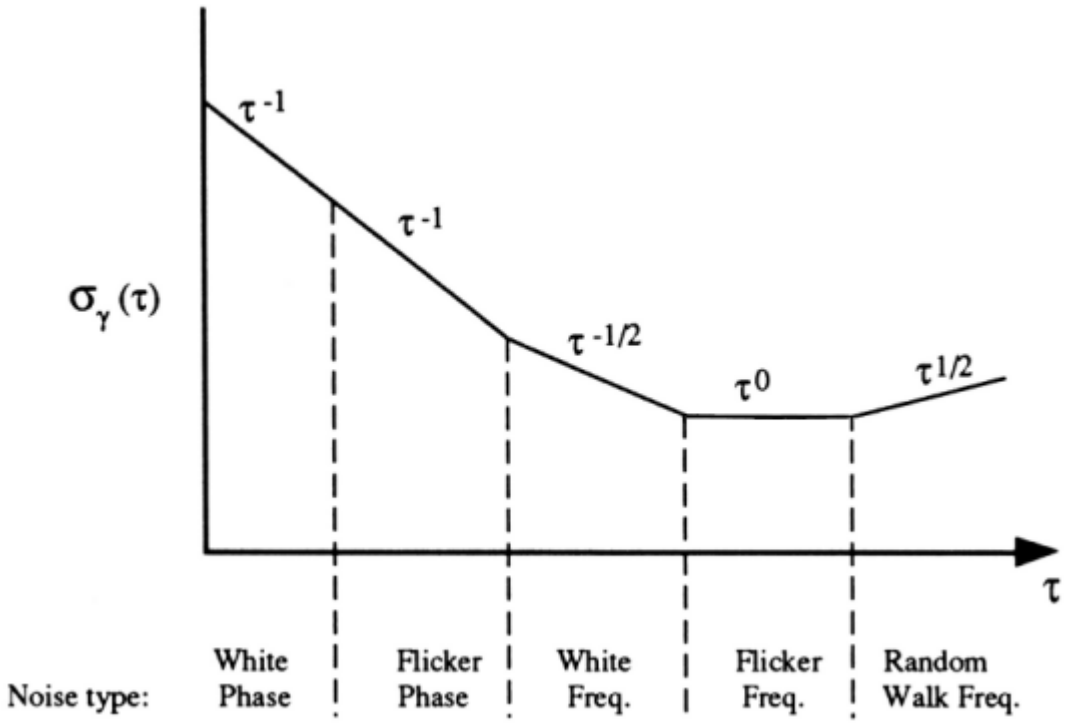

Figure 5-1: Allan Deviation plot showing relative positioning of different noise processes versus averaging interval (NIST 2010).

In the Allan Deviation plot, it is apparent that different noise processes dominate at different averaging intervals. It follows that different GNSS receiver operations will be affected most by certain noise processes or combinations of noise processes. For example, acquisition using an Almanac will be heavily influenced by the accumulated timing error, as well as frequency offset, both of which are functions of the long term Random Walk Frequency Modulation (RWFM) noise processes. During normal operation, the contributions of these noise processes are negligible, as their extremely low frequency nature relative to the navigation solution means that in a properly operating system they are estimated or estimated and removed by definition. In contrast, the noise

processes which dominate at averaging intervals not corrected by the navigation solution will remain uncorrected and negatively influence receiver performance.

Depending on the application, these uncorrected phase noise components will lower the apparent C/N_0 of the signal (NovAtel 2000) or simply prevent proper operation as explained in Van Dierendonck (1999). For scintillation detection applications, extremely low phase noises are necessary, and traditionally require the use of expensive, physically bulky, and electrically power hungry Ovenized quartz clock sources. In the following section a novel method of providing low phase noise observations that does not require the use of an Ovenized quartz source will be presented.

5.2 Signal Model

To understand how a low phase noise observation can be provided without the use of a low phase noise clock, it is necessary to examine the expressions for the signal and clock noise components within a typical GNSS receiver.

$$\begin{aligned} S_{L1}(t) &= A' C_P(t) W(t) D(t) C\,\mathrm{os}[(\omega_0 + \Delta\omega)t + \phi_0] + \ldots \\ &\ldots + \sqrt{2} A' C_{CA}(t) D(t) Sin[(\omega_0 + \Delta\omega)t + \phi_0] \end{aligned} \tag{5.1}$$

where

A' = P Code amplitude,

$C_{CA}(t)$ = C/A PRN code modulation (± 1),

$C_P(t)$ = P PRN code modulation (± 1),

$D(t)$ = 50 bps navigation data modulation (± 1),

$W(t)$ = Anti Spoofing Encryption Sequence (± 1),

$\omega_0 = 2\pi f_0$ = Angular Carrier Frequency,

$\Delta\omega$ = Frequency offset (Doppler, clock drift, etc.), and

$\emptyset_0$ = Nominal (but ambiguous) carrier – phase.

Breaking from the analysis in Raquet (2006) the C/A portion of the signal is focused on, as this is the component of use to the vast majority of users. Further, to allow simplification of the following expressions an alteration is introduced to let $A = \sqrt{2}A'$ = Amplitude of C/A code portion of signal. This small change is used to simplify the amplitude term for the C/A code portion of the signal prior to down conversion to IF and filtering.

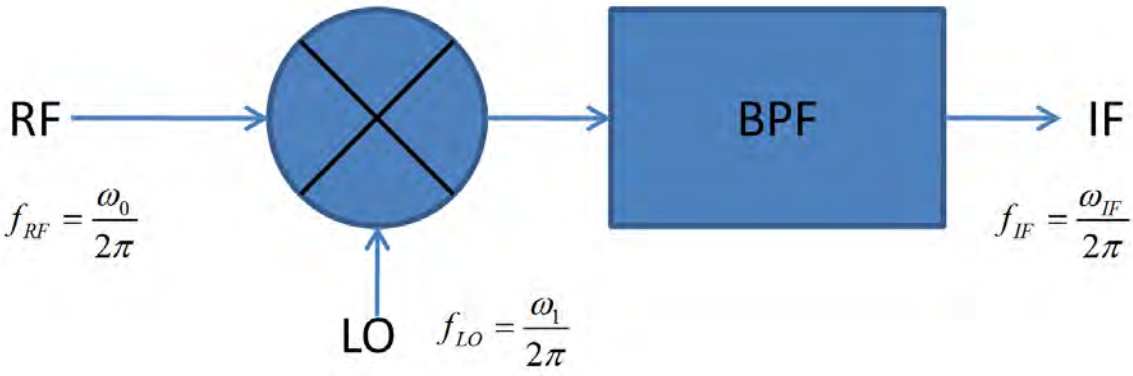

Figure 5-2: Standard architecture for down conversion and filtering of a GNSS carrier.

Within Figure 5-2 the expression for the LO signal is given as

$$LO(t) = 2\cos(\omega_{LO}t - \theta_{LO}(t)), \tag{5.2}$$

Where

$\omega_{LO}t = 2\pi f_{LO}t$ = Angular Local Oscillator Frequency,

$\theta_{LO}(t)$ = time varying phase error in local oscillator

resulting in the expression for the intermediate frequency signal

$$S_{IF}(t) = AC_{CA}(t)D(t)Sin[(\omega_{IF} + \Delta\omega)t + \phi_0 + \theta_{LO}(t)]. \tag{5.3}$$

If one accounts for the noise processes in the local oscillator by adding a traditionally omitted time varying phase error term, as is done in equation (5.2), the IF signal seen in equation (5.3) will now contain this term as well as the normally considered phase term. Since the result of further processing the signal through Doppler removal, de-spreading, integration and application to a carrier tracking discriminator is the recovery of the phase of the signal, it becomes obvious that the normal process of estimating local carrier phase also estimates the phase noise contribution of the local oscillator.

The detection of this time varying phase term will be discussed in Section 5.4, along with the considerations needed to separate this time varying phase effect from the effects of platform dynamics and noise. The following two sections are adapted from Morrison

(2009), the publication in which this novel method of isolating oscillator phase noise was first presented.

5.3 Typical Receiver Operation

Inside a typical GNSS receiver the estimate of the error in the local oscillator is formed only as a component of the navigation solution, which is in turn based on the output of each satellite tracking channel propagating its estimate of carrier and code measurements to a common future point independently of one another. While this method of creating apparently simultaneous measurements is necessary, it regrettably limits the resolution with which the noise of the local oscillator can be quantified due to the scaling of non-simultaneous samples of local oscillator noise through the measurement propagation process. Before introducing the proposed new phase error estimation method, it is necessary to first understand the limitations imposed by the conventional receiver architecture, with respect to accurately estimating short term oscillator behaviour.

In a typical receiver, while information about local time offset and local oscillator frequency bias may be recovered, information about the phase noise in the local oscillator is distorted and discarded (as a consequence of scaling non-simultaneous observations to a common epoch) as represented in Figure 5-3.

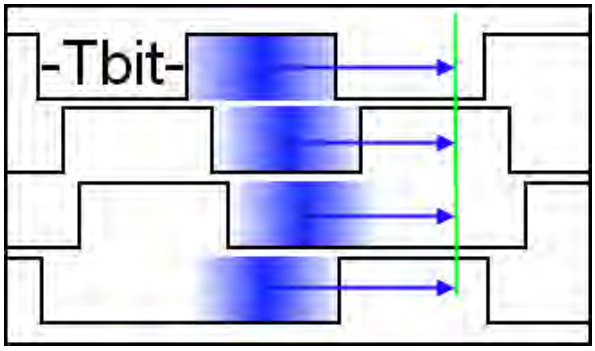

Figure 5-3: Visual representation of the propagation of non simultaneous 1-bit coherent integration time observations in individual channels to a common measurement epoch as described in Morrison(2009).

As shown in Figure 5-3, coherent summation intervals in a receiver are used to approximate values of the phase error, including oscillator phase, measured at the non-simultaneous interval centres in each channel. This is necessitated by the non-simultaneous nature of the bit transitions received at the user antenna, due to differing user to satellite ranges, as well as satellite clock offsets. These interval centre phase estimates are then propagated to a common navigation solution epoch. Each channel will intrinsically contain a partially overlapping midpoint estimate of oscillator noise over the coherent summation interval in each channel. As these estimates are not totally overlapping, they do not make optimal use of the information available regarding the effects of the local oscillator, and form a poor basis for estimating the contributions of this device to the uncertainty in the channel measurements at short time intervals. As shown in Figure 5-1, the phase error noise process in the local oscillator at short averaging intervals is dominated by white phase noise. Since this dominant white noise is uncorrelated between any two points, the only way it may be removed is via direct observation at each point of interest.

5.4 Novel Proposed Method

To overcome the limitations of a typical receiver, it is necessary to record the approximate bit timing and history of each tracked satellite as well as a short segment of past samples. Through this retained data it is guaranteed that the bit period boundaries of the satellites will not pose an obstacle to forming common N-ms coherent periods between all visible satellites, over which simultaneous integration may proceed by wiping off bit transitions. Using this approach as depicted visually in Figure 5-4, all available constellation signal power is used to estimate a single parameter, namely the epoch-to-epoch phase change in the local oscillator.

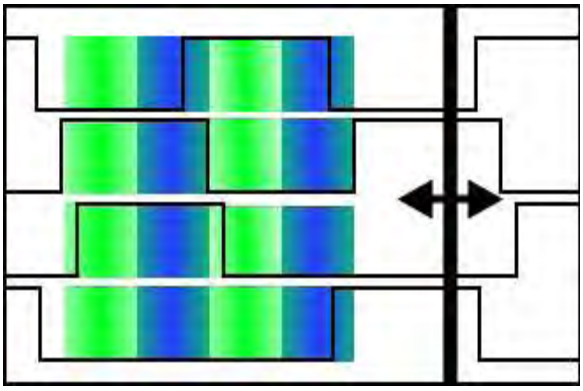

Figure 5-4: Common intervals over which coherent integration may proceed on all channels, from Morrison (2009). This diagram shows consecutive half bit length coherent integrations along with bit boundaries.

With the knowledge that it is possible to create common periods of coherent integration across all channels via bit wipe off and a small processing delay, it becomes evident that it is possible to avoid the previously mentioned non-overlapping and scaled estimates of local oscillator phase noise. Instead it is possible to form time synchronized estimates of

the phase contribution of the common system oscillator alternately across one N-ms time slice, then the next, in turn forming an unbroken time series of estimates of the phase change of the system oscillator. Specifically, forming the difference between the adjacent discriminator outputs in this manner will provide the following information:

1) The ΔEps (change in the noise term in the local loop)

2) The ΔOsc (change in the phase of the local oscillator – the parameter of interest, and previously introduced as the $\theta_{LO}(t)$ term in equation (5.2))

3) The ΔDyn (change in the untracked/residual of real and apparent dynamics of the local loop/estimator)

Noting that term 1 may be considered entirely independent across independent PRNs (GPS, GALILEO, COMPASS) or frequency channels (GLONASS), and that the value of term 3 over a 10 ms period is expected to be small over these short intervals, it becomes obvious that term 2 may be recoverable from the available information. To determine the feasibility of recovering a meaningful estimate of the oscillator phase change, the magnitude of the oscillator phase noise must be contrasted against the measurement error.

5.5 Expected Performance

5.5.1 Calculation of variance at output of ATAN2 discriminator

To allow the realistic weighting of discriminator output deltas it becomes desirable to estimate at very short time intervals the variance of the output of the phase discriminator. In the case of a 2 quadrant arctangent discriminator this means one wishes to quantify the variance of $\tan^{-1}\left(Q/I\right)$, where *Q* and *I* are the quadrature-phase and in-phase prompt correlator outputs. Letting the ratio of *Q* over *I* be referred to as *Z*, and recalling that in general if *Y=aX* then the PDF of *Y* becomes:

$$f_y(y) = \frac{1}{|a|} f_x\left(\frac{y}{a}\right). \tag{5.4}$$

Applying this to the variance of the input to the arctangent discriminator in terms of the in phase and quadrature accumulators, this would give the variance of the input term *Z*:

$$\sigma^2(Z) = \frac{\sigma^2(Q)}{I^2}. \tag{5.5}$$

Rather than proceed with a direct evaluation from this point onward to determine the expression for the variance at the output of the discriminator, it is convenient to recognize that simpler alternatives exist since g(z) is in this case atan(z) and therefore:

$$\frac{d(g(Z))}{dz} = \frac{1}{1+Z^2}. \tag{5.6}$$

The implication being that since the slope of the arctangent transfer function is very nearly equal to 1 in the central, typical operating region, and universally less than 1 outside of this region, it is easy to recognize that the variance at the output of the arctangent discriminator is universally less than that at the input, and can be pessimistically quantified as the variance of the input, or $\sigma^2(Z)$. This assumption has been verified by simulation, the result of which is shown in Figure 5-5, where the response has been shown after taking into account the effect of operating at a point anywhere in the range +/- 45 degrees. While the consequence of the simplification of the variance expression is an exaggeration of discriminator output variance, it is seen in Figure 5-6 that the variance of the output is well bounded by the estimate, and within a small margin of error for strong signals.

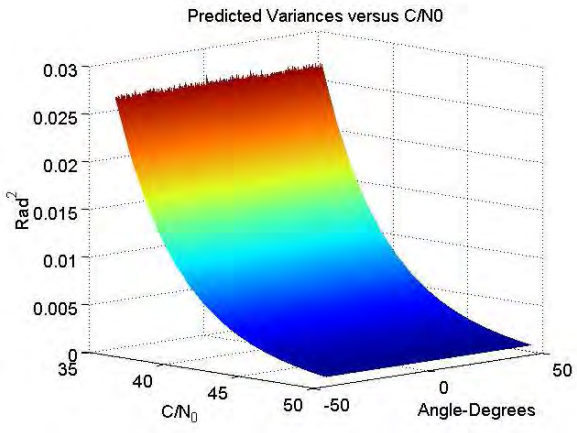

Figure 5-5: Predicted Variances at output of ATAN discriminator versus carrier to noise density ratio estimated at each coherent interval (Morrison 2009).

The gap between real and predicted output variance may also be narrowed in cases where Q>I by using a type of discriminator which interchanges Q and I in this case and adds an appropriate angular offset to the output as:

$$\sigma^2_{Discri\,mOutput} \sim\leq \frac{\sigma^2_{Normalized}}{MAX\{I,Q\}}. \tag{5.7}$$

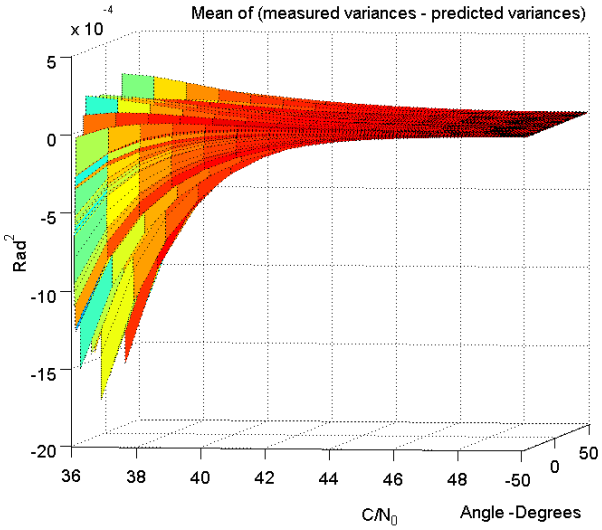

Figure 5-6: Difference between actual and predicted discriminator output variance from Morrison (2009).

Proceeding in this vein, the next required parameter is the normalized variance of the In-phase and Quadrature arms, which are calculated as follows (Borio and O'Driscoll 2007): Given that the carrier amplitude can be expressed to be the square root of the sum of the squared values of the I and Q branches or

$$A = \sqrt{I^2 + Q^2}\,, \tag{5.8}$$

results in a carrier power *C* that is

$$C = \frac{A^2}{2}. \tag{5.9}$$

Further, since the noise power is calculated from noise density and bandwidth as

$$\sigma^2 = 2N_0 B, \tag{5.10}$$

expressing bandwidth B as the inverse of the coherent integration time, and rearranging now gives noise density N_0 as

$$N_0 = \frac{\sigma^2 T}{2}. \tag{5.11}$$

Combining this expression, and the one previously given for the carrier power C in equation (5.9) results in the following expression for the carrier to noise density ratio:

$$\frac{C}{N_0} = \frac{A^2}{\sigma^2 T}. \tag{5.12}$$

This latest expression can be rearranged to find the desired variance term. Assuming the 10ms coherent integration time discussed earlier is used, this yields

$$\sigma^2 = \frac{100A^2}{C/N_0}. \tag{5.13}$$

Normalizing for the carrier amplitude gives the normalized variance in terms of radians squared:

$$\sigma^2_{Normalized} = \frac{100A}{C/N_0}. \tag{5.14}$$

Note that in any situation where the carrier is sufficiently strong to be tracked, it is likely that the carrier power term employed above can be gathered from the immediate I and Q values, ignoring the contribution of the noise term to its magnitude.

5.5.2 Calculation of the expected magnitude of the epoch-to-epoch oscillator phase effect.

Determining the expected magnitude of the local oscillator phase deviation requires only three steps, assuming that certain criteria can be met. The first requirement is that the averaging times in question must be short relative to the duration at which noise processes other than white phase, and flicker phase modulation begin to dominate the noise characteristics of the oscillator (Lombardi 2008a). Typically the crossover point between the dominance of these processes and others is above 1 s in averaging interval length, when quartz oscillators are concerned (Vig 2004a). Since this paper discusses a

specific implementation interval of 10 ms within systems expected to be using quartz oscillators, it is reasonable to assume that this constraint will be met.

The second requirement is that the Allan deviation of the given system oscillator must be known for at least one averaging interval within the region of interest. Since the Allan deviation follows a linear slope of -1 with respect to averaging interval on a log-log scale within the white phase noise region, this single value will allow an accurate prediction of the Allan deviation at any other point on the interval, and in turn, of the phase uncertainty at the 10 ms averaging interval level.

Letting $\sigma_A(\tau)$ represent the Allan deviation at a specific averaging interval, recall that this quantity is the midpoint average of the standard deviation of fractional frequency error over the averaging interval τ, per NIST (2010), and Johansson (2008). Scaling this quantity by a frequency of interest results in the standard deviation of the absolute frequency error on the averaging interval as discussed in Lombardi (2008b), and IEEE 1139/D3 Annex C (2008). The expression for this quantity is $\sigma_A(\tau) \bullet F_{Carrier}(Hz)$.

By integrating this average difference in frequency deviations over the coherent period of interest, one obtains a measure of the standard deviation in degrees, of a signal generated by this reference

$$\sigma_{Carrier} = \frac{\sigma_A(\tau) \cdot T_{Coherent} \cdot F_{Carrier} \cdot 360^o}{2}. \qquad (5.15)$$

Note that the averaging interval τ, is identical to the coherent integration time.

Turning to a practical example, if the oscillator in question has a 1s Allan Deviation of 1 part per hundred billion (1 in 10^{11}), a stability value between that of an OCXO and MCXO standard according to Vig (2004b), and shown to be somewhat pessimistic by Leapsecond (2008**),** this would scale linearly to be $1e^{-9}$ at a 10 ms averaging interval, under the previous assumption that the oscillator uncertainty is dominated by the white phase noise term at these intervals. Also, for illustration purposes if one assumes the carrier of interest to be the nominal GPS L1 carrier, the uncertainty in the local carrier replica due to the local oscillator over a 10 ms coherent integration time becomes:

$$\frac{(360^o \cdot 1e^{-9} \cdot 1e^{-2} \cdot 1.57542e^{9})^o}{2} = 2.836^o . \tag{5.16}$$

When stated in a more readily digested format, this represents roughly 15 cm per second in the line of sight velocity uncertainty. Keep in mind that in an operating receiver there are additional factors which serve to modify this effect. The first is that this noise contribution is filtered by the bandwidth limiting effects of the local loop filter resulting in a modification to the noise affecting velocity estimates, as well as reduced information about the behaviour of the local oscillator.

5.5.3 Impact of apparent dynamics

When considering the error sources within the system, it is important to realize which individual sources of error will contribute to estimation errors, and which will not. One area of potential concern would appear to be the errors in the satellite ephemerides, encompassing both the satellite orbit trajectory misrepresentation and the satellite clock error. While the errors in the satellite ephemerides are of concern for point positioning, they are not of consequence to this application, as the apparent error introduced by a deviation of the true orbit from that expressed in the broadcast orbital parameters does not affect the tracking of that satellite at the loop level. Additionally, while the satellite clock will add uncertainty to the epoch to epoch phase change within each channel independently, the magnitude of this change is minimal relative to the contribution of uncertainty due to the variance at the output of the discriminator guaranteed by the low carrier to noise density ratio of a received GNSS signal. Since this contribution is uncorrelated between satellites and relatively small compared to other noise contributions affecting these measurements, even when compared to the soon to be discontinued URAGAN GLONASS satellites which had generally less stable onboard clocks Revnivykh et al (2005) it is likely safe to ignore. When compared to the more stable oscillators aboard GPS or GLONASS-M satellites, it is a very reasonable assumption that this will be a dismissible contribution to received signal phase uncertainty.

While atmospheric effects present an obstacle which will directly affect the epoch-to-epoch output of the discriminators, it is believed that under conditions that do not include the effects of ionospheric scintillation, the majority of the contribution of apparent dynamics due to atmospheric changes will have a PSD heavily concentrated below a

fraction of one Hz (Olynik et al 2002). The consequence of this concentration is that the tracking loops will remove the vast majority of this contribution, and that the difference operator that will be applied between adjacent phase measurements, as in the case of dynamics, will nullify the majority of the remaining influence.

5.5.4 Impact of real dynamics

Real dynamics present constraints on performance, as do any tracking loop transients. For example, a low bandwidth loop tracking dynamics will have long lasting transients of a magnitude significant relative to levels of local oscillator noise. For this reason it is necessary to adopt a strategy of using the epoch-to-epoch change in the discriminator as the figure of interest, as opposed to the absolute error value output at each epoch. This can reasonably be expected to remove the vast majority of the effects of dynamics of the user on the solution.

In order to validate this assumption under typical conditions, a short verification example is called for. Arbitrarily selecting the use of a 2^{nd} order PLL for carrier tracking, with a 10Hz loop bandwidth, the effects of dynamics on the loop are given by the following equations (Ward & Betz 2006).

Letting Noise Bandwidth (*Bn*) be 10 Hz and following the previously mentioned reference:

$$Bn = 0.53\omega_0, \tag{5.17}$$

Therefore, the value of ω_0 is

$$\omega_0 = 18.87 Hz . \tag{5.18}$$

Recall that the steady state tracking error in a 2nd order tracking loop is given by

$$\frac{d^2 R}{dt^2} \Big/ \omega_0^2 = \Delta Dyn \tag{5.19}$$

Given the choices above, a line of sight dynamic stress of a constant 1 metre per second squared acceleration would result in a constant offset of 0.00281 cycles, or 1.011 degrees of constant tracking error due to dynamics. Since this constant bias will be eliminated by the difference operator discussed earlier, it is necessary to examine higher order dynamics.

Further, if one used a coherent integration interval of 10 ms as assumed earlier, and let the dynamics of interest be a jerk of 1 g/s, this results in a midpoint average of 0.005 g on this interval:

$$0.005G = 0.0491 \, m/s^2 \tag{5.20}$$

$$0.0491 \, {}^{m}\!/_{s^2} = 0.252 \, {}^{cycle}\!/_{s^2} \tag{5.21}$$

Substituting this result into equation (5.19) produces the associated change in dynamic error over the integration interval, which is in this case

$$\frac{0.252 \, {}^{cycle}\!/_{s^2}}{(18.87 Hz)^2} = 7.08e^{-4} cycle \, . \tag{5.22}$$

This it is equivalent to slightly more than one quarter of one degree, or 0.255^{o}. This value will be kept in mind when evaluating the estimated capabilities of the estimation approach to determine when it will be of consequence. One must remember that since the estimation process will proceed after a short delay, there will be an existing estimate of platform dynamics that could form the basis of a smoothing strategy to reduce this dynamic contribution further. This suggests that it would be possible to adapt this method to use in a mobile receiver experiencing high dynamics, as long as continuous navigation solutions, or estimates of antenna motion were available.

5.5.5 Estimated Capabilities

In the absence of the influence of any unmodeled effects, the expected performance of this method is dependent on only the number of satellite observables, and their respective carrier to noise ratios.

Across each of the scenarios below it is assumed for simplicity's sake that each satellite in view is received at a common carrier-to-noise ratio and over a common integration period of 10 ms.

If the assumption of minimal dynamic influences is met, as described above, the situation at hand becomes one in which multiple measures of a single quantity are present, each containing independent (due to CDMA or FDMA channel separation) noise influences with a nearly zero mean. According to Kay (1998) when one can express the available data in the form

$$x[n] = R + w[n], \tag{5.23}$$

where x[n] is the nth channel discriminator delta which includes the desired measure of the local oscillator delta (R), as well as w[n], a strong, nearly white noise component, there are multiple approaches for the estimation of R.

The straightforward solution to estimate R in this case is to use the predicted variances of each measure to serve as an inverse weighting to the contribution of each individual term, followed by normalization by the total variance, as expressed by

$$\hat{R} = \frac{\sum_{n=0}^{N-1} \frac{x[n]}{\sigma_n^2}}{\sum_{n=0}^{N-1} \frac{1}{\sigma_n^2}}. \tag{5.24}$$

Now, since it is desired to bound the uncertainty of the estimate of R, the variance of this quantity should also be noted. This uncertainty can be determined as

$$\sigma_R^2 = \frac{1}{N^2} \sum_{n=0}^{N-1} \sigma_n^2 . \tag{5.25}$$

In the case where the variance of all N measurements is equal to σ^2 this simplifies to

$$\sigma_R^2 = \frac{\sigma^2}{N} \tag{5.26}$$

To determine the performance of the estimation method for a given constellation configuration, with specific power levels and available carrier signals, it is necessary to utilize the predicted variances plotted in Figure 5-5 as inputs to equations (5.24) and (5.25). To provide numerical examples of the performance of this method, three scenarios will be discussed spanning the expected range of performance.

In scenario 1 which is intended to be characteristic of that visible to a single frequency GPS user under slight attenuation it is assumed that 12 single frequency satellites are visible at a common C/N_0 of 36 dB-Hz, yielding from the simulation curves a σ_n^2 value

for each channel of 0.0265 rad^2. When substituted into equation 24, this predicts an estimation uncertainty of $\sigma_R = 2.81^o$.

This is a level of estimation uncertainty similar to that assumed to be intrinsic to the local oscillator in the previous section. The implication of this result is that with this minimally powerful set of satellites, it becomes possible to quantify the behaviour of the local oscillator with a level of uncertainty commensurate with the actual uncertainty in the oscillator over the 10 ms averaging interval. Consequentially this indicates that the Allan deviation of this system oscillator could be wholly evaluated under these conditions at any interval of 10 ms or longer. Further, if the system oscillator were in fact the less stable MCXO (Microprocessor Compensated XO) from the resource above, this estimate uncertainty would be significantly lower than the actual uncertainty intrinsic to the oscillator, providing an opportunity to "clean" the velocity measurements.

In scenario 2 which is intended to be characteristic of a near future multi-constellation single frequency receiver it is assumed that eight satellites from three constellations are visible on a single frequency each, with a common C/N$_0$ of 42 dB-Hz, yielding a σ_n^2 value for each channel of 6.4e^{-3} rad^2, leading to an estimation uncertainty of

$\sigma_R = 0.935^o$

In scenario 3 which is intended to serve as an optimistic scenario involving a future multi frequency, multi constellation receiver, it is assumed that nine future satellites are available from each of three constellations, each with four independent carriers, all

received at 45 dB-Hz, yielding a σ_n^2 value for each channel of $3.2e^{-3}$ rad^2, leading to an estimation uncertainty of $\sigma_R = 0.311^o$.

While the implication of the preceding performance estimations is that all of the signals available within a GNSS receiver may be used to estimate the phase noise in the local oscillator, there are certain important receiver design features that may interfere with the combination of measurements from different GNSS carriers.

5.6 Oscillator Noise Considerations During Up and Down Conversion

Since each different GNSS signal band such as L1 and L2 reside far apart in the spectrum they require differing down mixing LO frequencies. While these LO frequencies are generated from the common system oscillator, the generation of each LO frequency involves the use of a frequency synthesizer. Since these frequency synthesizers add to and shape the noise present in the frequency conversion chain, they will cause the phase noise present in the down conversion of different carriers to differ and de-correlate.

The modification and inevitable increase of system oscillator noise during up-conversion from the frequency naturally produced by the system reference, e.g. 10 MHz to the RF frequency needed for down conversion, e.g. 1590 MHz is a consequence of the implementation of a practical frequency synthesizer. This causes the noise at the output of the frequency converter to be partially governed by the input noise, while also being

dependent in part on the configuration choices within the frequency synthesis apparatus. In light of this fact a discussion of the components and noise sources within a frequency synthesizer, in line with that presented by Radio-Electronics.com (2010) will be undertaken.

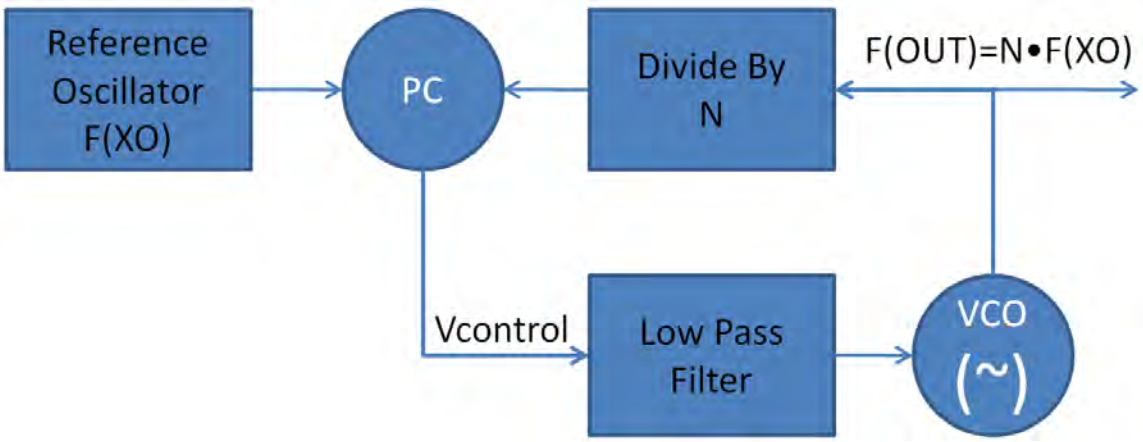

Figure 5-7: Block diagram of a Phase locked loop frequency synthesizer

In Figure 5-7 the individual components of a basic PLL frequency synthesizer are shown based on their interconnection. Before explaining the overall noise characteristics of the composite system, the identity and purpose of each block should be considered:

1) The reference oscillator is the system oscillator, often a quartz crystal.
2) The Phase Comparator (PC) compares the input reference signal to a locally generated signal of the same frequency, increasing or decreasing the value of its output control voltage (Vcontrol) based on whether the phase of the locally generated signal leads or lags that of the input reference.

3) The low pass filter filters the control voltage from the phase comparator to remove noise above its cutoff frequency before passing this signal along to the VCO (Voltage Controlled Oscillator).
4) The VCO produces an output frequency proportional to the value of the filtered control voltage.
5) The divider block creates a signal at 1/N times the output frequency.

To aid the understanding of the overall noise at the output of the frequency synthesizer we assume for the time being that both the frequency divider and phase comparator components operate as ideal functional blocks. Under these assumptions the analysis of the system noise may be expressed in terms of the noise originating from the voltage controlled oscillator, and that originating within the system reference oscillator.

Noise originating in the VCO will propagate through the down converter and directly influence the output of the phase comparator. In turn any portion of the VCO noise at the output of the phase comparator which is below the cutoff frequency of the loop filter will be fed back to the VCO as an error signal, negating this noise. As such the noise of the VCO is effectively high pass filtered before reaching the output. In contrast, noise originating from the system Reference Oscillator will travel through the phase comparator, and pass through the low pass loop filter before being acted upon by the VCO.

Having considered these two noise paths through a simple frequency synthesizer it becomes apparent that the noise at the output of the synthesizer will be dominated by the noise processes in the system oscillator at frequencies up to the loop filter cut off frequency, and by noise intrinsic to the VCO above this point.

This is intuitively correct since the system must be locked to the local oscillator when functioning, allowing short term deviation of the output from the ideal frequency translated input, but over the long term remaining locked to the input.

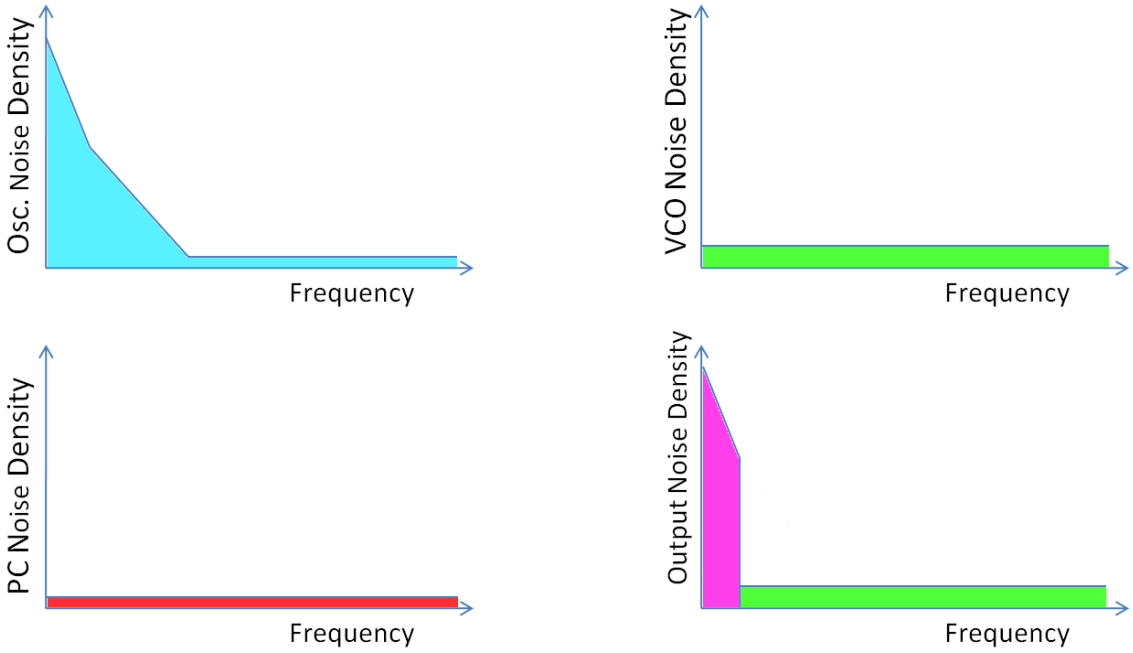

Figure 5-8: Noise spectra of important components within the Frequency Synthesizer signal chain.

If we now consider the effect of noise within the phase comparator, it is obvious that this source of noise will be additive with the noise from the reference oscillator, adding to the output phase noise of the system below the cutoff frequency of the loop filter, but not having an effect above.

As discussed by Kester (2008), and as is shown in Figure 5-8 the composite noise spectra at the output of the synthesizer can be improved in the region of the spectrum between the cutoff frequency of the loop filter, and the region where the noise of the system reference oscillator is greater than that of the voltage controlled oscillator. Above this frequency offset however the noise density at the output of the synthesizer will be greater than that of the input. Since the noise at the output of the frequency synthesizer is effectively low pass filtered by the coherent integration processes within a GNSS receiver, noise above 1kHz will not be of consequence. By extension, in any system where the loop filter bandwidth within the synthesizer is equal to or greater than one kHz, the output noise will be dominated by only the system reference oscillator and the phase comparator.

In conclusion the degree of decorrelation of oscillator noise between the various down converted signals within a multi-band receiver will be dependent on the noise characteristics and bandwidth of the synthesizer phase comparator, as well as the loop filtering bandwidth. In the case of low noise phase comparator driven by a relatively noisy reference such as a TCXO, within a wide loop bandwidth synthesizer, the methods outlined should be able to combine observations from all carriers simultaneously. Since according to Kester (2008) the noise density in a typical phase comparator is quite low relative to the noise densities expected within a typical reference oscillator, this should not pose an obstacle to operation. If however the bandwidth of the synthesizer is lower than the inverse of the coherent integration interval utilized, the noise between different

system channels could de-correlate to a degree that would make this approach un feasible. For a further discussion of the exact relationships between system oscillator and frequency synthesizer phase noise levels, the reader is directed to the following references: Cerda(2006), Jones & Hofner (2010), and Drucker (2000).

Chapter Six: Conclusions and Future Work

6.1 Conclusions

The conclusions of the thesis are divided into two categories to reflect the two primary and novel developments encapsulated by it. The first being the empirical information gained about the auroral and polar behaviour of GPS L1 L2 phase scintillation and other disturbed ionospheric effects. In both auroral and polar scintillation events observed, ranging from universally weak in the case of the polar scintillation, to very strong in the case of some of the auroral events, the optimally detectable physical size was found to be approximately equal, and less than 75 metres. The second set revolves around the presented novel method for very short time scale determination and removal of the phase noise effects of the system oscillator within a GNSS receiver.

The practical usefulness of the developed understanding of the high level of correlation between the effects of the ionosphere between GNSS carriers during both weak and extremely strong, polar and auroral scintillation is expected to derive primarily from its implications for civilian receiver operation. The fact that the events analyzed indicate that direct observation of the ionosphere is possible, even during severe phase scintillation activity by using multiple civilian accessible signals, could be of significant utility to users or future L1 L5 safety of life navigators. Likewise, the observation of synchronization of pulsation effects between L1 and L2 GPS carriers, as well as the proposed method of detection may be of interest to those studying such phenomena,

especially in light of the theoretically determined low false alarm rate of the detection method for even extremely small changes in the ionosphere due to pulsation.

In terms of the development of a method for estimating the very short term instability in the local system oscillator of a GNSS receiver, a straightforward yet novel method of utilizing the existing and future GNSS signals has been created. The ability to estimate on a very short term basis the phase change in the local oscillator with a certainty approaching that of an ovenized quartz reference has strong implications for other fields of receiver development. These are expected to include the ability to utilize the previously discussed short term scintillation detection methods even within very low cost, weight and size consumer GNSS equipment, while also enhancing existing applications that utilize GNSS as a timing reference. While some consideration of the hardware used within the frequency synthesizers of a multi frequency receiver is needed to ensure that the presented approach to local oscillator phase noise estimation is applicable, this obstacle should be relatively easy to overcome. Simply put, it is expected that these findings could have a very broad impact within GNSS receiver development.

6.2 Future Work

The noted presence of apparent correlated carrier activity well beyond the maximum correlation versus noise frequency/feature size in the auroral and polar data, should be further examined to ascertain the true de-correlation frequency/physical displacement distance at which L1 to L2 GPS phase scintillation de-correlation occurs.

Further polar scintillation data of a higher intensity is desired to determine if the near total carrier phase scintillation correlation effects observed at latitudes beneath the auroral oval for vigorous phase scintillation also hold true at higher latitudes.

The capture of moderate and high magnitude phase scintillation events implies that further data collections should be executed, but also that they should be conducted when the probability of observing events of significant magnitude is elevated. The currently available data was collected during a deep nadir of activity, as the solar activity data presented in Chapter 2 confirms. Since it is impossible to observe that which is not currently occurring, it comes as little surprise that strong scintillation activity was not captured during the latter 2008 polar collection efforts. This should be addressed simply by conducting data collections later in the current solar cycle.

The analysis of high latitude fading events and their observation with multi carrier GNSS signals was intended to be carried out as a component of this thesis, however due to the lack of observation of clearly identifiable fading (verified to be free from multipath effects) activity this was not possible. Due to this omission, it is intended that a portion of the future effort of the author would be directed to the study of this phenomena, which would be facilitated by further data collection.

Attention should also be given to the GNSS network used to collect multi-frequency scintillation data from satellites above 30 degrees elevation, to ensure that the

characteristics of the network or networks used for further observation are likely to capture the desired events. From the point of view of simple observability and distribution across the sky, multi frequency GPS satellites are somewhat less likely to provide observations of scintillation than those of GLONASS.

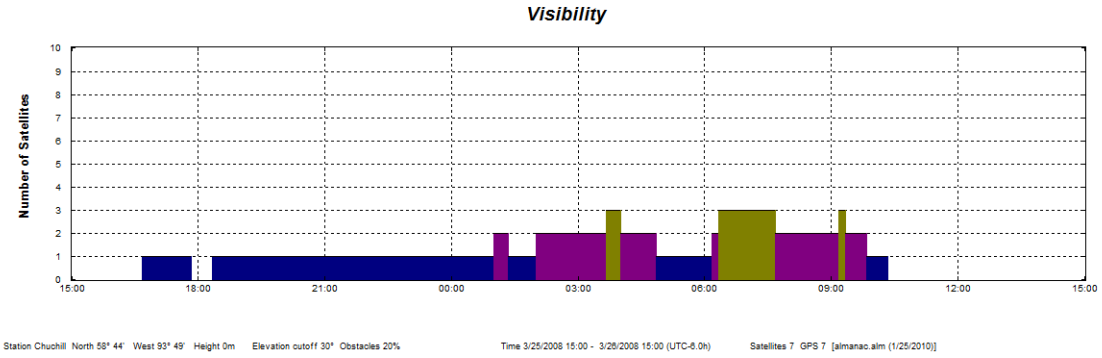

Figure 6-1: Dual frequency GPS satellite visibility from Churchill Northern Studies Centre above 30 degrees elevation, based on current ephemeris data.

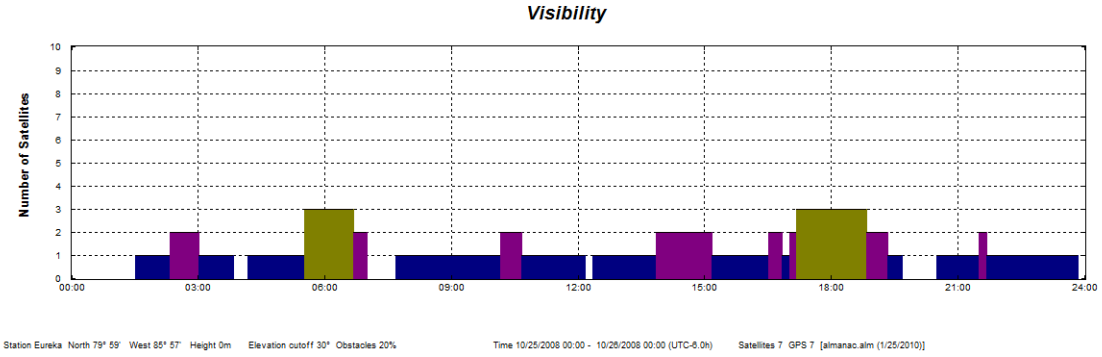

Figure 6-2: Dual frequency GPS satellite visibility from Eureka weather station above 30 degrees elevation, based on current ephemeris data.

Subjectively evaluating the visibility of useable GPS Block IIR-M satellites during the Churchill and Eureka data gathering efforts shown in Figure 6-1 and Figure 6-2, it becomes clear that the probability of observing a scintillation event is highly constrained by the limited number of GPS dual frequency satellites. In both situations, but

particularly in the case of Churchill there were large outage periods when observation of scintillation events on a dual frequency satellite above 30^{o} was simply impossible.

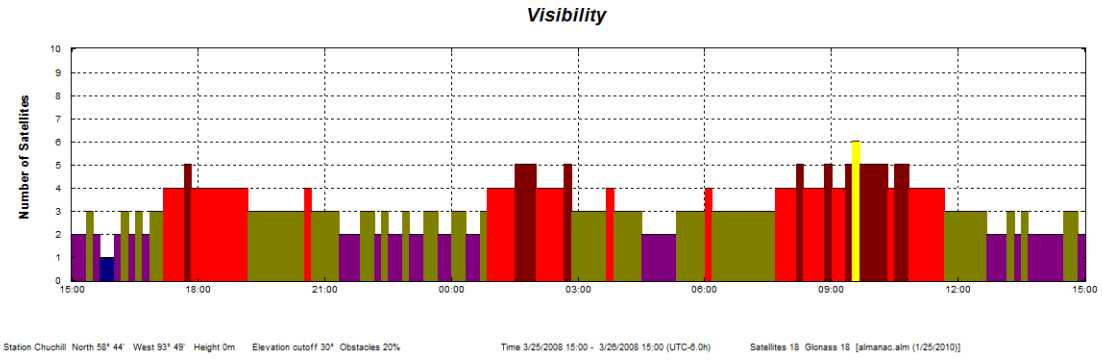

Figure 6-3: Dual frequency GLONASS satellite visibility from Churchill Northern Studies Centre above 30 degrees elevation, based on current ephemeris data.

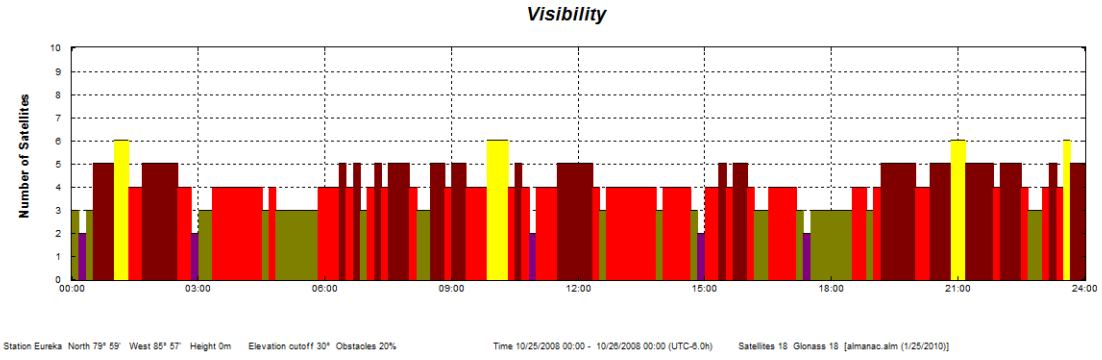

Figure 6-4: Dual frequency GLONASS satellite visibility from Eureka weather station above 30 degrees elevation, based on current ephemeris data.

Comparing the availability of GLONASS at the same locations with the same elevation constraints shown in Figure 6-3 and Figure 6-4 to the availability of GPS it is obvious that the collection of dual frequency GNSS scintillation observations will have a much higher rate of observability when utilizing GLONASS than when utilizing GPS. This disparity is expected to continue through much of 2010 due to the continued delays in the launch of GPS Block II-F satellites, as well as the continued rapid replenishment of the

GLONASS constellation with URAGAN-M vehicles. In 2010 one Block II-F satellite is expected to launch, while a total of 8 URAGAN-M and 1 URAGAN-K will be deployed.

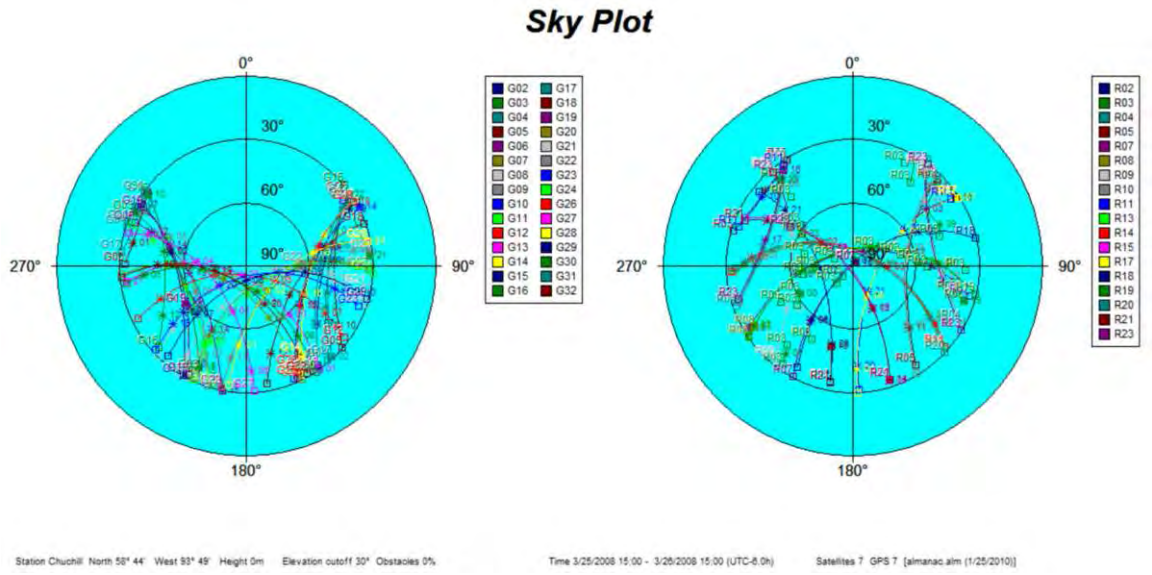

Figure 6-5: Sky coverage maps from Churchill northern studies centre above 30 degrees elevation over 24 hours. GPS coverage is plotted on the left, GLONASS coverage is plotted on the right. Note that while all GPS satellite paths are plotted, only modernized GLONASS satellite overpass trajectories are shown.

An additional factor highlighting the need to plan to use an additional GNSS in addition to GPS for future data collection is the sky coverage in high latitude areas. Taking the example shown in Figure 6-5 that compares the sky coverage between GPS (all satellites) and GLONASS (dual frequency satellites) over a 24 hour period, it is clear that a large portion of the sky is simply not covered by GPS. This limitation will be shared by COMPASS satellites due to both systems utilizing a lower orbital inclination angle than that of GLONASS and Galileo. The plot has been generated with all GPS satellite trajectories shown rather than only those of dual frequency satellites to eliminate any misconception as to the cause of the large coverage gap. The gap is not due to the

currently limited number of modernized GPS satellites, it is simply a consequence of the system orbit configuration, and cannot be eliminated through future satellite launches. Collection of stronger scintillation events near the solar cycle maxima must therefore be planned to include GLONASS.

In addition to the planned future work surrounding field data collection, and subsequent theoretical analysis of moderate to strong high latitude scintillation, future work in terms of system development is also planned. Due to the enormous advantages presented to scintillation study by the inclusion of GLONASS into the pool of observable satellites, the development of a lightweight, portable GPS+GLONASS dual frequency front-end will be completed. As of the publication of this thesis the state of development of this front-end is detailed in Appendix A, and while not yet completed, this front-end is designed to figure prominently in future ionospheric scintillation study efforts.

References

ASC (2010), *ACE Level 2 (Verified) Data*, http://www.srl.caltech.edu/ACE/ASC/level2/index.html, last accessed 2 June 2010.

Béniguel, Y., B., Forte, S. M., Radicella, H. J., Strangeways, V. E., Gherm and N. N. Zernov (2004) "Scintillations Effects on Satellite to Earth Links for Telecommunication and Navigation Purposes", Annals of Geophysics, Supplement to Vol. 47, pp. 1179-99.

Beta LAYOUT Ltd. (2009) *Layerbuild for 4-Layer Mutilayer*, available at http://www.pcb-pool.com/download/spezifikation/eng_cmso004_ml4.pdf Last retrieved 5 July 2010.

Boeing Corporation (2005) *Delta II Block IIR-14 Media Kit*, No report number given, Boeing, 29 pages

Borio, D. and O'Driscoll, C. (2007) Personal Communication.

Cerda, R.M. (2006), *Impact of ultralow phase noise oscillators on system performance*, rfdesign.com Time and Frequency technical report, 4 pages.

Chastellain, F., C. Botteron, and P.A. Farine (2005), "A Low-Power RF Front-End Architecture for an L1/L2CS GPS Receiver," in *Proceedings of ION GNSS 18th International Technical Meeting of the Satellite Division*, 13-16 September, Long Beach CA, pp. 628-634, U.S. Institute of Navigation, Fairfax VA

CIT (1998) *ACE Satellite Now In Place Between Earth and Sun; Will Seek To Determine What Sun Is Made Of*, California Institude of Technology, Published 3 February 1998, available at http://media.caltech.edu/press_releases/11853

Clynch, J.R. (2001) "Ionospheric Bending of Radio Signals: A rough, Shell Model Approximation", pubished as part of Professor Clynch's collection of technical notes available at http://clynchg3c.com/Technote/Tnotes.htm, Last accessed June 8 2010

Conker, R.S., M. B. El-Arini, C.J. Hegarty, and T.Y. Hsiao (2000), *Modeling the Effects of Ionospheric Scintillation on GPS/SBAS Availability*, Mitre Product No. MP 00W0000179, The MITRE Corporation, 63 pages

Conley, R., Cosentino, R., Hegarty, C. J., Kaplan, E. D., Leva, J. L., Uijt de Haag, M. and K. V. Dyke (2006) "Performance of Stand-Alone GPS," [Chapter 7] in *Understanding GPS Principles and applications, 2nd Ed*, E.D. Kaplan and J. Hegarty, ed., Artech House Publishers, Boston MA, p. 312

Cosentino, R. J., Diggle, D.W., Hegarty, C. J., Milbert, D. and J. Nagle (2006) "Differential GPS," [Chapter 8] in *Understanding GPS Principles and applications, 2nd Ed*, E.D. Kaplan and J. Hegarty, ed., Artech House Publishers, Boston MA, p. 440

Datta-Barua, S., Doherty, P.H., Delay, S.H. and T. Dehel (2003), "Ionospheric Scintillation Effects on Single and Dual Frequency GPS Positioning," in *Proceedings of ION GPS 2003,* 9-12 September, Portland OR

Drucker, E. (2000) "Model PLL Dynamics and Phase-Noise Performance," *Microwaves & RF*, February 2000, pp.73-117

Forssell, B. (2003) *Radionavigation Systems*, Kompendieforlaget, Nardoveien 14, 7005 Trondheim, pp. 48-52

Foster, J., C. and W. Rideout (2007) "Storm enhanced density: magnetic conjugacy effects", Ann. Geophys, Vol. 25, pp. 1791-1799.

Grillenberger, A., R. Rivas, M. Markgraf, P. Mumford, K. Parkinson, and C. Rizos (2008) *The NAMURU Receiver as development platform for spaceborne GNSS applications*, Navitech Report

Garvey, M. (2004) Public comments following presentation of "Comparative Analysis of GPS Clock Performance Using both Code-Phase and Carrier-Derived Pseudorange Observations" *36th Annual Precise Time and Time Interval (PTTI) Meeting*, December 7-9 2004, Washington D.C.

Gaussiran, T., D. Munton, B. Harris, and B. Tolman (2004) "An Open Source Toolkit for GPS Processing, Total Electron Content Effects, Measurement and Modeling," *International Beacon Satellite Symposium 2004*, Trieste Italy October 2004.

Hathaway, D. H. (2007) *NASA/Marshall Solar Physics: The Solar Wind* http://solarscience.msfc.nasa.gov/SolarWind.shtml, last accessed 19 July (2010)

Hinks, J.C., T.E. Humphreys, B. O'Hanlon, M.L. Psiaki, and P.M. Kintner Jr. (2008) "Evaluating GPS Receiver Robustness to Ionospheric Scintillation," in *Proceedings of ION GNSS 21st International Technical Meeting of the Satellite Division*, 16-19 September, Savannah GA, pp. 309-320 U.S. Institute of Navigation, Manassas VA.

Humphreys, T.E., B.M. Ledvina, M.L. Psiaki, and P.M. Kintner, Jr. (2004) "Analysis of Ionospheric Scintillations using Wideband GPS L1 C/A Signal Data," in *Proceedings of ION GPS 2004*, 21-24 September, Long Beach California

IEEE 1139/D3 Annex C (2008). Definitions of Physical Quantities for Fundamental Frequency and Time Metrology – Random Instabilities.

Irons, B. (2008) *Extended Characterization for the MAX2112/MAX2120 Satellite Tuners*, Application Note #4256, Maxim IC Corporation, 13 pages

IS-GPS-200D (2004), *Interface Control Document – Navstar GPS Space Segment / User Segment Requirements*, ARINC Incorporated, December 2004.

JHUAPL (2000), *UPOS: SCINDA*, http://sd-www.jhuapl.edu/UPOS/SCINDA/index.html , last accessed 12 July 2010.

Johansson, S. (2008), *Modern frequency counting principles*, Pendulum Instruments AB, Sweden, Page 27. Retrieved from resource.npl.co.uk/docs/networks/time/meeting5/ johansson.pdf

Jones, P. and T. Hofner (2010) *Design Challenges for an Ultra-Low-Jitter Clock Synthesizer*, Application Note 4336, Maxim Corporation, 8 pages

JPO (2004) *Navstar GPS Space Segment/Navigation User Interfaces*, IS-GPS-200 Revision D, GPS Joint Program Office 207 Pages.

Kay, S.M. (1998) *Fundamentals of Statistical Signal Processing, Volume I Estimation Theory*, Prentice Hall, Upper Saddle River, New Jersey 07458, pp. 244

Kay, S.M. (1998b) *Fundamentals of Statistical Signal Processing, Volume II Detection Theory*, Prentice Hall, Upper Saddle River, New Jersey 07458, pp. 74

Kazemi, P.L. (2010) Development of New Filter and Tracking Schemes for Weak GPS Signal Tracking, PhD Thesis, Department of Geomatics Engineering, University of Calgary, Canada, pp. 6 (Available at http://plan.geomatics.ucalgary.ca)

Kester, W. (2008) *Converting Oscillator Phase Noise to Time Jitter*, Tutorial MT-008, Analog Devices, 10 pages.

Leapsecond (2008), Oscillator Stability Comparison. Retrieved from http://www.leapsecond.com/museum/manyadev.gif, last accessed July-2009

Lipko, Y.V., A.Y. Pasinin, and R.A. Rakhmatulin (2001) "Ionospheric Manifestations of Geomagnetic Pulsations at High Latitudes," Institute of Solar-Terrestrial Physics SD RAS.

Lombardi (2008a), *Fundamentals of Time and Frequency*, Chapter 17.1. Retrieved from tf.nist.gov/timefreq/general/pdf/ 1498.pdf

Lombardi, M. (2008b), *General Concepts of Time and Frequency Metrology.* Retrieved From http://tf.nist.gov/sim/2008_Seminar/ SIM_2008_General_Concepts_Lombardi .ppt

Menk, F.W., T.K. Yeoman, D.M. Wright, M. Lester, and F. Honary (2003) "High-latitude observations of impulse-driven ULF pulsations in the ionosphere and on the ground," in *Annales Geophysicae*, vol 21, pp. 559-576

Moraes, A. O. and W.J. Parrella (2009) "Performance evaluation of GPS receiver under equatorial scintillation", Journal of Aerospace Technology and Management, Vol. 1, number 2, pp. 193-200.

Morrison (2009), Accurate Millisecond Level Oscillator Phase Noise Estimation for Standalone GNSS, Proceedings ION GNSS 2009 Session F6b, Savannah, GA., September 22-25 2009

NAROM (2010) "Jordens permanente magnetfelt," [chapter 7] in Fysikk, Nasjonalt Senter For Romrelatert Opplæring Publishers, Revidert NO, section 7.8, Figure 7.14.

NASA (2008) *What's Wrong with the Sun? (Nothing)*, http://science.nasa.gov/headlines/y2008/11jul_solarcycleupdate.htm, last updated 11-July-2008, last accessed Jan-2010

Natural Resources Canada (2009) *Geomagnetism – Plotting Service*, http://geomag.nrcan.gc.ca/common_apps/mp-eng.php , last updated September 23, 2009

NIST (2010) *Time and Frequency from A to Z*, http://tf.nist.gov/general/glossary.htm, last accessed Feb-2010

NOAA/NESDIS/NGDC/STP, Boulder – Solar Data Services (2010), http://www.ngdc.noaa.gov/nndc/struts/results?op_0=eq&v_0=Interplanetary_Magnetic_Field&t=102827&s=29&d=8&d=290&d=9, last accessed 25 April 2010.

NOAA (2009) *Solar Cycle 24 Prediction Updated May 2009*, http://www.swpc.noaa.gov/SolarCycle/SC24/index.html, last updated 8-May-2009, last accessed January 9 2010

Novatel (2010) *GPS-702L Antennas: Dual Frequency Antenna Delivers Excellent Performance, Multipath Rejection and L-band Functionality*, www.novatel.com/assets/Documents/Papers/GPS-702L.pdf, last accessed 25 May 2010.

NovAtel (2000) *GPSCard^{TM} OCXO, MiLLennium^{R} Cesium or Rubidium Options Should you be using one in your applications?*, APN-002 Rev 1, NovAtel, 5 Pages.

O'Hanlon, B., M.L. Psiaki, S.P. Powell, and P.M. Kintner Jr. (2010) *Carrier-Phase Anomalies Detected on SVN-48*, http://www.gpsworld.com/gnss-system/gps-modernization/news/carrier-phase-anomalies-detected-svn-48-9946, Published 17 May 2010.

Olynik, M., M.G., Petovello, M.G., Cannon and G. Lachapelle (2002), "Temporal Variability of GPS Error Sources and Their Effect on Relative Positioning Accuracy" in *GPS Soluations, John Wiley & Sons Inc.*, vol 6, no 1-2, pp. 47 - 57

Posch, J.L., M.J. Engebretson, S.B. Mende, H.U. Frey, R.L. Arnoldy, M.R. Lessard, L.J. Lanzerotti, J. Watermann, M.B. Moldwin, and P.V. Ponomarenko, (2006) "Using Pi1 Pulsations to Improve Spatial Identification of Substorm Onsets" submitted to the Journal of Geophysical Research March 2, 2006.

Psiaki M.L. (2007) *Collection, Analysis, and Modeling of GPS Scintillation Data from Equatorial Regions*, The University of Calgary Department of Geomatics International Lecture Series and ION Alberta Section Presentation.

Psiaki, M.L., Humphreys, T.E., Cerruti, A.P., Powell, S.P., and P.M. Kintner (2007), "Tracking L1 C/A and L2C Signals through Ionospheric Scintillations" in *Proceedings of the ION GNSS 2007* 25-28 September, Fort Worth, TX. Pp 246-268.

Pullen, S., Opshaug, G., Hansen, A., Walter, T., Enge, P.and B. Parkinson, B., "A preliminary study of the effect of ionospheric scintillation on WAAS user availability in equatorial regions," in *Proceedings of the ION GPS 1998,*15-18 September, 1998, Alexandria, VA. Pp. 687-699

Radio-Electronis.com (2010) *low phase noise synthesizer design*, www.radio-electronics.com/info/rf-technology-design/pll-synthesizers/frequency-synthesiser-tutorial-basics.php, last accessed 6 March 2010.

Raquet, J.F. (2006) *Advanced GNSS Receiver Technology*, ENGO 699.45 Course Notes, Department of Geomatics Engineering, University of Calgary, Canada, pp. 75-77

Raquet, J.F. (2006b) *Advanced GNSS Receiver Technology*, ENGO 699.45 Course Notes, Department of Geomatics Engineering, University of Calgary, Canada, pp. 63-65

Revnivykh et al (2005), *Status and Development of Glonass*. Presented to the European Navigation Conference, Munich, 19-22 July. slide 15. Retrieved from - http://www.mcc.rsa.ru/IACKVO/RUS/News/Status and Development of GLONASS.pdf

RF-Cafe (2009) *Cascaded Noise Figure compact form*, http://www.rfcafe.com/references/electrical/noise-figure.htm, last accessed January 23, 2010

RISDE (2008) *Global Navigation Satellite System GLONASS Interface Control Document Navigation radiosignal in bands L1,L2*, Edition 5.1, Russian Institute of Space Device Engineering

Rodrigues, F.S., M.H.O. Aquino, A. Dodson, T. Moore, and S. Waugh, (2004) "Statistical Analysis of GPS Ionospheric Scintillation and Short-Time TEC Variations

over Northern Europe," in *NAVIGATION: Journal of The Institute of Navigation*, vol 51, no 1, Spring, pp. 59 - 75

Skone, S.H. (2010) *Ionospheric Refraction FINAL*, ENGO633 Course Notes, Department of geomatics Engineering, University of Calgary, Canada, pp. 33

Skone, S.H. (2010b) *Ionospheric Phenomena and Indices*, ENGO633 Course Notes, Department of geomatics Engineering, University of Calgary, Canada, page. 5

Skone, S.H. (2010c) *Special Topics Pulsations final*, ENGO633 Course Notes, Department of geomatics Engineering, University of Calgary, Canada, page. 9

Skone, S. (2007) *Atmospheric Effects on Satellite Navigation Systems*, ENGO 633 Course Notes: Ionosphere Phenomena and Indices, Department of Geomatics Engineering, University of Calgary, Canada, pp. 5-17

Skone, S. (2007a) *Atmospheric Effects on Satellite Navigation Systems*, ENGO 633 Course Notes: Observation of Geomagnetic Pulsations Using GPS, Department of Geomatics Engineering, University of Calgary, Canada, pp. 1-18

Skone, S.H., and K. Knudsen (2000) "Impact of Ionospheric Scintillations on SBAS Performance," in *Proceedings of the ION GPS 2000*, 19-22 September, Salt Lake City UT

Skone, S.H., G. Lachapelle, D. Yao, W. Yu and R. Watson (2005) "Investigating the Impact of Ionospheric Scintillation using a GPS software Receiver," in *Proceedings of the ION GNSS 2005*, 13-16 September, Long Beach CA.

Space Weather Prediction Centre (2010) *Statistical Auroral Oval Extrapolated from NOAA-19*, http://www.swpc.noaa.gov/pmap/gif/pmapN.gif, last accessed 11 March 2010.

SpaceWeather.com (2008), *Spaceweather.com Time Machine 10 October 2008*, http://www.spaceweather.com/archive.php?view=1&day=10&month=10&year=2008, last accessed 10 July (2010)

SpaceWeather.com (2008a), *Spaceweather.com Time Machine 11 October 2008*, http://www.spaceweather.com/archive.php?view=1&day=10&month=10&year=2008, last accessed 10 July (2010)

SWPC (2010) *Explanation of Real-Time Solar Wind data dials*, http://www.swpc.noaa.gov/SWN/sw_dials.html Last updated 18 July 2010.

Ullman (1999) "What is HDF-EOS?," *HDF-EOS Workshop III, 1999*, Landover, Maryland September 14-16, 1999.

Van Dierendonck, A.J. (1999) "Eye on the Ionosphere: Measuring Ionospheric Scintillation Effects from GPS Signals," GPS Solutions, Vol. 2, number 4, pp. 60-63.

Van Dierendonck, A.J., J. Klobuchar, and Q. Hua (1993) "Ionospheric Scintillation Monitoring Using Commercial Single Frequency C/A Code Receivers*," *Proceedings of the ION GPS-93*, Salt Lake City, Utah, 22-24 September, 1993.

Van Dierendonck, A.J., and Q. Hua (2001) "Measuring Ionospheric Scintillation Effects from GPS Signals," in *Proceedings of ION 57th Annual Meeting/CIGTF 20th Biennial Guidance Test Symposium*, 11-13 June, Albuquerque, NM, pp. 391-396

Victorkosenko, V., and V. Chebotarev (2006) "Russian GLONASS at the Stage of Active Implementation," *Inside GNSS*, Technical Article Builders Notes, April 2006

Vig, J (2004a) *Quartz Crystal Resonators and Oscillators For Frequency Control and Timing Applications – A Tutorial*, Rev. 8.5.2.0, p 4-25

Vig, J (2004b) *Quartz Crystal Resonators and Oscillators For Frequency Control and Timing Applications – A Tutorial*, Rev. 8.5.2.0, p 7-1

Wang, Z., Y. Wu, K. Zhang, and Y. Meng (2005) "Triple-Frequency Method for High-Order Ionospheric Refractive Error Modelling in GPS Modernization," in *Journal of Global Positioning Systems*, vol 4, No.1-2, pp. 291-295

Ward, P.W., J.W. Betz and C.J. Hegarty (2006) Satellite Signal Acquisition, Tracking, and Data Demodulation, Understanding GPS Principles and Applications, E. D. Kaplan and C.J. Hegarty, Norwood, MA, Artech House, Inc., pp 153-241

Yu, W. (2007) Selected GPS Receiver Enhancements for Weak Signal Acquisition and Tracking, MSc Thesis, Department of Geomatics Engineering, University of Calgary, Canada, pp. 69 (Available at http://plan.geomatics.ucalgary.ca)

Yu W., G. Lachapelle, and S. Skone (2006), "PLL Performance for Signals in the Presence of Thermal Noise, Phase Noise, and Ionospheric Scintillation" in *Proceedings of ION GNSS 19th International Technical Meeting*, 26-29 September, Fort Worth, TX

APPENDIX A: FRONT-END DESIGN & IMPLEMENTATION

A.1. Design motivation and objectives

When approaching a combined hardware, firmware, and software design project such as a high performance Front-End it is critical to ensure that the desired features of the design are firmly set from the very inception of the project. Failure to judiciously set a constrained number of specific goals will often result in a failure to satisfy any objectives.

With this fact of design under consideration, the primary functional goals of the front-end were set as follows:

1) The front-end must have a tuneable centre frequency between the limits of the currently known L-band navigation signals, with L5/E5a (1176.45 MHz) at the low end and GLONASS L1 (1602 MHz) at the high end. To allow optimal setting of centre frequencies to capture as many signals as possible, the granularity of the centre frequency selection should be smaller than 5 MHz increments.
2) To provide coverage of the most heavily populated spectral bands, the combination of usable bandwidth per channel and number of channels must provide coverage of GPS and GLONASS L1 and L2 simultaneously.

3) To support field logging, the front-end should be capable of utilizing either a passive or an active GNSS antenna. This implies that the front-end must possess a suitable LNA drive circuit at the sensitive RF connection point.
4) To provide maximum compatibility, the front-end should pass all data over a standard USB 2.0 connection.

With these primary design goals established as above, a set of secondary functional goals were considered. These goals were to be approached only as targets of opportunity, if their implementation would cause negligible disruption to the design to date, or would require no physical alteration of the system. The selected secondary design goals were as follows:

1) To assist other researchers within and associated with the PLAN group, the front-end should be capable of operating tuning to the CDMA cellular phone bands used in Calgary (1947.5 MHz).
2) To facilitate testing of oscillator effects within GNSS receivers the front-end should be capable of utilizing an externally applied oscillator as the timing standard.
3) To facilitate the integration of inertial navigation equipment with software receivers, the front-end should produce a PPS (pulse per second) signal for the syntonization of external sensors.
4) To allow ease of field use, the front-end should be powered entirely by the aforementioned USB connection with no need for external power supplies or

batteries. This implies a 2.5 W power limit on the system as the USB2.0 specification limits maximum bus current to 500 mA, with a supply voltage of 5 V.

5) To aid in pedestrian data collection applications, the front-end should be physically compact, and lightweight.

A.2. Architectural Decisions

The desired capabilities outlined above can in theory be arrived at by multiple independent approaches, making it necessary to understand the benefits and drawbacks of each. This decision was necessary in three distinct cases in the early development process of the front-end. Firstly a decision had to be reached as to whether to use an integrated down-converter digitizer combination such as the Maxim MAX2769 or Atmel ATR0601 both of which provide down conversion, filtering and digitization in one package, or to use discrete RF mixing, filtering, and ADC sampling hardware spanning two or more ICs. Secondly, a determination as to the RF band selection methodology was needed to distinguish between using multi-stage conversion, single-stage conversion, and which frequency range to use for baseband or under-sampling. Thirdly, while there are relatively few differences between the various vendor options for USB interface ICs, selection of a vendor and definition of the interface to this IC was still required before board design could begin.

An additional design complication arises from the fact that each of the above critical decision categories is to a certain extent related to each of the others. For example, the

selection of an integrated solution for the RF chain would greatly simplify design, but in many cases limits the usable bandwidth of the system significantly, or requires complicated up/down conversion mixing techniques in the preceding stages. It must be noted that for this reason none of the design parameters are truly independent from the others.

A.3. Integrated Down-converter or discrete components

The selection between Integrated Down-converters and discrete components is primarily a trade off between ease of implementation and flexibility of features in the final design. In many cases for example, self contained RF down-converters with filtering and digitization are restricted to a single bit of quantization, or have extremely limited options for bandwidth and sample rate. The aforementioned MAX2769 IC for example advertises a flexible frequency range between 1570 and 1590 MHz centre frequency, but while it claims to be a GPS/GLONASS front-end IC it makes no mention of exactly how it can receive the GLONASS FDMA signals. This is an apparent contradiction since the GLONASS signals reside at 1602 MHz within an 8 MHz band of spectra, indicating that this front-end may not even be able to receive GLONASS despite its claims. In order to use such a device within a GPS+GLONASS capable front-end it would be necessary to resort to a scheme of pre-mixing the incoming signal. This would involve mixing the received signals of interest up or down to ensure they fall within the usable range of frequencies for the given IC. While complicated, this method is successfully used by some pre existing receivers, such as the NAMURU II receiver from the University of New South Wales discussed by Grillenberger et al (2008). Through the employment of

this approach these researchers have been able to map signals of interest such as L2C into the L1 band at the input of the converter IC, such that it is digitized as an L1 signal normally would be. However in addition to the added physical and electrical complexity of this approach, the added RF conversion stages introduce far more inter-channel bias and add phase noise as compared to a simpler implementation.

Clearly, what is desired is the simplicity of the integrated solutions, but with the flexibility of the adjustable discrete components. For this reason, after an extensive search, it was decided to attempt to utilize a DVB-S or DVB-S2 satellite tuner IC, which includes many of the desired features previously mentioned including wide tuning range, adjustable bandwidths and gain, range of input reference frequencies, as well as good support from the manufacturer. Due to the very fine-grained frequency selection options available in the MAX2112, this IC was initially selected as a basis for the design. Regrettably tuning ICs used for DVB applications have noise figures many times higher than those marketed towards GNSS applications, as well as the tendency to have their input impedance matched to the 75 ohm standard used in most television applications, as opposed to the 50 ohm matching in GNSS equipment. Both of these limitations can be overcome by careful design choices, as will be discussed later.

A.4. RF Band Selection and Down Conversion Methodology

Having chosen to utilize a solution based on the MAX2112 DVB-S2 IC, the band selection methodology was implicitly decided, and fortuitously quite straight forward. Specifically the MAX2112 provides for the adjustable division, and subsequent

multiplication of the input frequency standard in order to produce the down-conversion tone used to mix a given signal to baseband. In addition to this integer multiplication and division method, the MAX2112 also included support for a fractional-N PLL operating mode, in which the reference tone could be multiplied by a non-integer value, allowing for very fine grained frequency of interest selection. Unfortunately as this method of frequency generation introduces further phase noise, as well as constraining the range of valid input frequencies in this mode of operation. Due to these shortcomings of the MAX2112, an integer-N only PLL version of the IC known as the MAX2120 was adopted to replace the MAX2112 starting in Revision B of the front-end design, and carried forward from this point.

A.5. Digital Sampling Strategy

Generation of the digitized baseband signal from the product of the RF down conversion section of the front-end requires the use of an ADC, which may be operated in one of at least two modes. In the first of these two modes, referred to as direct or baseband sampling, the signal of interest is present between DC and the Nyquist frequency of the ADC at a given sampling rate. In this mode of conversion the bandwidth requirements of the ADC are relatively low by current technology standards, and the necessity to pre-filter the signal of interest is minimized. In the second of the two modes of digitization, which is referred to as under or IF sampling, the signal of interest is present above the Nyquist frequency of the ADC. This second mode of operation takes advantage of the aliasing caused by sampling a signal, and while it has the advantage of allowing the signal of interest to exist in a higher frequency band, away from where noise from the

digital circuitry of the front-end which can corrupt it, the approach suffers the drawback of requiring much higher bandwidth in both the selected analog to digital converter, as well as the RF down conversion section (Chastellain et al 2005). A further requirement for IF sampling implementations is the need for an effective band-pass filter to allow only the specific Nyquist region of interest to reach the inputs of the ADC, while attenuating both the higher and lower zones.

Due to the limitation of baseband filter bandwidth in the previously selected MAX2112 (and MAX2120) of 40 MHz, it is unlikely that an IF sampling strategy would result in significant separation between occupied signal bandwidth and any spurious signals from local circuitry, while requiring significant additional filtering circuitry. For these reasons, an ADC suited to the output format of the MAX2112 (and 2120) was selected, with additional ADC bandwidth selected as only a minor objective.

The MAX1181/1182/1183 series of dual differential ADC products was selected to match the differential I/Q outputs of the MAX2112 (and 2120) down-converters. These ADCs provide a compatible reference signal range, sampling rates higher than those required by the MAX2112 (or 2120), and an electrical interface well matched to the down-converters. Because of these similarities, the use of these ADCs requires only an additional discrete baseband filter to prevent unwanted noise infiltration.

A.6. USB Interface Implementation

During the initial design phases of the project, three alternatives were available for providing a conduit for the passage of data between the outputs of the ADC and a high speed USB 2.0 connection to a PC. The first of these involved the use of an FPGA to directly implement a USB interface while also connecting to the ADC outputs. While this could potentially be the most compact and lowest cost implementation (if later migrated to an ASIC) it was deemed as not feasible due to the large amount of implementation effort that would be needed to create a USB compatible interface, or due to the large cost of buying the appropriate IP cores to achieve this objective. For these reasons it was decided to employ an existing ASIC from a 3rd party manufacturer, of which two were found to be appropriately matched to the application.

The two ASIC USB interface solutions under consideration were the Cypress Semiconductor FX2, and the FTDI FT2232H, with both sharing many common and desirable features. The first and most essential of these desirable features is the advertised capability to sustain high rates of data transfer, in excess of 20 MB per second. This minimum transfer rate is needed to provide at least 80 MHz of aggregate signal spectrum between the two front-ends with 1-bit quantization. The only alternate requirement for the USB interface IC is that the required cost in money and time of development tools, software, test equipment, and custom firmware needed to evaluate the functionality of the interface should be reasonable. Unfortunately, the expense of equipment and software necessary to program and test an FX2 based solution would be an order of magnitude higher than one using the FT2232H.

A.7. Physical Implementation Considerations

Number of Channels

The ideal solution from the point of view of physical implementation is the simplest, lowest part count option available. Additionally, a simpler implementation usually conserves PCB area, helping to minimize cost of production. One obvious trade off between design complexity and functionality lay in the relationship between the bandwidths of the signals of interest, which number of front-ends would be utilized to capture them, and how much spectral and therefore USB bandwidth, power, and data storage space waste would occur as a consequence. An additional constraint exists in the implementation complexity of multiple front-end channels requiring more than eight aggregate bits of data per sample, due to the need to then insert synchronization pattern generation into the data stream to avoid byte-wise ambiguity in terms of which bits compose which samples. As an example an ensemble of four front-ends, each producing 1-bit I/Q samples would produce one byte of combined data per sample period. If the sampling resolution were increased to two bits, the aggregate data rate would rise to 16 bits per sample period, requiring the generation of a synchronization pattern prefixing any transmitted data from the front-end to remove the byte level ambiguity. A consequent complication of this approach includes the requirement that any decoder or software receiver used with this data stream includes code for identifying and synchronizing with this generated pattern.

As the primary signals of interest were the L1 and L2 bands of both GPS and GLONASS, as well as compatibility with future Galileo and Compass (emerging Chinese GNSS

system) where possible, two approaches to division of the spectra of interest were deemed reasonable. The first of these approaches was the utilization of four front-ends to capture each band individually, at a minimal data rate required for each band; the second approach was the use of two front-ends to capture the L1 signals of both networks in one channel, and the L2 signals of both networks in the other.

In the first implementation, four independent down-conversion channels and four independent ADC modules would be needed to realize the design. The bandwidth usage in this mode of implementation would range between 40-60 MHz of spectrum divided evenly between the front-ends, depending on the desire to utilize the GLONASS P-Code on L1 and L2. This amount of desire spectral capture capability would require between 80-120 Mbit per second of bandwidth over the USB interface for 1-bit quantization, or 160-240 Mbit for 2-bit quantization. Since the parameter of USB bandwidth has already been set above but close to 20 MByte per second, this implementation method is viable for 1 or 2 bit quantization with bandwidths of 10 MHz per channel.

In the second implementation, two down-convert and ADC chains would be required. The bandwidth usage in this mode of operation would be a minimum of 40 MHz of spectrum per channel, for an aggregate 80 MHz of spectrum, requiring 160 Mbit per second of transfer capacity for 1-bit quantization. This mode of spectral division would therefore only function in 1-bit quantization mode when providing GPS+GLONASS.

Despite the identified shortcomings of the latter implementation mode, it was selected to minimize the physical and implementation complexity of the front-end during early design stages, with the possibility of switching to 4 channel design considered only once acceptable results are achieved in the simpler and faster to adapt 2 channel version.

A.8. Printed Circuit Board Characteristics

The selection of printed circuit board characteristics has many implications for other design parameters, including but not limited to physical size, cost, ease of component layout, and in some cases, signal integrity/performance.

The first PCB characteristic over which a designer has control is that of the material used within the substrate between the metal layers. This parameter is most important for RF designs, as the substrate material determines the dielectric constant of the interlayer material, and therefore the intrinsic loss/transmission capabilities of a given board. The most commonly used printed circuit board material is the FR4 glass epoxy combination, which is not recommended for designs impedance controlled designs (Beta LAYOUT Ltd. 2009). Since this application has only one impedance-matched analog circuit, the use of inexpensive FR4 material was decided.

The second PCB characteristic critical to a design is the number of conductor layers. While PCBs can be manufactured with more than 12 conductor layers to accommodate extremely complicated or dense digital routing patterns, many designs only require two,

four, or six layers. In the case of combined analog digital, or RF designs it is often essential to dedicate one or more layers to provide an unbroken reference plane over which critical signals may be routed, to minimize either the EMI they generate, or receive. If extra layers are available, and additional EMI resistance or lower inductance are desirable, critical signals may be routed between two adjacent, unbroken reference layers, effectively producing a shielded conduit. The expected digital complexity of the front-end combined with the need to route, amplify and preserve sensitive L-band microwave signals onboard warranted the use of a four or six layer PCB. As will later be discussed, use of a four layer PCB proved sufficient for revisions A through E, with six layers considered for migration to a future revision F.

A.9. Functional Block Diagram

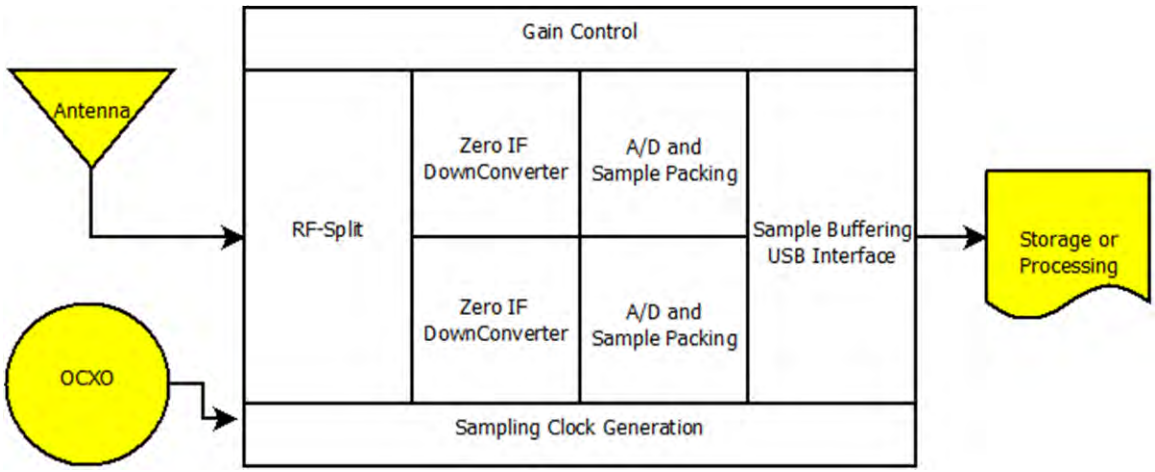

Figure A-6-6 Functional Block Diagram of Front-End

Summarized in Figure A-6-6 is the overall configuration of the front-end revisions B through E, expressed graphically. In the first revision of the system, an onboard oscillator was used in place of the external frequency standard, represented by an OCXO in the block diagram. This change was made in support of the secondary goal of using off-board frequency sources that was facilitated by the change from the MAX2112 to the MAX2120 down converter. As a side note the RF-Split section was implemented in versions A,B,C and E to contain an SMA661AS low noise amplifier in order to maintain a low system noise floor, as well as to compensate for the 16 dB power loss in the RF-Split portion of the front-end.

A.10. Noise Figure Calculations

In order to predict the Noise Figure of the eventual front-end, it is necessary to calculate the cumulative noise contributions of each section of the RF signal chain from the point of reception (antenna) to the point of digitization at the ADC input. The aggregate noise figure is calculated using the Friis formula to determine the effect of cascaded gains and losses within an RF system. Having converted the power gains and losses of each stage of a system from decibels to linear values, ordered with input first produces the Friis formula as

$$nf_n = nf_1 + \sum_{i=2}^{N} \frac{nf_i - 1}{\prod_{i=1}^{i-1} gain_j} \tag{A.1}$$

according to Raquet (2006b).

Unfortunately, the noise figure of the down converter varies with the gain value selected by both the RF gain control voltage GC1, and the baseband gain control register GC2 values, resulting in a non constant system noise figure. The extent of this variation is discussed in an application note from Maxim IC technologies, the graphical representation of which is reproduced in Figure A-6-7

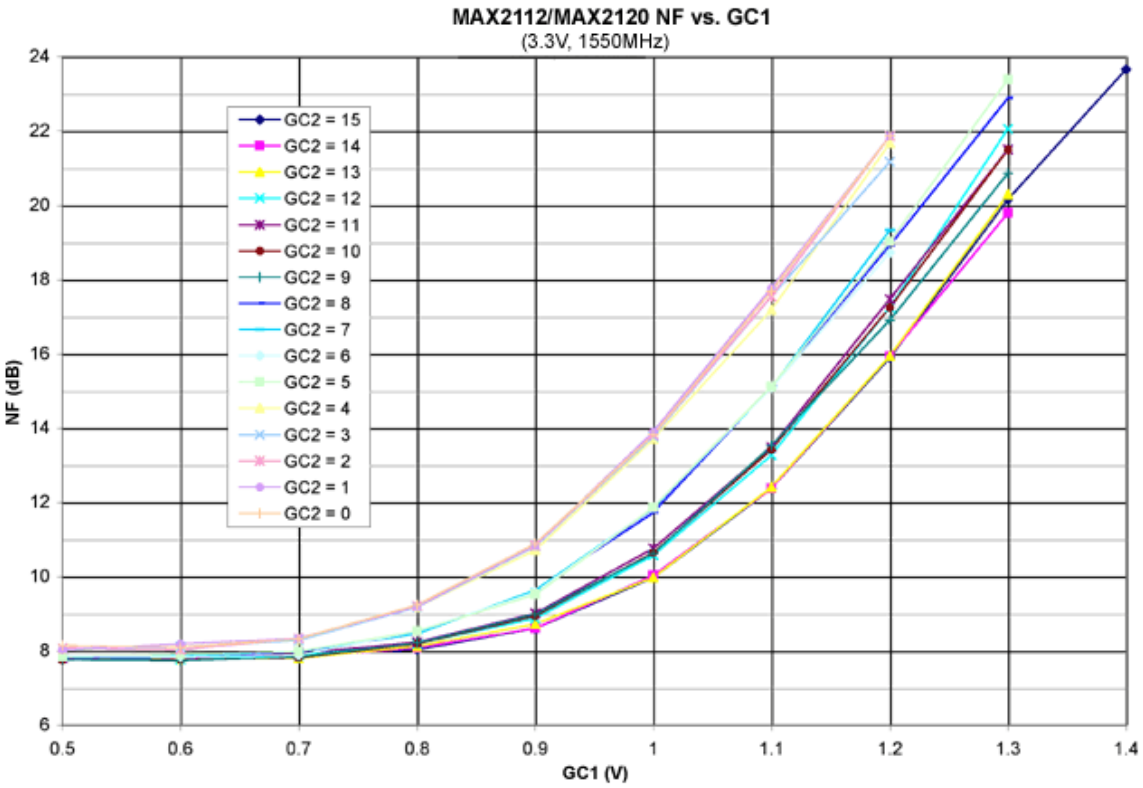

Figure A-6-7 Down Converter Noise Figure Versus Gain settings from (Irons 2008)

To represent the variability in the down converter, it is therefore prudent to specify the noise figure of the combined system at multiple points on the gain plus noise figure operating curve. This curve is reproduced in figure 6-3, while the operating points selected are indicated in Table 6-1, having fixed GC2 at 0 and varying gain only via the GC1 voltage control. It should be noted that the gain values given in figure 6-3 are voltage gain, not power gain and therefore must be scaled by a factor of two to obtain power gain.

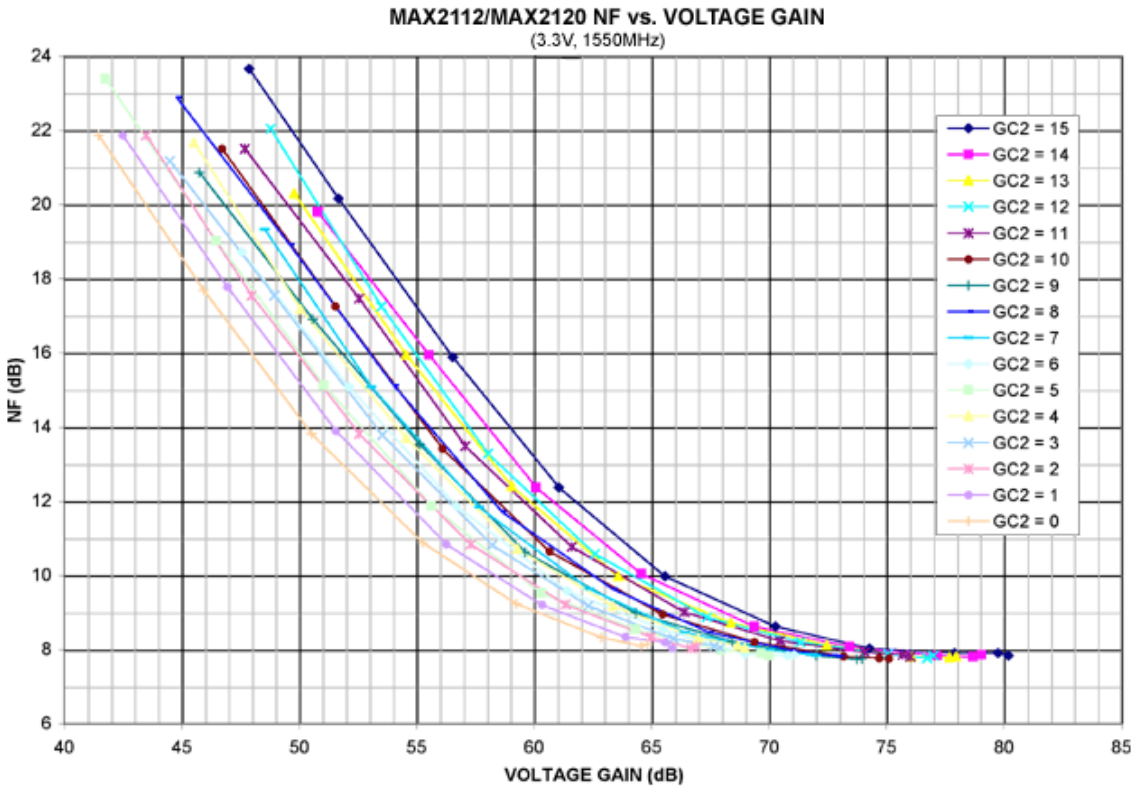

Figure A-6-8: Voltage Gain versus noise figure of down converter from (Irons 2008)

Utilizing the figures stated in Table A-6-1, the calculated noise figure values under the high, medium and low signal gain configurations are 2.00 dB, 2.04 dB, 2.40 dB,

respectively. This indicates that over a 50 dB gain control range, the noise figure of the combined antenna and front-end will vary by only 0.40 dB. Including the gain available by varying the GC2 control register, the range of selectable gains rises to 65 dB over this interval of noise figures. An additional important observation is that the performance of the system is largely determined by the noise figure of the attached active antenna, with the system contributing less than one tenth of total noise power in all cases.

Table A-6-1 RF chain stages, power gains and noise figures

Stage	Power Gain dB (linear)	Noise Figure dB (linear)
1: NovAtel 702GG Antenna	29 dB (794.32x)	2 dB (1.58x)
2: SMA661AS LNA	18 dB (63.10x)	1.15 dB (1.30x)
3: Passive Splitter and Impedance matching	-16 dB (0.0251x)	16 dB (39.81x)
4A: MAX2120 High Gain	130 dB (10^13x)	8 dB (6.31x)
4B: MAX2120 Med. Gain	100 dB (10^10x)	14 dB (25.12x)
4C: MAX2120 Low. Gain	80 dB (10^8x)	23 dB (199.53x)

A.11. Implementation Revisions

Revision A:

Board Image:

Board layout image not available.

Notes:

-Utilized MAX2112 Fractional-N PLL based down converter

-Contained 12 MHz onboard TCXO

Subsystems Verified:

-USB interface verified to function as expected

-Clock recovery and sampling clock PLL circuits verified to function as expected

Failure Mode:

-Exposed power trace prevented installation of 2nd Front-End Channel due to shorting

-Determined MAX2112 was undesirable relative to related MAX2120 down converter

Revision B:

Board Image:

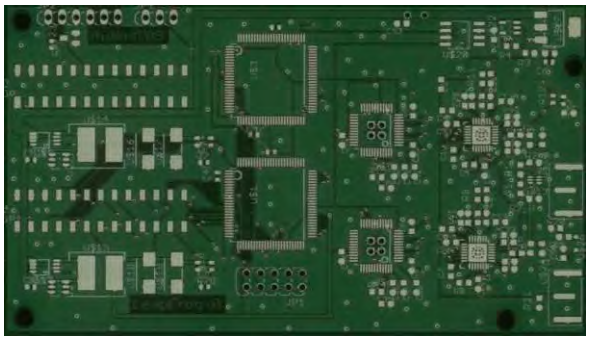

Figure A-6-9 Image of Printed Circuit Board Revision B

Notes:

-Utilized MAX2120 Integer-N PLL down converter

-Frequency reference provided from external OCXO

Subsystems Verified:

-External clock termination and drive level adaptation

-MAX2120 Band selection

-PLL circuit clocking selection

Failure Mode:

-USB buffering in FT2232H IC found to be 8x smaller than documented resulting in severe data loss issues that were previously unexpected

Revision C:

Board Image: (lower layer shown, including dual ram chip footprints)

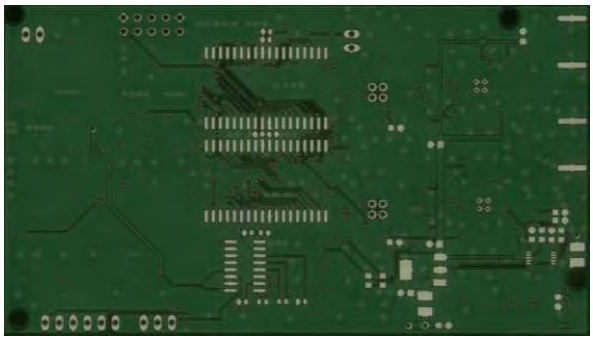

Figure A-6-10 Revision C PCB bottom layer showing RAM footprints

Notes:

-Altered RF Layout in attempt to reduce PCB loss

-Added 1 MB SRAM in ping pong buffer configuration

-Upgraded CPLD from 240 Logic Elements to 570 Logic Elements to contain ram controller

-Increased CPLD pin count to implement memory controller for ping pong buffer

-Added digital potentiometer circuit for gain control via VGC1

Subsystems Verified:

-Gain Control via VGC1

-CPLD control of RAM ICs

Failure Mode:

-Re-routed RF signals produced oscillatory feedback destroying signal of interest

Revision D:

Board Image:

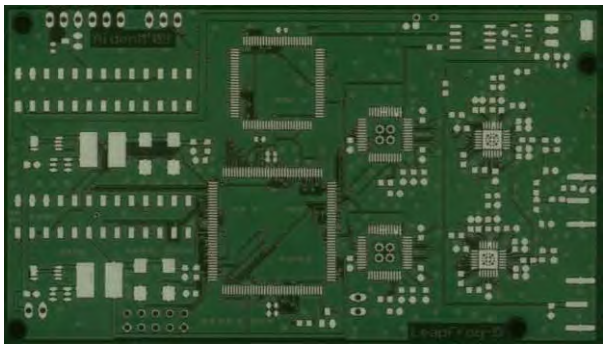

Figure A-6-11 Revision D Printed Circuit Board top layer

Notes:

-Removed input LNA(s) to ensure lack of oscillation

-Added DC-Bias injection to antenna connector to allow active antenna use

Subsystems Verified:

-PC side multi-threaded logging software

-First version of system capable of supporting acquisition of logged GNSS signals

Failure Mode:

-Lack of RF gain prior to high loss/noise figure splitting and impedance matching stage

-EM interference pickup believed to be self generated by board digital segments

-Digital data loss and corruption later determined to be a further issue affecting performance

Revision E:

Board Image:

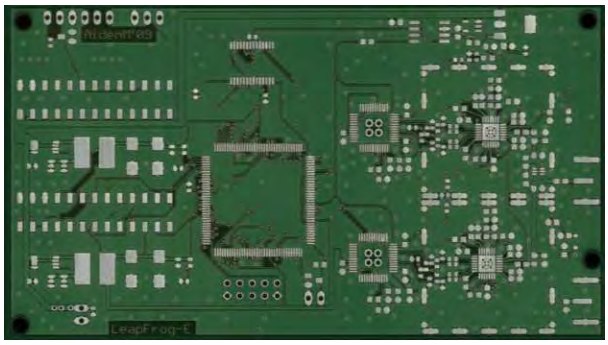

Figure A-6-12: Revision E Printed Circuit Board

Notes:

-Changed to physically smaller CPU package to conserve board space

-Added RF shielding to RF down converters and support components

-First version of board to contain both DC-Bias injection and SMA661AS LNA

-Re-implemented FIFO controller to remove timing race conditions causing data loss

Subsystems Verified:

-Updated FIFO controller re-verified. Cause of previous false pass during revision C determined to be variation between memory chips allowing some to operate far beyond specified timings.

Failure Mode:

-Intermittent data loss (as infrequently as once per 300 seconds) believed to be due to insufficient RAM capacity combined with poor USB performance on some computers

-10 MHz tone interference from Local Oscillator signal corrupting output spectrum in 40 MHz operating mode. Insufficient CPLD fabric to implement filtering

A.12. Revision E Performance

In this section the performance of the Revision E hardware will be evaluated with respect to the characteristics of acquirable signal spectra, and other design criteria. Despite the statement of two 'failure modes' for the Revision E hardware, this version of the front-end is the first capable of providing data segments of several minutes in length, without data loss or corruption. For this reason the failure modes listed for revision E should be viewed as targets for future improvement of the front-end.

Total Bandwidth:

Testing has shown that the performance of the Revision E front-end is sufficient for the capture of two bands of 1-bit quantized data at up to 40 MHz per band of bandwidth via 40 MHz quadrature sampling.

Tuning Range:

The functional tuning capacity of each front-end spans the range between 925 MHz and 2.175 GHz, with the included LNA operating well into the 1.95 GHz CDMA cellular band, as is shown in figure 6-10.

Self Interference:

Figures 6-8, 6-9, 6-11, and 6-12 demonstrate that the generated self interference within the front-end is limited to spurs spaced at roughly FS/8 each with power equivalent to that found in 200 Hz of spectrum when using a 15 MHz Real sampling scheme. Unfortunately the amplitude of the Local Oscillator feedthrough spur for signals spanning the 10 MHz frequency point are approximately 40 times stronger than these spurs and will require digital signal processing to be nullified.

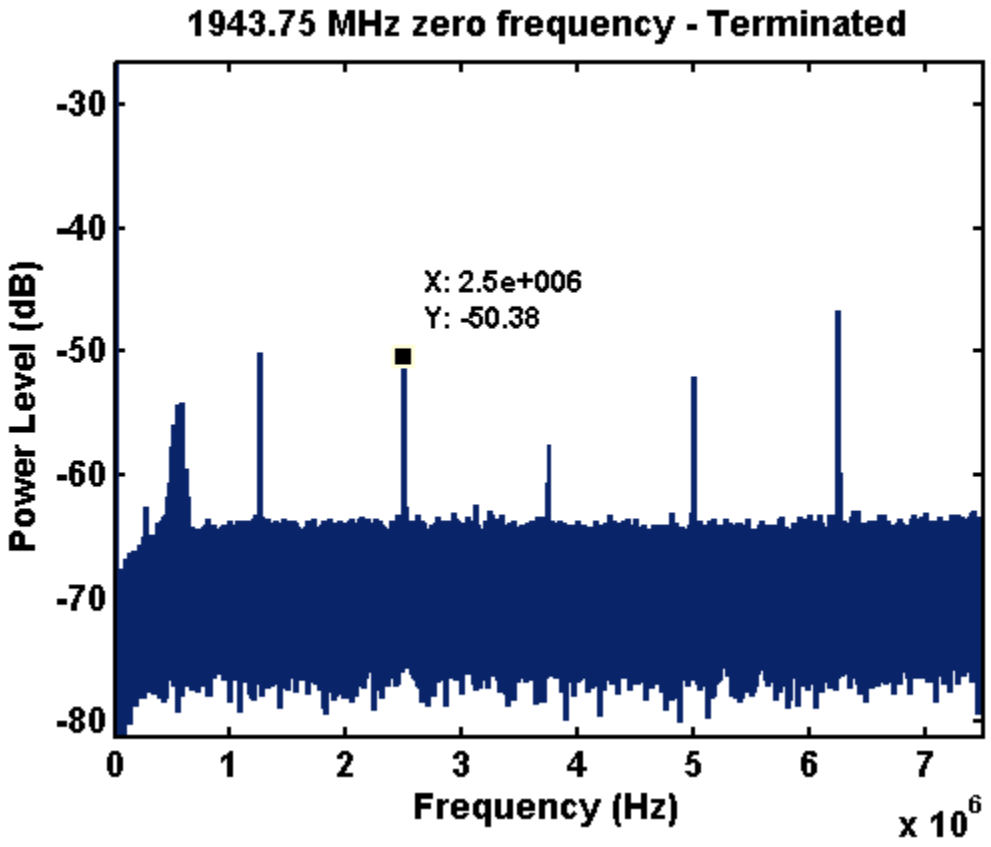

Figure A-6-13: Noise present with terminated antenna connector (no antenna) consists of internally generated interference, as well as strong ambient interference signals. The lobe present near 0.5 MHz is a CDMA cellular signal received by the PCB.

Stability: The stability of the front-end combined with the currently used test machine is such that approximately one in three tests will last for five minutes or more of continuous collection without an overflow in the onboard buffer of the front-end. It is expected that doubling this buffer should be sufficient to allow indefinite collection lengths without data loss.

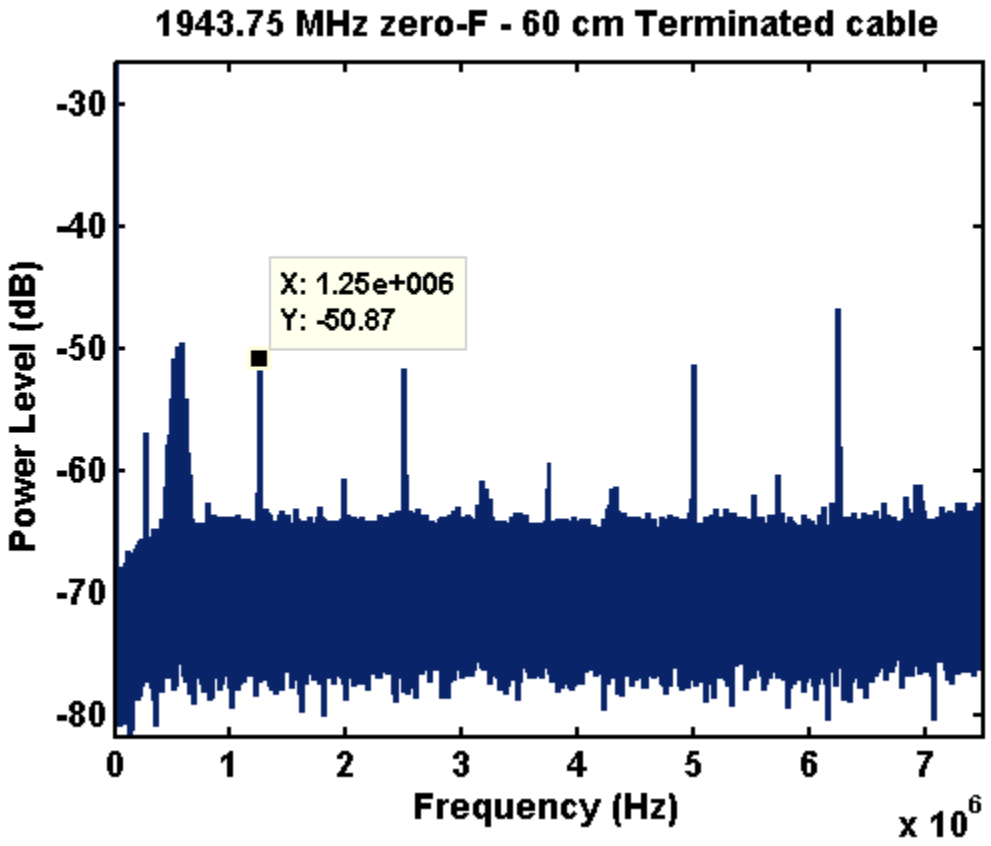

Figure A-6-14: Noise present with terminated 60 cm cable (no antenna) consists of internally generated interference, as well as strong ambient interference signals. The lobe present near 0.5 MHz is a CDMA cellular signal received by the 60 cm length of cable as well as the PCB.

Primary Goals Summary: Of the primary goals established at the commencement of the project, all have been satisfied by the Revision E front-end implementation, with the exception of the aggregate bandwidth goal of 80 MHz of spectrum. This failure is due to

the presence of extremely strong local oscillator feed-through effects in the down-converter IC. It is possible that this may be solved through the implementation of notch filtering within the FPGA of Revision F. Since the revision E CPLD is of extremely limited size, there is not enough fabric left to implement these features within revision E. Additionally, to allow expansion of the onboard RAM buffers, a transition to an FPGA with more available IO will be required.

Secondary Goals Summary: Of the secondary goals selected at the outset of the project, all have been achieved.

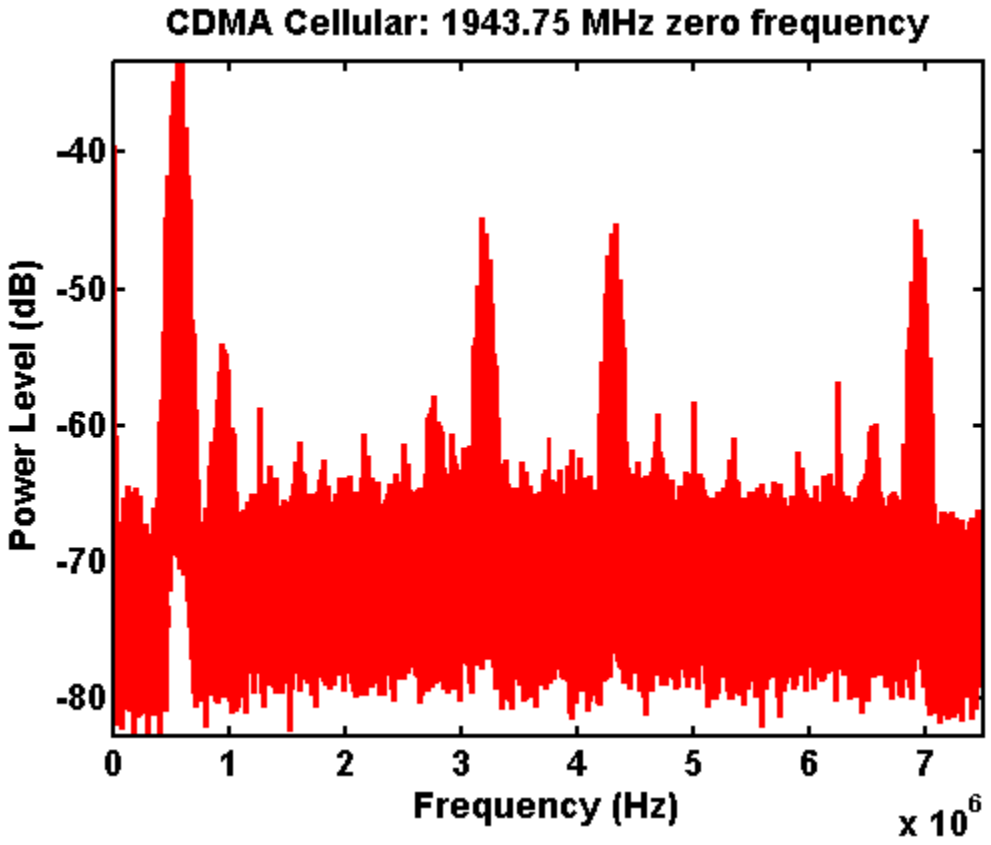

Figure A-6-15: Strong signal present with antenna connected, front-end tuned to CDMA cellular band. Signal consists of relatively negligible internally generated interference, as well as strong ambient cellular signals. The extreme strength of the lobe near 0.5 MHz indicates why it was visible in the previous figures.

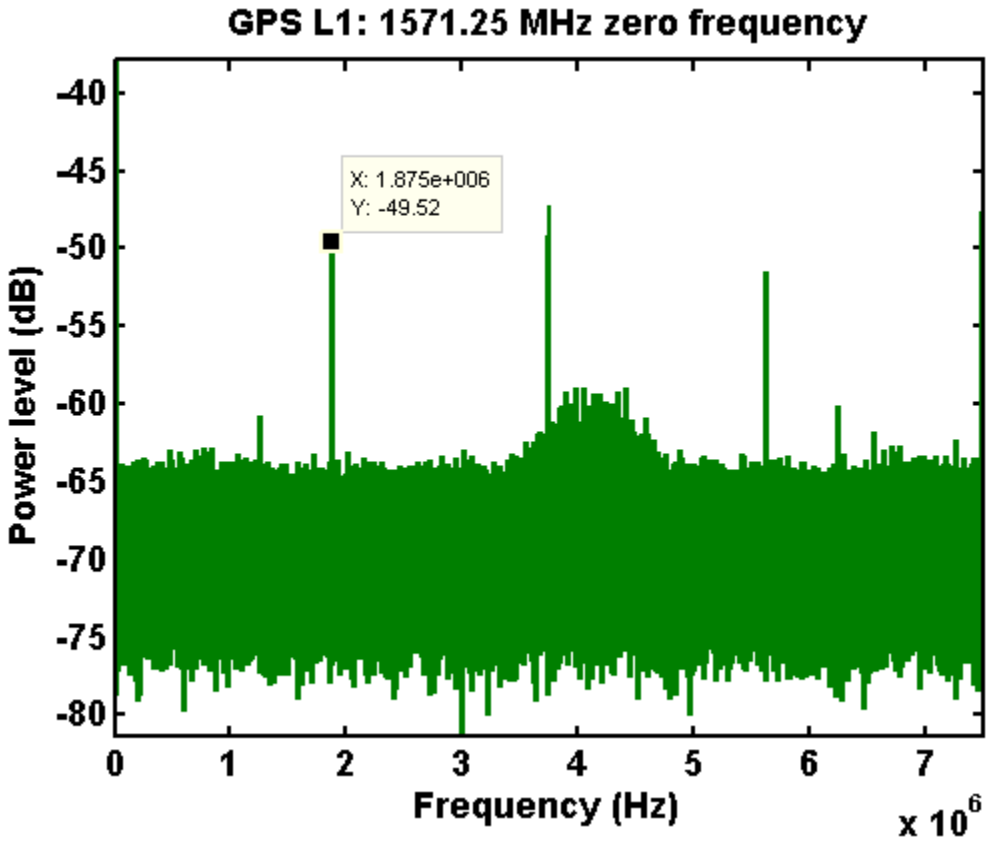

Figure A-6-16: Spectrum of collected GPS L1CA data and internally generated interference spurs. Since each point in the spectrum represents only 5 Hz of bandwidth, the power contained within the spurs is seen to be low. Despite the 15 dB level above the noise floor of these spurs, their power represents less than that contained within 200 Hz of 'uncorrupted' spectrum. This explains why the signals tracked from this data remain strong despite the presence of these spurs.

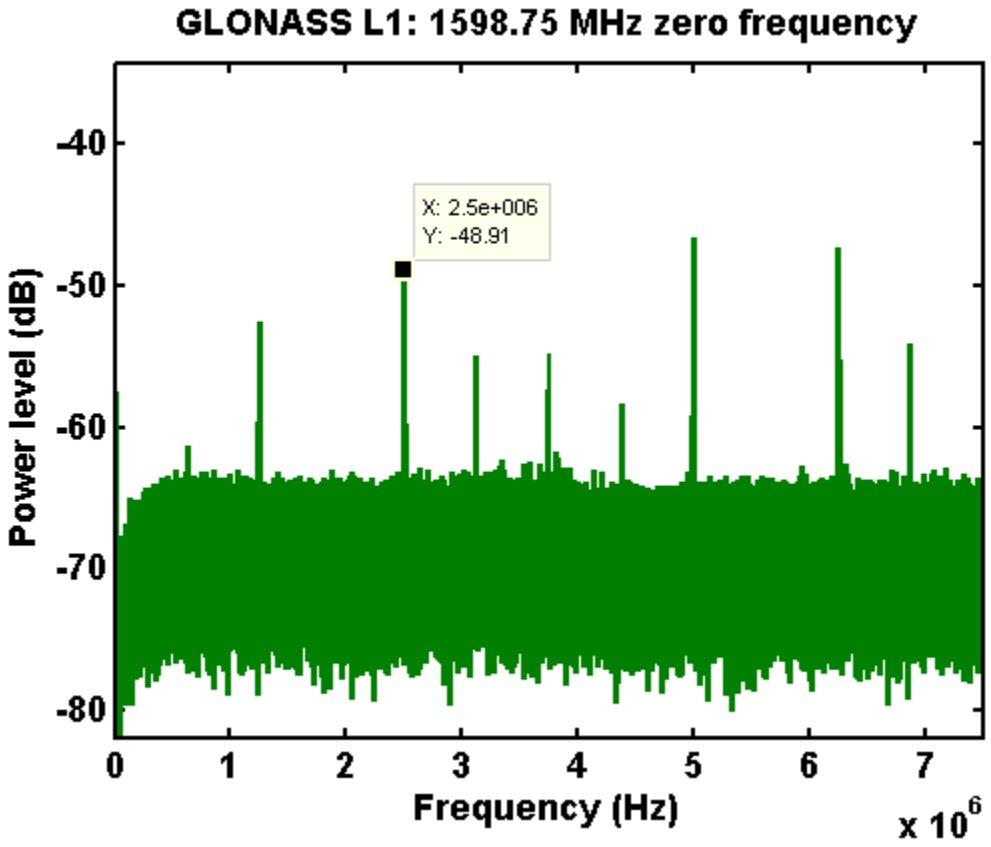

Figure A-6-17: Spectrum of collected GLONASS L1 data and internally generated interference spurs. Exactly as with the prior GPS spectral content image, since each point in the spectrum represents only 5 Hz of bandwidth, the power contained within the spurs is seen to be low. Despite the 15 dB level above the noise floor of these spurs, their power represents less than that contained within 200 Hz of 'uncorrupted' spectrum. This explains why the signals tracked from this data remain strong despite the presence of these spurs.